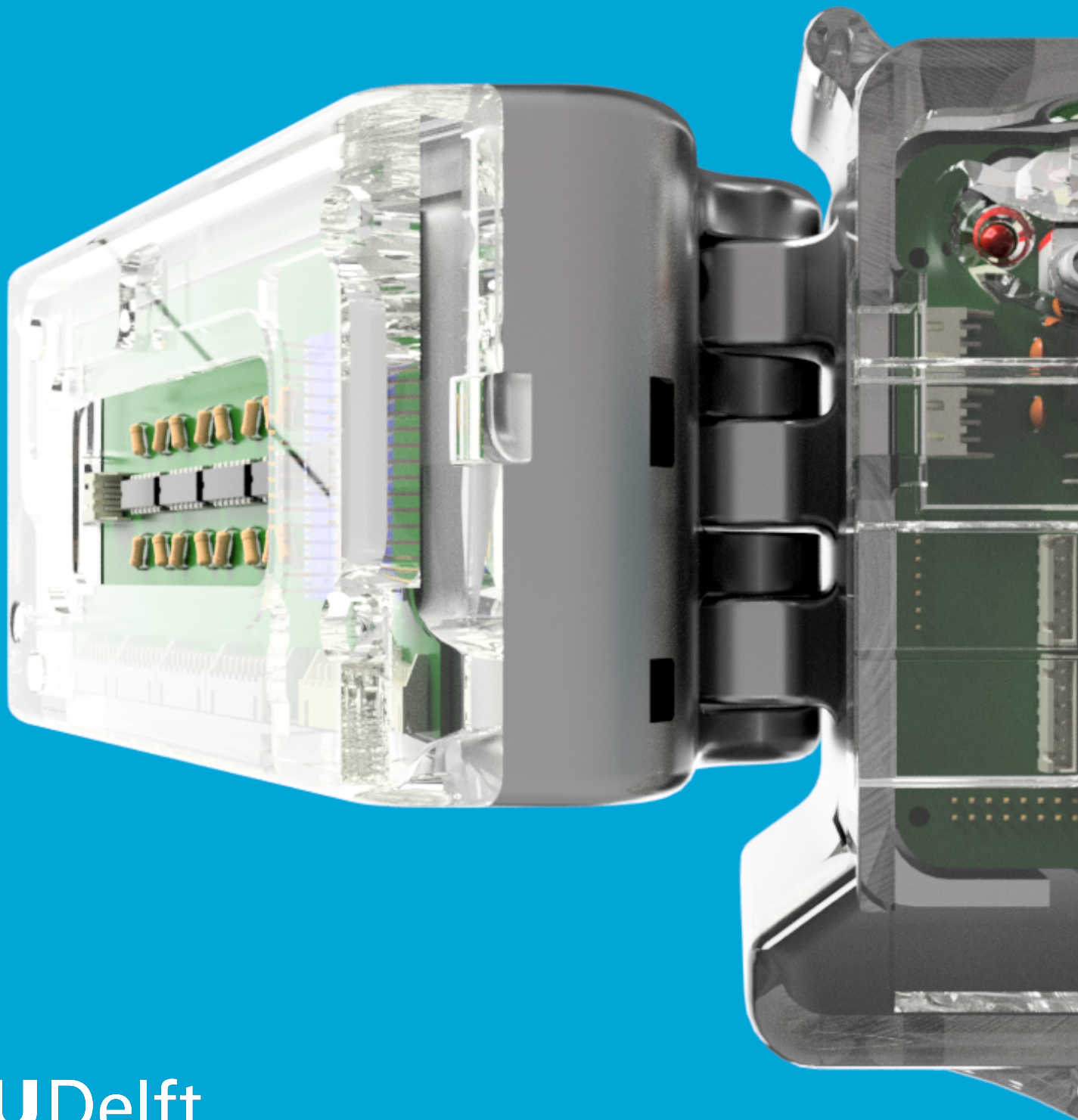


Simon van Borren

Prototype Design and Workflow for a Scoliosis Brace Monitoring and Evaluation System



PROTOTYPE DESIGN AND WORKFLOW FOR A SCOLIOSIS BRACE
MONITORING AND EVALUATION SYSTEM

A thesis submitted to the Delft University of Technology in partial fulfillment
of the requirements for the degree of

Master of Science in Mechanical Engineering

by

Simon van Borren

Jul 2022

Simon van Borren: *Prototype Design and Workflow for a Scoliosis Brace Monitoring and Evaluation System* (2022)

The work in this thesis was made in the:



Department of BioMechanical Engineering
Faculty Mechanical, Maritime and Materials Engineering
(3mE)
Delft University of Technology

Supervisors: Prof.dr. Jaap Harlaar
Dr. Joost Rutges

Co-reader: Dr. ir. Paul Breedvled

ABSTRACT

While bracing has been proven to be an effective treatment strategy for adolescent idiopathic scoliosis, its effectiveness is often found to be inconsistent in practice. One of the main reasons for this is that the forces applied by the brace may be subject to constant change, while its required effect is expected to change over time as well. Brace treatment becomes even more complicated when considering that both the patient and the practitioner are provided with limited to no information on how this relation may be changing over time. While measurements of the pressure distribution may be used for evaluation of the brace, most commercially available devices are too expensive or unsuitable to be integrated in a brace. This study therefore sought to investigate the possibility of designing a cost effective monitoring system based on force sensitive resistors (FSR) that can be implemented in the brace to evaluate brace performance.

Several metrics were defined to evaluate different functional aspects of the brace. This simultaneously served as a basis for the system requirements, which focused on finding a cost effective solution for evaluating brace performance, while no restrictions on dimensions and mass of the prototype were set at this time. The hardware of the system was based on an Arduino Mega microcontroller connected to custom designed PCBs for voltage regulation and signal conditioning, which were integrated in a purposely designed belt. The belt was connected to a sensor pad with a total of 15 integrated FSRs (*FSR402 by Interlink Electronics*) and was designed to fit the pad located in the lumbar area of the brace. The FSRs in the sensor pad were calibrated in the 0 - 26kPa range using a model developed for creep and hysteresis compensation. When tested with a consistent actuation system, a random error of 4% was found. The model also showed to yield a decent approximation of the hysteresis behavior of the FSRs using a parametric third order polynomial function, but further research is required for this to be validated.

In order to evaluate the three dimensional effect of the brace forces on the spinal column, the spatial geometry of the spine and the sensorpad had to be reconstructed. A generative design algorithm was developed for doing this using only a surface model of the torso, an AP radiograph of the spine, standard vertebra dimensions and the geometry of the sensor pad including the relative two dimensional locations of the integrated FSRs. The method yields a low resolution reconstruction of the required geometry and serves as a proof of concept for acquiring data that normally would require sophisticated equipment which may not always be available.

Validation showed that the system could effectively be used to measure pressure distribution inside a scoliosis brace. Differences were measured related to posture and respiratory movement, which was found to have an effect on the mean pressure and the pressure distribution in the lumbar area. Combining the measurements with the spatial geometry allowed for computation of equivalent bending moments, which seemed to be in line with the expected function of the brace.

Although this research showed promising results for an FSR based pressure measurement system for scoliosis braces, further research is required to optimize the different aspects of its design.

CONTENTS

1	INTRODUCTION	1
1.1	Background	1
1.2	General Working Principles of a Scoliosis Brace	2
1.3	The Complexity of Brace Treatment	3
1.4	Pressure Monitoring for Scoliosis Braces	5
1.4.1	Using Pressure Monitoring for Optimizing Brace Treatment	5
1.4.2	State of the Art: Pressure Monitoring Systems	5
1.5	Problem Statement and Research Goal	7
1.6	Thesis Structure	7
2	METHODS FOR FUNCTIONAL BRACE EVALUATION	9
2.1	Introduction	9
2.2	One Dimensional Evaluation Metrics	9
2.3	Three Dimensional Evaluation Metrics	10
2.4	Four Dimensional Evaluation Metrics	11
3	SYSTEM REQUIREMENTS	15
4	PROTOTYPE DESIGN	17
4.1	Introduction	17
4.2	Electronic Hardware Design	17
4.2.1	Design Process	17
4.2.2	Main Components	18
4.2.3	System Architecture	20
4.2.4	PCB Design	23
4.2.5	Integration and Connection	25
4.3	Sensor Pad Design	27
4.3.1	Design Process	27
4.3.2	Sensor Integration Design	27
4.3.3	Sensor Placement and Pad Shape	32
5	SPATIAL RECONSTRUCTION METHODS	35
5.1	Introduction	35
5.2	Sensor Pad Mapping	36
5.3	Spinal Reconstruction	37
5.3.1	Introduction	37
5.3.2	Vertebra and IVD Data	37
5.3.3	Scan Placement and Landmark Identification	38
5.3.4	Reconstruction Algorithm	38
5.3.5	Vertebral body and IVD Centroid Computation	41
5.3.6	Local Vertebra Frame and Rotation Matrix	42
6	STATIC CALIBRATION OF FORCE SENSITIVE RESISTORS	43
6.1	Introduction	43
6.2	Methods	43
6.2.1	Test Setup	43
6.2.2	Test Procedure	43
6.2.3	Hysteresis Compensation Method	46
6.2.4	Measurement Uncertainty	46
6.3	Results	48
6.3.1	Hysteresis Compensation Model	48
6.3.2	Measurement Uncertainty	51
6.4	Discussion	51

7	EVALUATION OF BRACE FUNCTION FOR A CHENEAU TYPE SCOLIOSIS BRACE	55
7.1	Introduction	55
7.2	Methods	55
7.2.1	Patient Details and Research Objective	55
7.2.2	Test Procedure	55
7.2.3	Evaluation Metrics	57
7.3	Results	63
7.3.1	One Dimensional Evaluation	63
7.3.2	Three Dimensional Evaluation	65
7.3.3	Four Dimensional Evaluation	67
7.4	Discussion	69
8	DISCUSSION	71
9	CONCLUSION	73
A	ACTUATION SYSTEMS	81
B	PCB ROUTING DESIGN AND CIRCUIT SCHEMATICS	83
C	GRASSHOPPER SCRPT	85
D	CALIBRATION PROTOCOL	87
E	ARDUINO & MATLAB CODE FOR DATA ACQUISITION	89
F	AVERAGE BREATHING CYCLE PRESSURE DISTRIBUTIONS	95

ACRONYMS

- **AIS** - adolescent idiopathic scoliosis
- **FSR** - force sensing/sensitive resistor
- **IVD** - intervertebral disc
- **GC** - geometric center or centroid
- **COP** - center of pressure
- **COR** - center of rotation
- **PCB** - printed circuit board
- **BREP** - Boundary Representation

1 | INTRODUCTION

1.1 BACKGROUND

Adolescent Idiopathic Scoliosis (AIS) is a condition causing progressive deformation of the spine, typically resulting in an abnormal curvature and torsion of the spinal column [32]. Its progressive nature is thought to be caused by mechanisms described by the Heuter-Volkman Principle, which states that skeletal growth is retarded by mechanical compression and accelerated by tension [16]. In an upright position, gravitational loads cause mechanical compression of the spinal column. For a normal spine, the surrounding musculature and the shape of the vertebrae cause the compressive load to follow the spinal profile. This results in symmetric compression of the vertebrae and the growth plates with respect to the sagittal plane, causing the growth of the spinal column to also be symmetric. In the case of AIS, the spine is imbalanced, which leads to asymmetrical compression and thus asymmetrical growth of the vertebrae with typically a lateral curvature and torsion of the spinal column as a result [32, 75]. The more the scoliotic curve progresses, the more significant this imbalance becomes as the (lateral) spinal bending moment over the vertebrae as a result of gravitational forces also increases, subsequently increasing the asymmetrical compression even further [14]. This effect was simulated in a study by Crijns et al. (2017) as depicted in Figure 1.1 [17]. The study illustrated the effect of restrained differential growth of the spinal column and how this affects the progression of the scoliotic curve.

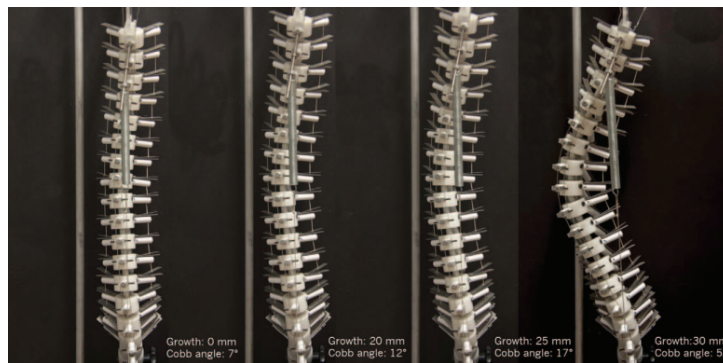


Figure 1.1: An experiment by Crijns et al. (2020) illustrates the effect of differential growth on the spinal curvature [17]. Growth was simulated by increasing the distance between the vertebral bodies. A spring was used to asymmetrically restrain the spine. A rapid progression was found after a Cobb angle of 30 degrees is reached.

The severity of scoliosis is primarily assessed by the Cobb angle, which is a measure for the greatest angle at a particular region of the spinal column [16]. The Cobb angle usually refers to the greatest lateral angle of the spinal column in the coronal plane as it is typically measured from a standing AP¹ radiograph [36] (see Figure 1.2). This lateral curvature is usually also accompanied by axial and sagittal abnormalities, which makes scoliosis a three dimensional deformity [36]. A Cobb angle of more than 10 degrees is required before the spinal curvature is actually referred to as scoliosis [16]. Mild Scoliosis, which is characterized by a Cobb angle of 10 - 25 degrees usually does not cause any serious symptoms, but may cause back pain in some rare cases [77]. However, in moderate cases with a Cobb angle of 25 - 40 degrees, the symptoms can get progressively worse [77]. In addition to this, scoliosis

¹ Anterior(=front) to Posterior(=back)

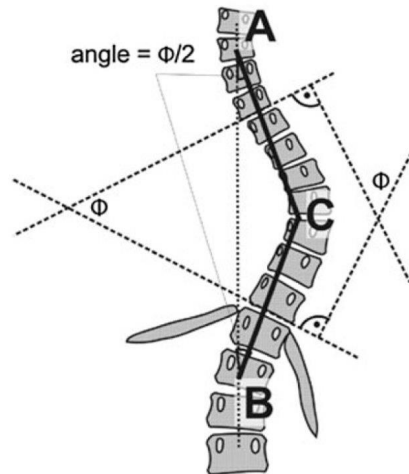


Figure 1.2: Illustration showing the coronal Cobb Angle ϕ which is the angle between a line normal to segments AC and BC. Figure was obtained from Hefti et al. (2013) [32].

may also affect the patient's appearance, by causing uneven hips and shoulders, prominent ribs and a shift of the waist and trunk [54, 85]. Severe scoliosis is characterized by a Cobb angle of more than 40 degrees [77] and may cause serious cardiopulmonary complications [1, 35]. A Cobb angle of more than 45 degrees is typically when surgical intervention is required.

With growth being the driving factor behind curve progression, treatment is preferably started before the patient's growth spurt and involves active management of the scoliotic curve until skeletal maturity is reached [66, 88]. In mild cases, AIS is usually treated by physical therapy [24, 85]. A brace treatment is usually recommended for patients with Cobb angles between 30 and 45 degrees when growth is remaining and for patients with Cobb angles between 20 and 30 degrees when a progression of more than 5 degrees is observed in less than 6 months [85]. The scoliosis brace is an orthotic device that continuously imposes an in-brace correction of the spine by applying external forces to the torso.[29] This continuous correction of the spine forces a symmetric growth pattern and prevents the scoliosis curve from progressing any further [29, 32] The brace should actively manage the curve progression throughout the growth spurt and should therefore be worn 18 - 23 hours per day over a period of 2 - 4 years or until skeletal maturity is reached [29]. Weinstein et al. (2013) [88] showed in a multicenter study that the use of scoliosis braces was effective in preventing the need for surgery in approximately 72% of the cases where a rigid brace was prescribed. This was in contrast to a 48% success rate for the cases where no braces were used. While bracing can therefore be considered to be an effective method of treatment, it should be noted that its outcome depends on a lot of external factors as will be discussed in more detail in Section 1.3, making it a complex treatment strategy that requires full commitment of the patient and all other parties involved.

1.2 GENERAL WORKING PRINCIPLES OF A SCOLIOSIS BRACE

While there currently exist many different brace designs [93], they all rely on the same core principle, which is to achieve continuous correction of the spinal column over a prolonged period of time in order to prevent or slow down the progression of the scoliotic curve [29, 65]. The most effective structure of a scoliosis brace is currently still that of a hard plastic shell covering the majority of the torso (see Figure 1.3). The brace has a highly personalized shell shape which is designed to translate a tensioning of the straps to external forces to the torso. The highly personalized design is required for three dimensional correction of the lateral bending and torsion of the spine, specifically tailored to the patient's curve type and morphology [21, 65]. While being different in their specifics, all brace



Figure 1.3: An example of two widely used rigid brace designs (a) The Boston Brace [21] and (b) the Rigo-Cheneau Brace.[65]

types generally achieve the required correction using a three point force system. This means that the brace applies forces on both ends of the concave part and at the apex of the convex part of the curve [29]. The three point system should simultaneously correct the lateral curve and de-rotate the spine. In some cases a single three point system is enough to correct the spine, which means that the brace only requires three pads that apply pressure to the torso. However, in most cases a fourth pad is necessary in the trochanter region. A second three point system is then necessary in order to correct a double scoliosis curve or to function as a counter rotation pad to keep the patient vertical. The highest pressure is usually applied in the lumbar and thoracic region [52, 63, 86, 90]. The axillary pad, which is the pad that is located most proximally, is necessary to achieve static equilibrium. This pad has the longest lever arm with respect to the pelvis and therefore also requires the least amount of pressure.

Correction of the spine does however not only rely on these passive brace forces alone, but is often also contributed to by active self correction, which is the additional correction that is achieved as the patient actively moves away from the high pressure area in the brace [29, 42] (see Figure 1.4). Most sophisticated brace designs, like the Cheneau type brace (see Figure 1.3b), leave room for expansion opposite to the pressure pads [65, 66]. These braces are designed in such a way that chest expansion as a result of respiratory movement causes the torso to be pushed towards the expansion area. In addition to that, the patient is often also taught specific breathing exercises that emphasizes breathing into these expansion areas. These movements are supposed to guide the patient away from the pressure pads, which should give an additional corrective effect by providing them with somatosensory input, thus making them more aware of their posture [29]. While physical therapy has been found to have a positive effect when used in combination with the brace treatment [24], the relation between respiratory movement and active self correction is still largely unknown. Nevertheless, the corrective effect caused by the brace may always be the result of the passive brace forces on the one hand as well as the active self-correction on the other hand.

1.3 THE COMPLEXITY OF BRACE TREATMENT

While its core principle has been found to be an effective strategy for preventing curve progression [88], bracing currently still seems to yield inconsistent results in terms of treatment outcome. This can partially be attributed to the fact that not all patients respond as well to bracing. The immediate in-brace correction, which is the correction the brace can immediately achieve upon donning², has been found to be suitable as a predictive metric for a successful treatment outcome [15]. Depending on the patient's spinal stiffness, it may be more difficult in some cases than others to achieve sufficient in-brace correction [13]. Other morphological factors that have been found to affect in-brace correction

² Putting on, opposite to *doffing*; taking off

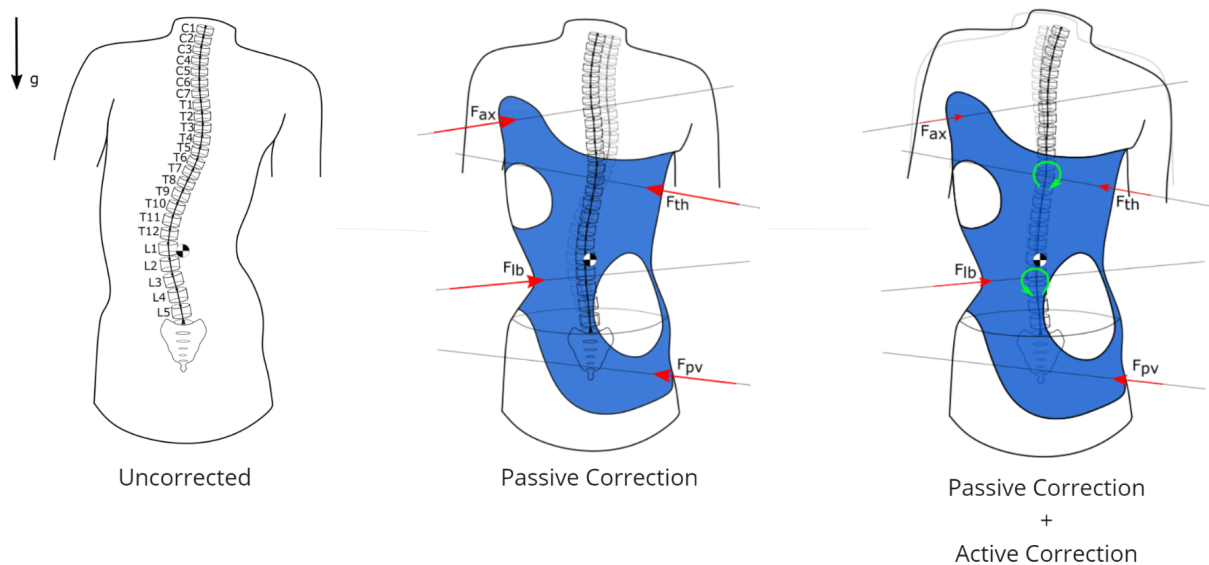


Figure 1.4: Figure illustrating the (immediate) corrective effect of the brace with **passive correction** resulting in equivalent forces at the axillary pad (F_{ax}), thoracic pad (F_{th}), lumbar pad (F_{lb}) and the pelvic pad (F_{pv}). The figure on the outer right illustrates the additional corrective effect of **active self-correction** which can be interpreted as bending moments induced by active muscle contributions. The brace can be seen to act laterally but also vertically, to counteract the effect of gravity (g).

are the curve type [84] and the patient's body mass index (BMI) [46, 61], where individuals with a thoracic curve or a higher BMI are generally at higher risk of curve progression.

Although morphological factors seem to have a significant effect on the effectiveness of a brace treatment, they cannot be considered as the only explanation for treatment failure. Bracing is a very intensive form of treatment, where the patient is often required to wear the brace for up to 23 hours a day and therefore requires cooperation of all parties involved. Patient compliance is therefore a key factor in the overall treatment outcome [12, 40, 44, 64, 88]. This implies that the brace is to be worn for the prescribed amount of time and tensioned at the levels required to achieve sufficient correction, which is referred to as the quantity and quality of compliance respectively [50]. However, even in the case of perfect compliance, there are many factors that may still affect the intended function of the brace. Strap tension and the related pad pressure have been found to be affected significantly by the patient's posture [2, 8, 63, 86]. When a posture having a significantly compromising effect on the corrective function of the brace is assumed routinely, the effectiveness of the brace treatment may suffer as a result.

Other factors that can be considered to compromise the effectiveness of the brace treatment are potential changes in morphology throughout the treatment. Inevitable changes include the growth of the spinal column, which should be accounted for by appropriate modifications of the brace. Failing to do so may lead to a decreased effectiveness or in some cases may even aid curve progression [91]. While the expected growth of the patient therefore always has to be taken into account when fitting the brace, assessment of brace function is only done during fixed follow-up appointments or relies on self-report of the patient. Unexpected morphological changes like rapid spinal growth or potential changes in BMI that ideally would require intervention are therefore not always adequately identified.

It can therefore be concluded that bracing is inevitably complicated as a treatment strategy as its effectiveness may be affected by many factors that are out of control of both the patient and the practitioner. Many studies have sought to improve the treatment by focusing on the design of the brace. While this certainly has led to some improvement, it should be noted that the success of a brace treatment isn't solely determined by the initial design of the brace. The rigid brace shell may always require adequate



Figure 1.5: An example of two pressure measurement systems. (a) Tekscan's I-Scan System, including a sensor array, a data acquisition module and software [79]. and (b) the Pedar Smart Insole by Novel GmbH, including the insole and the data acquisition module. [60]

modifications to account for the constantly changing morphology of the patient. Close monitoring is therefore key for ensuring that the brace achieves continuous correction of the spine. Currently however, both the patient and the practitioner is provided with limited to no insight on how the function of the brace is affected throughout the treatment period. It is therefore hypothesized that optimization of the brace treatment should start at improving the means of monitoring in order to provide feedback and ensure adequate intervention.

1.4 PRESSURE MONITORING FOR SCOLIOSIS BRACES

1.4.1 Using Pressure Monitoring for Optimizing Brace Treatment

The most effective way of evaluating the function of the brace may be by monitoring the pressure at the brace-torso interface. While this may not directly be related to curve correction (as this is also assumed to be contributed to by active self correction, see Figure 1.4), it may provide useful information that may indicate potential changes in brace function. The brace treatment may therefore benefit greatly from a method for continuous pressure monitoring at the brace-torso interface. However, monitoring the mean pressure magnitude at the pressure pad areas alone may be insufficient to provide any meaningful insights on how exactly the function of the brace is affected. This can be explained by the fact that the brace is designed to apply pressure to specific areas on the torso, which can be translated to an equivalent force with a magnitude, direction and point of application in that specific area. A change in any of these parameters should be interpreted as a change in the function of the brace. Monitoring the pressure distribution over a prolonged time period may therefore provide the necessary information to analyze how the function of the brace is affected over time and identify certain patterns that may indicate how and when the brace should be modified to optimize the treatment. This may not only provide the practitioner with useful tools to assess when the treatment needs intervention, but it may also be used to give the patient feedback on the quality of brace wear, which has been shown to improve both quantity and quality of compliance [48].

1.4.2 State of the Art: Pressure Monitoring Systems

Pressure distribution in orthoses is most commonly measured using piezoresistive or capacitive pressure sensors [41]. Capacitive sensors are typically more stable than piezoresistive sensors [41, 70], but are generally more expensive [4, 5, 74] and require more complex signal conditioning circuits and

calibration algorithms [11]. For both type of sensors, an applied load results in a change in voltage over the sensing element, either caused by a change in resistance or capacitance [23, 47]. Depending on the sensing area, one can express the load as either a pressure or a force. A calibration procedure is necessary to relate the measured voltage back to a force or pressure magnitude.

Implementing a multitude of those sensors in an array of interconnected sensing elements allows one to measure a pressure distribution. Rather than measuring the pressure at all sensing elements simultaneously, multiplexing is used to sequentially measure the voltage over each sensing element individually [31]. The pressure distribution over the array is then sampled at a rate of $f_{system} = n_{sensors} f_{sensor}$, with $n_{sensors}$ being the amount of sensing elements in the array and f_{sensor} the sampling rate of each element individually. Increasing the amount of sensing elements in a specific area increases the spatial resolution and robustness of the pressure distribution measurements. However, it also increases the complexity of the system. Many pressure sensor arrays therefore require an expensive data processing module and specific software designed by the manufacturer in order to process the voltage signal to a consistent value that can be used for calibration.

Measurement Systems

Currently, there are no commercially available pressure measurement systems that are specifically designed for scoliosis braces. Therefore, a variety of different systems have been used in past studies to measure brace pressure. These systems were primarily designed and manufactured by either Tekscan, Inc. or Novel GmbH [60, 79] (see Figure 1.5). While the Tekscan systems primarily use piezoresistive technology, the Novel systems implement mostly capacitive sensor technology. Although these systems proved to be useful for research purposes, they are currently too expensive for personal use and therefore not suitable as monitoring systems.

Recent developments in smart textiles have made it possible to design pressure sensitive garments. In a study by Gesbert et al. (2020) [27], a pressure sensitive ‘Smart T-Shirt’ (STS) was tested to measure pressure in a scoliosis brace. While the technology is promising, it still lacks significantly in accuracy compared to other pressure sensing solutions. Smart garments may therefore currently be more suitable for applications where the absolute pressure values may be less important, which may be the case for a heart rate monitoring application for example [3].

Monitoring Systems

While most studies have focused on measuring acute effects on the interface pressure, some studies have sought to monitor how pressure may change in the brace throughout the treatment period. Lou et al. (2004) was one of the firsts to implement a load monitoring system in a scoliosis brace [50]. The system used a single piezoresistive pressure sensor (FS01 by Honeywell Inc. [33]) in the thoracic pad and was used to measure the interface pressure over a 4 month period. Zhu et al. (2021) [95] recently developed a similar system for monitoring interface pressure over a 3 month period. The system was based on a different kind of piezoresistive pressure sensors, called a force sensitive resistor or FSR (FSR400, Interlink Electronics Inc. [37]). FSRs are generally very cost effective and are used in a wide range of applications including smart insoles [34, 57] and augmented reality systems[87].

While both studies found that the interface pressure at the thoracic pad may experience a gradual decrease over the treatment period, it was acknowledged by Lou et al. (2011) that it is unknown whether this was caused by an overall decrease or a redistribution of the interface pressure [49].

1.5 PROBLEM STATEMENT AND RESEARCH GOAL

While the measurement of pressure distribution at the brace-torso interface may be a very useful tool to evaluate brace performance, it seems like the current solutions to do so are not suitable for long term monitoring and personal use, due to their complexity and high cost. Studies that implemented a load monitoring system used a very rudimentary setup where only a single pressure sensor was used, thus being unable to describe how a measured change in pressure may have been caused by certain underlying mechanisms. It can therefore be concluded that brace treatment may benefit from a cost effective monitoring device that may be used to evaluate pressure distribution in order to evaluate how the function of the brace may change over time. The main goal of this research is therefore stated as follows:

Design a cost effective pressure monitoring system that may be used for functional evaluation of a scoliosis brace to provide both patient and practitioner with feedback for optimizing brace treatment.

This goal can be broken up into several sub-objectives in order to specify the measurable outcomes defining the framework of this thesis. These objectives are defined as follows:

1. *Define a set of specific evaluation metrics that describe the different functional aspects of a scoliosis brace and can be used to give feedback to both the patient and practitioner for optimizing brace treatment.*
2. *Define the requirements for a pressure monitoring and evaluation system based on the metrics defined in (1.) and results from previous studies.*
3. *Design a cost effective monitoring system including hardware and necessary software that can measure pressure distribution at the brace-torso interface based on requirements defined in (2.).*
4. *Estimate the uncertainty in the measured pressure in terms of random and systematic error.*
5. *Validate the system's feasibility by evaluating brace function for a real subject based on aforementioned evaluation metrics.*

1.6 THESIS STRUCTURE

Based on the previously stated sub-objectives of this research, the structure of this thesis can be defined. The research done for this work is divided into a total of 7 chapters, a discussion and a conclusion. **Chapter 1 & 2** are meant to provide the required theoretical background while also introducing definitions that provide a certain framework this research is based on. This framework and previous studies regarding this topic formed the basis for the list of system requirements that is defined in **Chapter 3**. The following two chapters (**Chapter 4 & 5**) then describe the design of the prototype and a processing method necessary for obtaining the required three dimensional geometry of the system. Testing the prototype is then discussed in **Chapter 6**, where a model is described that is used for calibration of the included pressure sensors. This chapter also provides insight into the sensor behavior and an estimate of the measurement uncertainty. The last chapter (**Chapter 7**) describes the validation of the entire system and combines all the research to evaluate the function of a lumbar pad in a Cheneau type scoliosis brace. This is then followed by a discussion of the research results and recommendations for further research in **Chapter 8** and a final conclusion in **Chapter 9**.

2

METHODS FOR FUNCTIONAL BRACE EVALUATION

2.1 INTRODUCTION

As described in Chapter 1, the function of the brace is to apply pressure in specific areas on the torso, resulting in a correction of the spine. It is assumed that when correction is achieved continuously over a prolonged period of time, it results in symmetric growth of the spinal column, thus preventing curve progression. Monitoring the pressure at the brace-torso interface may provide valuable information indicating potential changes in brace function. This may help the patient to optimize compliance quality, while also providing the practitioner with more insight in the treatment, which may be used to optimize the design of the brace and ensure adequate intervention when necessary. However, as the brace pressure is not directly related to its corrective effect, a set of metrics need to be defined that capture different aspects related to the function of the brace. These metrics were categorized according to the dimensions required for their evaluation (time not included). This resulted in a *one*, *three* and *four* dimensional evaluation, with metrics calculated from pressure magnitude (p), pressure distribution (p, x, y) and projected pressure distribution (p, X, Y, Z). This chapter discusses the relevance and application of each evaluation type and its associated metrics.

2.2 ONE DIMENSIONAL EVALUATION METRICS

The most straightforward way of evaluating and monitoring brace function is by analysis of the *mean pressure magnitude* and *pad pressure variance* at the pressure pads. Measuring the mean pressure magnitude is a simple but effective method for evaluating passive brace contributions. It can be used to provide the patient with feedback, which they can use to tune the strap tension to match the prescribed reference pressure as close as possible. The reference values for the pressure distribution should ideally be obtained in combination with radiologic assessment, which should validate that a certain pressure is related to the desired correction. As brace pressure is assumed to change constantly as a result of different movements and postures, feedback may also provide the patient with more insight in when the function of the brace may be compromised. This should make the patient more aware of their posture, thus improving the brace treatment as a result.

Monitoring the mean pressure magnitude should also be useful to the practitioner as it may provide them with remote and continuous access to data representing the passive brace contributions. Potential irregularities that may compromise the function of the brace may be reflected by changes in the mean pressure magnitude. Additionally, the practitioner may also be provided with information regarding the pad pressure variance, which is a metric that may be used to quantify the degree of local pressure variance. This may be useful as it may provide information regarding local pressure points in the brace that may not only cause discomfort to the patient, but may also alter the function of the brace.

Mean Pressure Magnitude

The mean pressure P_{avg} at a specific time instance t_i can be calculated by taking the mean of all the measured pressure values at that specific pad location:

$$P_{avg}(t_i) = \frac{\sum_{k=1}^{N_{sens}} p_k(t_i)}{N_{sens}} \quad (2.1)$$

with $p_k(t_i)$ being the measured pressure value at the k th sensing element of the in total N_{sens} amount of sensing elements. For monitoring purposes, the moving average of this mean pressure $P_{avg,ma}$ over a specific time interval should provide information on the the mean pad pressure magnitude, uninfluenced by pressure differences caused by the expansion of the chest due to respiratory movement. The time interval should therefore be $n\hat{T}_{bc}$, with n being a positive non-zero integer and \hat{T}_{bc} being the mean period of a breathing cycle, defined as the time required for full inhalation and full exhalation. The moving average of the mean pressure magnitude at a specific time instance t_m , calculated over the last l data points, sampled every T_s with $lT_s = n\hat{T}_{bc}$ is calculated as follows:

$$P_{avg,ma}(t_m) = \frac{\sum_{i=m-l+1}^m P_{avg}(t_i)}{l} \quad (2.2)$$

Pad Pressure Variance

The pad pressure variance s_p^2 at a specific time instance t_i is calculated using the previously defined mean pressure magnitude P_{avg} and the total of N_{sens} individual pressure measurements p_k :

$$s_p^2(t_i) = \frac{\sum_{k=1}^{N_{sens}} (p_k(t_i) - P_{avg}(t_i))^2}{N_{sens} - 1} \quad (2.3)$$

2.3 THREE DIMENSIONAL EVALUATION METRICS

For a more detailed evaluation the measurements can be related to their associated relative spatial location, thus resulting in a two dimensional pressure distribution. By interpolating discrete pressure measurements, an estimation can be made of the pressure distribution over the pad surface. This may be visualized using a heat map which may be used to identify the specific location of potential pressure points. Additionally, the pressure distribution may also be translated to a more quantitative metric, namely the *center of pressure* or *COP*. The COP is the average location of where the total sum of the pressure acts on a body and can be seen as the point of application of the equivalent brace forces, which quantifies the resulting force at each pressure pad.

While the COP is useful for translating the pressure distribution to equivalent brace forces, it can also be used directly to assist the practitioner in fitting the brace. The fit of the brace may be validated by using the COP to evaluate the effect of certain postures and movements. As the function of the brace is related to an adequate magnitude and direction of the equivalent brace forces, the COP should remain within a certain margin of its ideal location irrespective of the posture the patient is in. This metric may also be monitored throughout the treatment period, which should add to the previously defined two metrics. As such, the practitioner is given an almost complete overview of potential changes in the passive contribution of the brace.

Center of Pressure

As the COP represents the average location of where the total sum of the pressure acts on a two dimensional surface [58], a COP_x and a COP_y component can be computed. Mapping the relative two dimensional surface of interest onto a three dimensional surface may then yield the three dimensional global COP components COP_X , COP_Y and COP_Z . The general equation for the x-component of the COP in an area where pressure is described by $p(x, y)$ is given as follows:

$$COP_x = \frac{\int xp(x, y)dx}{\int p(x, y)dx} \quad (2.4)$$

The y-component can be computed in a similar way by substituting x with y and dx with dy . In practice however, the pressure is measured with a finite amount of sensing elements. Therefore, the relations above should be discretized to account for this. In addition to this, in a monitoring scenario, the pressure distribution is time dependent, which means that the pressure at a certain time instance t_i for sensor k , located at (x_k, y_k) is described by $p_k(t_i)$. The discrete x-component of the center of pressure \hat{COP}_x at time instance t_i can be computed as follows:

$$\hat{COP}_x(t_i) = \frac{\sum_{k=1}^{N_{sens}} x_k p_k(t_i)}{\sum p_k(t_i)} \quad (2.5)$$

Again, the y-component \hat{COP}_y is computed similarly by simply substituting x for y . Note that for further reference the hat (^) denoting that the computed COP component is discrete will be omitted for simplicity.

2.4 FOUR DIMENSIONAL EVALUATION METRICS

The highest level of detail is achieved by computing the *equivalent bending moments*, which is a metric that is most closely related to the function of the brace. These equivalent bending moments are the moments induced by the brace and should be sufficiently large enough to counteract the *spinal bending moments* which are caused by the asymmetric gravitational loading of the vertebrae. The spinal bending moments are essentially a way of expressing the asymmetric pressure distribution on the cranial and caudal surfaces of the vertebral body (see Figure 2.1). These surface include the pressure sensitive growth plates that facilitate the growth of the vertebra. In a normal spine, the center of rotation of the vertebrae should coincide with the centroid of the intervertebral discs (IVD), resulting in a sagittally symmetric pressure distribution on the growth plates with symmetric growth as a result. In the case of scoliosis however, the center of rotation is shifted a distance d_r from the centroid of the intervertebral disc [39]. These spinal bending moments are the result of a shifted *center of rotation* (COR) in the scoliotic spine, which in a normal spine should coincide with the centroid (GC) of the intervertebral discs (IVD). The shifted center of rotation causes the reaction force $\vec{F}_{r, Vxy}$ of the adjacent vertebrae to also deviate a distance $\vec{d}_{r, Vxy}$ from the intervertebral disc centroids, thus resulting in an (equivalent) spinal bending moment $\vec{M}_{spine, Vxy}$ with respect to the intervertebral disc centroid Vxy :

$$\vec{M}_{spine, Vxy} = \vec{d}_{r, Vxy} \times \vec{F}_{r, Vxy} \quad (2.6)$$

These spinal bending moments can be calculated with respect to both the inferior as well as the superior adjacent intervertebral disc centroids. Note that the arrows indicate that these quantities are vectors, which can be calculated with respect to any (three dimensional) frame. Brace pressure measurements can be translated to *equivalent brace forces* from which the equivalent bending moments can be calculated for each vertebra individually, provided that the three dimensional spatial locations of the vertebrae, intervertebral discs and the brace pressure pads are known.

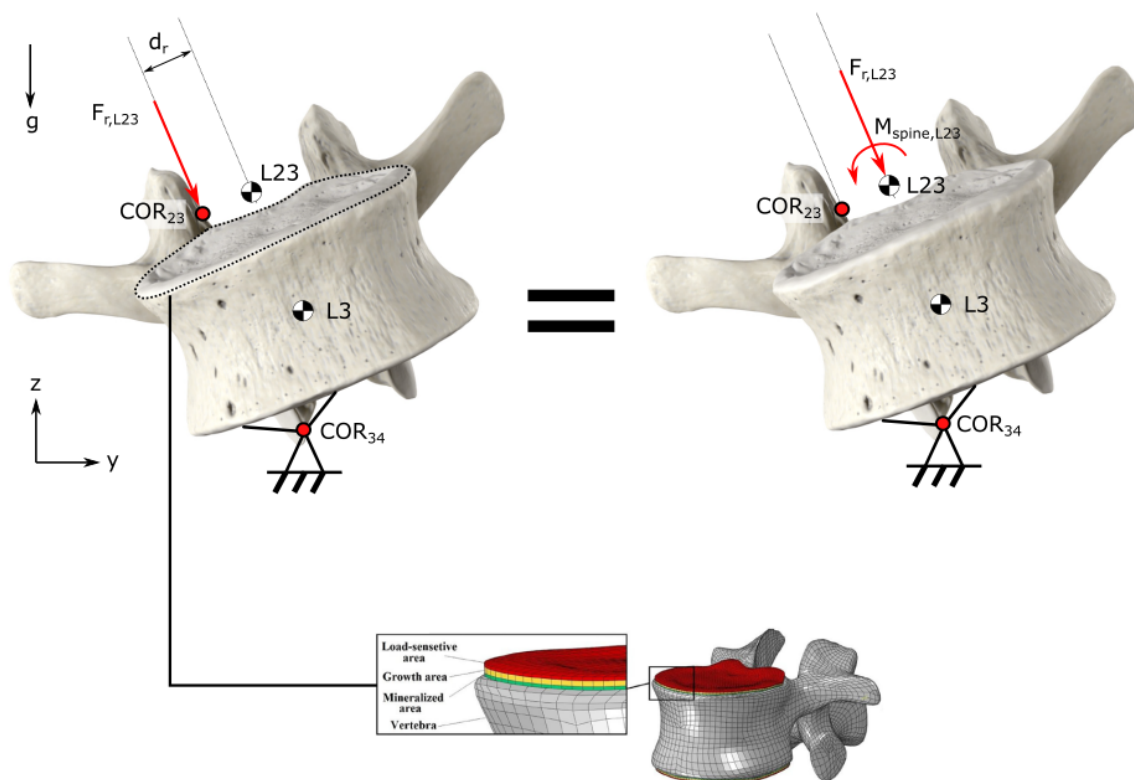


Figure 2.1: A figure illustrating how an asymmetric pressure distribution on the cranial growth plates of the L₃ vertebra in a scoliotic spine can be expressed as a reaction force $F_{r,L23}$ perpendicular to the vertebra surface acting through the center of rotation COR_{23} at a distance d_r from the intervertebral disc centroid of the L₂₃ vertebra. This can be translated to an identical reaction force through the intervertebral disc centroid and a spinal bending moment $M_{spine,L23}$. Note that the center of rotation is shifted with respect to the centroid location for both the L₃₄ (COR_{34}) and the L₂₃ (COR_{23}) intervertebral discs. Vertebra pictures were obtained from [69] and modified with additional drawings and the mesh model of the vertebra illustrating the growth plates was obtained from Kamal et al. (2019) [39].

When used in combination with radiologic assessment, the practitioner is given insight in the relation between pad pressure and correction of the spine. This may be useful to determine how to modify the brace to maximize its corrective effect. During follow-up appointments, analysis of the equivalent bending moments may provide the practitioner with a detailed representation of the function of the brace, which may be used as an additional metric to assess the effectiveness of the treatment. This should minimize the potentially subjective nature of brace design by allowing the practitioner to make informed decisions on how, when and where to modify the brace.

While the equivalent bending moments provide the most accurate description of the brace function, it may not be possible to reliably monitor this continuously throughout the treatment period. The reason for this is that the bending moments are computed using the spatial geometry of the patient's torso and spine. Growth of the spinal column and other morphological adaptations/changes may cause the spatial geometry to change over time. An accurate computation of the equivalent bending moments should therefore be based on relatively recent data representing the patient's morphology.

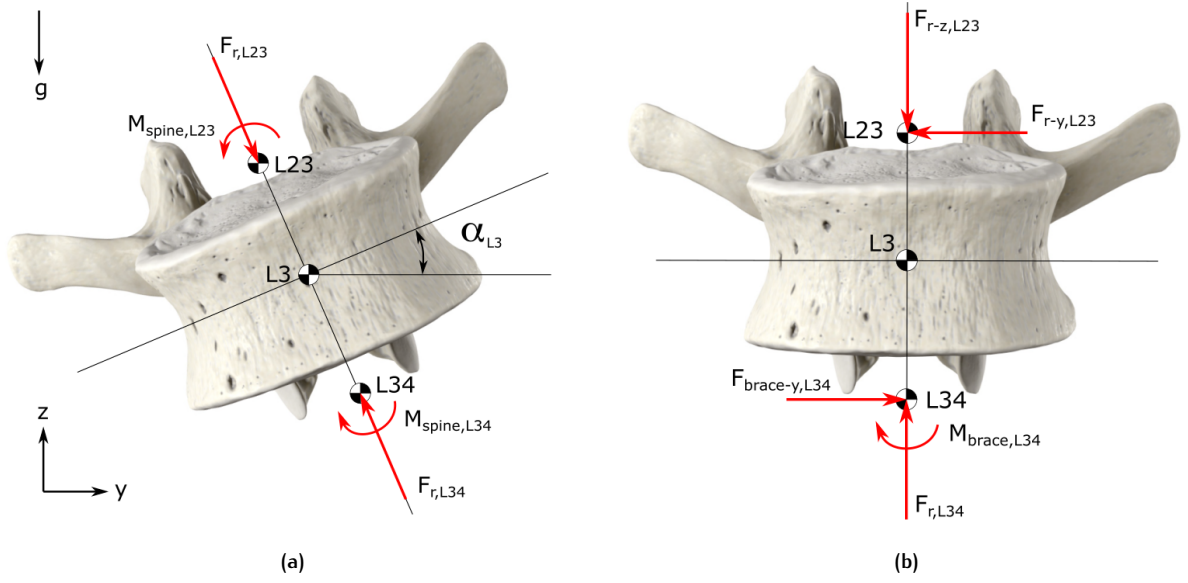


Figure 2.2: Figure illustrating free body diagrams of an uncorrected vertebra (a) and a corrected vertebra (b) with zero mass. (a) The free body diagram of the L3 vertebra in a scoliotic spine that is tilted by an angle α_{L3} ($\alpha_{L4} < \alpha_{L3} < \alpha_{L2}$) illustrates the reaction forces $F_{r,L23}$ and $F_{r,L34}$ through their associated intervertebral disc centroids L23 and L34 and the spinal bending moments $M_{spine,L23}$ and $M_{spine,L34}$ as a result of the shifted center of rotation (see Figure 2.1). (b) The free body diagram shows the corrective effect of the brace resulting in an equivalent bending moment $M_{brace,L34}$ with respect to intervertebral disc centroid L34 and an equivalent brace force $F_{brace-y,L34}$ and an opposite but equal lateral reaction force $F_{r-y,L23}$. This results in the reaction forces $F_{r,L23}$ and $F_{r,L34}$ to act through their associated intervertebral discs L23 and L34. Vertebra pictures were obtained from [69].

Lateral, Sagittal and Axial Bending Moments

The bending moment over a vertebra V_{xy} resulting from an equivalent force \vec{F}_X at pressure pad X is calculated using the distance vector $d_{X,V_{xy}}$, which is the distance from the COP at pad X to the center of rotation of vertebra V_y . Assuming the vertebra rotates about its inferior IVD centroid, the equivalent bending moment $M_{X,V_{xy}}$ resulting from the equivalent brace force at pad X can be calculated as follows:

$$\vec{M}_{X,V_{xy}} = \vec{d}_{X,V_{xy}} \times \vec{F}_X \quad (2.7)$$

The total resulting equivalent bending moment acting on a specific vertebra V_y with respect to IVD V_{xy} can be computed as the sum of all equivalent bending moments resulting from the pressure applied at all pressure pads in the brace. The resulting (immediate) correction depends on the spinal stiffness, which is a result of the combined intervertebral disc stiffness k [Nm/rad]. A vertebra V_y that is rotated by an angle α [rad] with respect to vertebra V_x requires an equivalent bending moment of $\vec{M}_{brace,V_{xy}} = \alpha/k$ in order to nullify the spinal bending moment. Assuming the brace applies pressure at the pelvic (pv), lumbar (lb), thoracic (th) and axillary (ax) pads, the resulting equivalent bending moment over a vertebra V_y can be denoted as follows:

$$\vec{M}_{brace,V_{xy}} = \vec{M}_{pv,V_{xy}} + \vec{M}_{lb,V_{xy}} + \vec{M}_{th,V_{xy}} + \vec{M}_{ax,V_{xy}} \quad (2.8)$$

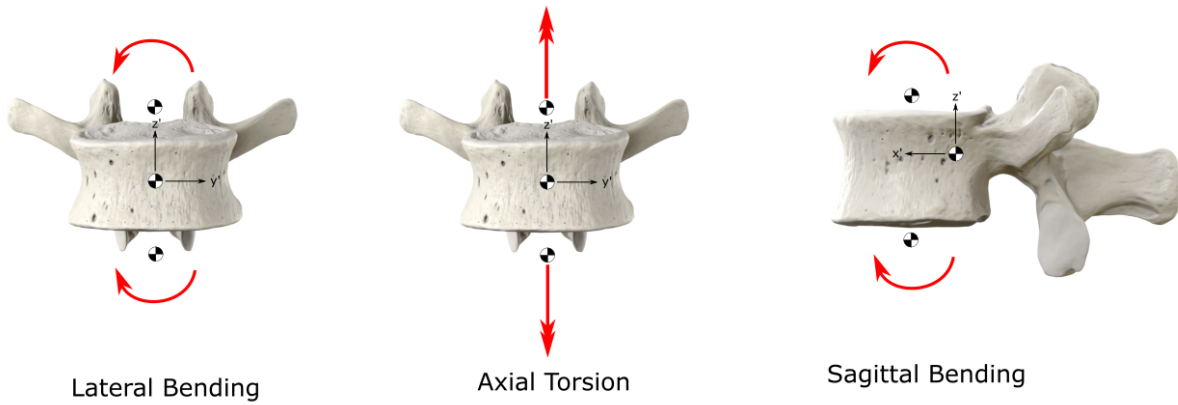


Figure 2.3: The figure illustrates three bending directions with respect to the intervertebral discs: a lateral bending moment, axial torsion and sagittal bending. It should be noted the surrounding musculature and the facet joints play a significant role in stabilizing the spine and limiting these bending moments. Vertebra pictures were obtained from [69].

The total equivalent bending moment can be broken up into its x , y and z component with respect to a local fixed frame for vertebra V_y , which result in a lateral, sagittal and axial bending component respectively as depicted in Figure 2.3. Note that the sagittal bending is also referred to as flexion/extension of the spine. As the main function of the brace is to counteract the lateral and axial spinal bending moments, one is mainly interested in the x and z component of $\vec{M}_{brace, V_{xy}}$, i.e. the lateral and axial equivalent bending moments.

3 | SYSTEM REQUIREMENTS

The requirements for the monitoring system are focused primarily on its functional aspects. The term *system* is used to articulate that the design includes the electronic hardware required for pressure measurement, but also methods for data-processing to relate these measurements to different functional aspects of the brace. The system requirements can therefore be defined to be hardware related (H), software/data-processing related (S) or both (H/S). The requirements were defined as follows:

- **Spatial Resolution of at least 0.15cm^{-2} - (H)**

The spatial resolution of a sensor array is defined by the amount of sensing elements that are deployed in a specific area and may be quantified as cm^{-2} . As the complexity of the system is preferred to be as little as possible, the minimum required spatial resolution should be determined. Wong et al. (1998) & (2000) [89, 90] used an array of electrohydraulic sensors with a spatial resolution of only 0.15cm^{-2} to show how strap tension affects the direction of the resultant forces in the pressure areas of a Milwaukee brace. It is therefore believed that the same spatial resolution would suffice as a good starting point for the current system, while keeping its complexity to a minimum.

- **Sampling Frequency of at least 10Hz - (H)**

As mentioned in Chapter 1, braces are often designed to translate respiratory movement to additional pressure at the pressure pads. By leaving room for expansion opposite to these pressure pads, the patient is encouraged to actively move away from these high pressure areas, thus having an additional corrective effect. The effect of respiratory mechanics on the function of the brace, reflected by changes in mean pressure, pressure distribution or equivalent bending moments, should therefore not be neglected as it may provide valuable information on the self corrective effect the brace may induce. The sampling frequency should therefore be sufficiently high enough for this effect to be accurately evaluated. Taking into account that the average respiratory rate is between 12 and 20 breaths per minute, the maximum signal frequency is estimated to be approximately 0.33Hz . The Nyquist criterion states that the sampling frequency should be greater than twice the maximum signal frequency [45], which would be 0.66Hz . This would however result in a rather poor representation of the signal of interest. A minimum sampling frequency is therefore chosen of 10Hz , which is believed to be sufficiently high enough to yield an accurate representation of the pressure signal resulting from respiratory movement. As most sensors (including piezoresistive and capacitive pressure sensors) require analog to digital (AD) conversion, the maximum sampling frequency is often limited by the AD converter that is used. However, when multiplexing is required, which is the case for a sensor array, the maximum sampling frequency is effectively limited by number of sensors.

- **Effective Range of $0 - 30\text{kPa}$ - (H/S)**

Based on a total of 12 independent studies [2, 10, 20, 26, 27, 50, 52, 63, 86, 89, 90, 95] that focused on analyzing brace pressure for different types of rigid scoliosis braces, a 95% confidence interval was defined of $8.5 - 41\text{kPa}$. With a mean of $25 \pm 3.6\text{kPa}$ and a median of 14kPa , it is assumed that the measurements are more likely to be towards the lower end of this range. This provides information for the range in which the sensors need to be calibrated in order to prevent clipping or pressure not reaching the minimum discernible signal value¹. There may always exist a trade-off between the width of the range and the measurement resolution², where a larger range will

¹ An input signal with a signal to noise ratio (SNR) being smaller than 1.

² The minimum discernible difference in the output signal

often lead to a decrease in resolution. A range of approximately $0 - 30kPa$ is therefore chosen as optimal for this system. The range is determined by choosing the appropriate components and calibrating the sensors for operation in the required range.

- **Cost Effective System Components - (H)**

This requirement was deliberately not quantified as the cost of a prototype may always be difficult to predict and will often be a higher than expected due to the cost of single components being higher than their bulk price. However, choices should be made to keep the cost of the main system components as low as possible. Prices of commercially available systems currently start at around €4000 [43]. The prototype should illustrate the feasibility of a cost effective alternative.

- **Semi-Remote System Operation - (H)**

While the prototype does currently not have any strict requirements for its mass and dimensions, it should still allow the patient to move freely in order to evaluate brace function in different positions. The system should therefore be able to operate semi-remotely, implying that data transfer may still be established using a wired connection, which should not interfere with the patient's movement freedom.

- **Three Dimensional Mapping Method based on Available Resources. - (S)**

As mentioned in the previous section, the mean pressure and the pressure distribution do not provide all information required for a thorough evaluation of brace function. When interested in the effect of the brace, one needs to know where the pressure is applied relative to the spinal column. Therefore, a method should be developed that may be used for mapping the pressure measurements onto the torso surface, while also providing an estimate of its location relative to the spinal column. The latter requires some estimate of the geometry of the spine, which currently requires sophisticated imaging systems to obtain. If a system is to be widely adopted, it should not require any additional equipment that may not always be available. Therefore, a method for 3D interpretation of 1D/2D pressure measurements should be developed based on currently available resources only. This implies a standard AP radiograph and a CAD model of the brace, which is obtained using photogrammetry.

The following two chapters will discuss the monitoring system that was designed based on these requirements. This includes the architecture of the system and the electronic hardware of the prototype (Chapter 4) and a method for mapping and reconstruction of relevant geometry (Chapter 5).

4 | PROTOTYPE DESIGN

4.1 INTRODUCTION

This chapter discusses the design of the different components of the pressure monitoring system. The basic components of the system were identified to be a sensing element, a microcontroller and a PC for the more complex computations. As mentioned in Chapter 1, the measurement of pressure distribution requires an array of pressure sensors. This can either be a matrix array of interconnected sensing elements or a discrete array of individual pressure sensors. As the latter is often used for COP trajectory analysis studies [34, 57], this will be used for this application as well. The output of any pressure sensor is inherently analog and requires analog to digital conversion for further processing. This can be done using a microcontroller. As microcontrollers usually only allow for a limited amount of simultaneous analog to digital conversions, multiplexing is required. When only a few analog signals have to be converted, the integrated multiplexer of the microcontroller can be used. However, when this is not enough, an external analog multiplexer may be used to expand the microcontroller's multiplexing capabilities. Figure 4.1 shows a diagram illustrating the basic functionality of the system.

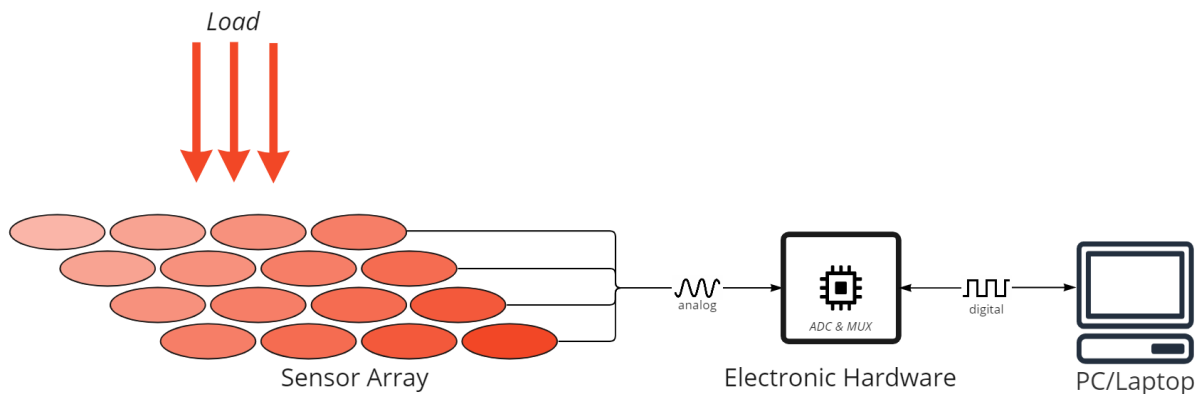


Figure 4.1: Diagram illustrating the basic functionality of the system. A load applied to the sensor array results in an analog signal. A microcontroller and potentially an additional multiplexer are then required for multiplexing (MUX) and analog to digital conversion (ADC).

Section 4.2 will discuss the design process of the electronic hardware from identifying the required main components and the system architecture design to the final PCB and housing design. Section 4.3 will discuss the design process for finding an appropriate integration of the sensors with the final sensor pad as a result.

4.2 ELECTRONIC HARDWARE DESIGN

4.2.1 Design Process

The electronic hardware was designed through an iterative process, for which the course was partially determined by the choice of the main components. This implied that the sensors were chosen first and the other components were chosen accordingly. The rest of the design was built around these

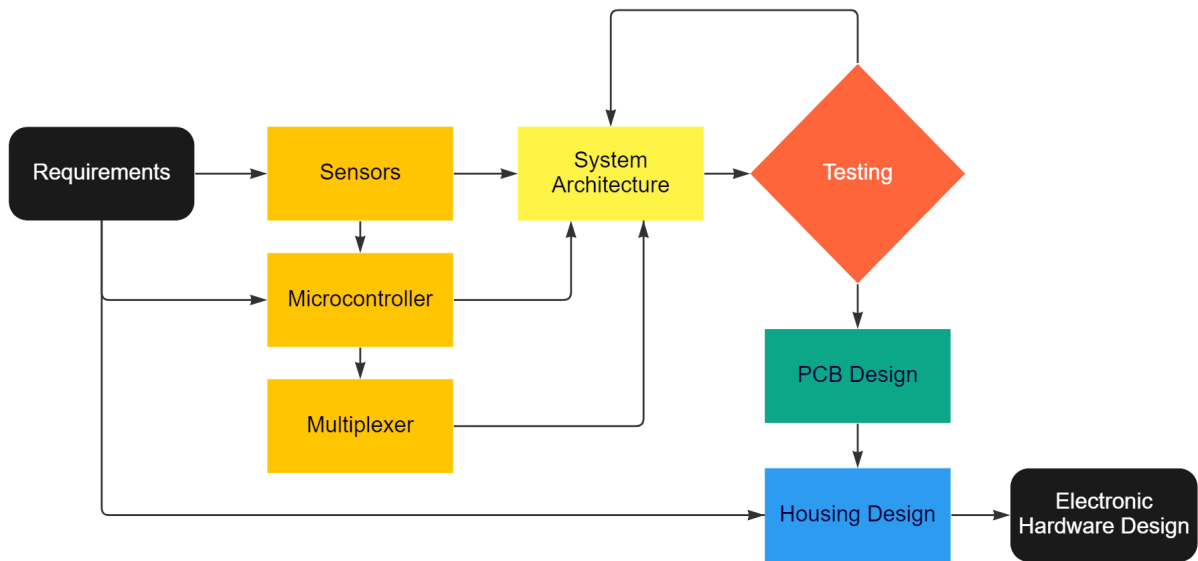


Figure 4.2: Flowchart illustrating the design process for translating the system requirements to the design of the electronic hardware. The main components were chosen based on the previously defined system requirements. The system architecture was then defined through an iterative design process. This was used for the design of the PCBs which were then integrated in a housing for which the design was partially based on the system requirements.

main components. Depending on the application, the manufacturer of the sensors often recommends implementation in a specific conditioning circuit. While this does not necessarily mean that this is the optimal method for implementation, this research followed these recommendations for a first version of the prototype. It should be stressed that the focus of this research was to illustrate a concept, where the focus was on ensuring the prototype could fulfill its basic requirements. Figure 4.2 illustrates the design process that was used to arrive at the final design of the printed circuit boards for integration of all the electronic hardware required for the system.




The iterative part of this design process was required to define an appropriate system architecture. This refers to the correct implementation and interconnection of the different system components. This was then used to design the *printed circuit boards* (PCBs) that facilitated a reliable and robust connection of the components. The PCBs were then integrated and connected in a protective housing, yielding the electronic hardware of the prototype to which the sensor pad could be connected. Testing and prototyping of the sensor pad, which will be discussed in Section 4.3, was done using the electronic hardware that will be discussed in the following section.

4.2.2 Main Components

Pressure Sensors

The most essential components of the pressure monitoring system are the pressure sensors. For sensing pressure at an interface between two surfaces, the sensor needs to be as thin as possible so as not to influence the measurement. Most biomechanical pressure sensing applications for measuring interface pressure therefore use either capacitive or piezoresistive pressure sensors. These applications include measurement of plantar pressure or pressure at the interface between orthosis or prosthesis and the skin. A total of three different sensors were considered for this prototype, with the other components mostly being determined by this choice. This included two different types of piezoresistive sensors, the FSR402 by Interlink Electronics and Flexiforce Standard Model A201 by Tekscan Inc. , and one capacitive sensor, the S15-45N by Singletact. The sensors were compared based on their performance reported in the datasheets, their cost and their relevant applications in current literature. The latter was done using a quantitative analysis where the number of results were compared when searching

Table 4.1: Specifications of the FSR402 by Interlink Electronics, the Flexiforce A201 by Tekscan and the S15-45N by Singletact based on information found in datasheets, on PubMed and from electronic component retailer Antratek [4, 5, 37, 74]. The repeatability, hysteresis and linearity are given in percentage of their full scale range.

	FSR402 (Interlink Electronics)	Flexiforce A201 (Tekscan)	S15-45N (Singletact)
			
Sensing Technology	Piezoresistive (shunt)	Piezoresistive (thru)	Capacitive
Repeatability [%]	< $\pm 6\%$	< $\pm 2.5\%$	< $\pm 1\%$
Hysteresis [%]	< 10%	< 4.5%	< 4%
Linearity [%]	N/a	< 3%	< 2%
Thickness [mm]	0.35	0.23	0.35 (+3.5)
Range [kPa]	0 – 197	0 – 389	0 – 64
Relevant Applications [# Results]	73 ¹	24 ⁸	19
Cost [€]	€7,00	€22,00	€23,00 (+€28,70)

((FSR) AND pressure) AND sensor, ((Flexiforce) AND pressure) AND sensor and ((Singletact) AND pressure) AND sensor in PubMed. This was assumed to provide an accurate representation of their use in biomechanical applications.

Based on the data reported in Table 4.1 it can be concluded that the Singletact S15-45N, seems to be the best performing sensor of the three, with the Flexiforce A201 as a close second. However, as was mentioned in Chapter 1, capacitive pressure sensors tend to be quite complex in their application. Singletact therefore recommends using the sensor in combination with a specifically designed electronic circuit board required for signal conditioning, which is to be connected directly to the tail-end of the sensor. This increases the cost to more than €51,70 per sensor and increases their thickness, significantly limiting its application [74]. As the sensor is relatively new, it is not surprising that it has not been reported in many studies. However, it is preferred to implement a sensor that has been proven to be usable for similar applications. In one specific study by Schoepp et al. (2018) the Singletact S8-10N sensor was compared with the FSR400 for implementation in a mechanotactile feedback system for myoelectronic prostheses [70]. The study recommends the Singletact sensor over the FSR400 when a high single sensor accuracy is required. While the accuracy is certainly important, it should be noted that multiple sensors are required for measurement of pressure distribution. The relatively high cost of the Singletact S15-45N and the increased thickness as a result of the directly connected circuitboard therefore makes it an unattractive choice for this application.

When comparing the FSR402 and the Flexiforce A210, it can again be found that the latter seems to outperform the FSR402 [37, 78]. However, both sensors have been used in a wide variety of biomechanical applications, including COP computations resulting from plantar pressure. Hu et al. (2018) did this using 24 integrated FSR402 pressure sensors [34], with 12 sensors in each insole, and Muzaffar et al. (2020) used a total of 12 integrated Flexiforce A210 pressure sensors to compute COP trajectories [57]. Both sensors are also relatively simple in their implantation compared to the Singletact sensor. Swanson et al. (2019) compared the two sensors for measurement of interface pressure in lower limb prosthetics [76]. The study compared the accuracy of the sensors using a protocol (walk-sit-stand) defined to simulate everyday movements with the prosthetic limb and found no statistical difference between the two sensors. The study illustrates that other unforeseen factors may result in a comparable accuracy. While the FSR402 experienced significantly more drift than the Flexiforce sensor, it was

found that this follows a more repeatable pattern. Florez et al. (2010) showed that this drift is related to creep and can easily be compensated for [25].

In conclusion, it was found that the low price and the presumably comparable practical accuracy of the FSR402, made it the optimal choice for this application.

Microcontroller and Multiplexer

As further research may find that a different microcontroller may be preferred for expanding monitoring capabilities it was decided that an external multiplexer should be used to create a more modular design where the electronics can be used with any other microcontroller if necessary. A 16:1 analog multiplexer (CD74HC4067 by Texas Instruments [81]) was chosen for this purpose, which requires a 4-bit binary code to be controlled and can be used to switch between 16 analog signals. This was found to be optimal considering that a spatial resolution of 0.15cm^{-2} would result in a covered area of 106.7cm^2 if 16 sensors were to be connected¹. It was assumed that this would be sufficient to cover any pressure pad area in the brace. Section 4.2.4. will discuss how the multiplexer and additional conditioning circuit components are integrated together in a PCB that allows for connection of up to 16 FSRs.

Two standard but quite diverse microcontrollers were considered for controlling the multiplexer and facilitating the analog to digital conversion, namely the Arduino Uno R3 [7] and the Arduino Mega 2560 [6]. Both microcontrollers have a 10 bit analog to digital conversion resolution, meaning that the analog signal is converted in to a total of $2^{10} = 1024$ steps. Assuming that the prototype is to measure at four pressure pads in the brace, deploying a total of 64 FSRs, a total of 16 digital pins (20 when also considering enable pins) and 4 analog pins would be required. This requires more digital pins than the Arduino Uno has and the choice was therefore made to use the Arduino Mega 2560 instead. It should be noted that both microcontrollers allow for a maximum sampling frequency of 9615Hz . With a maximum of 64 connected FSRs this would imply a maximum sampling frequency of 150Hz , which still far exceeds the required 10Hz . However, as will be mentioned in the next section, the limiting factor for the sampling frequency was found to be the software rather than the hardware of the system.

4.2.3 System Architecture

Conditioning Circuit and Power Supply

Having chosen the main system components, the next step was to define an appropriate system architecture. This implies the integration of all necessary system components to yield a functional system, which requires an appropriate signal conditioning circuit for the sensors and a power supply for powering all components with the required voltage. A process of trial and error was found to be necessary for finding an appropriate method for integrating all required components.

Analog sensors, like the FSR402 chosen for this application, require implementation in a conditioning circuit for the change in the electrical property to be measured. In the case of piezoresistive sensors, this often implies that the change in resistance is translated to a voltage signal. The analog voltage signal is then discretized and translated to a digital signal using an AD-converter. The conditioning circuit is designed to ensure the sensor can measure within the desired range. Interlink suggests a number of different circuits, including a voltage divider circuit and a current-to-voltage converter. The latter was found to be optimal for this purpose as it allows the sensitivity of the FSR to be carefully tuned if necessary, depending on the resistance value for R_g . A current-to-voltage converter circuit is given in Figure 4.4. In theory, a fixed resistor value would have been sufficient. However, the datasheet included in the integration guide reports a relatively high part-to-part error of up to 25%. Based on this and some preliminary quality testing of the FSRs, the choice was therefore made to implement $10\text{k}\Omega$ variable resistors, which would allow for tuning of R_g between 0Ω and $10\text{k}\Omega$. For the operational amplifier, the MCP6004 by Microchip Technology Inc. [56] was chosen, which is a general purpose

¹ 16 sensors with 0.15 sensors per cm^2 is $(16/0.15)\text{cm}^2 = 106.7\text{cm}^2$

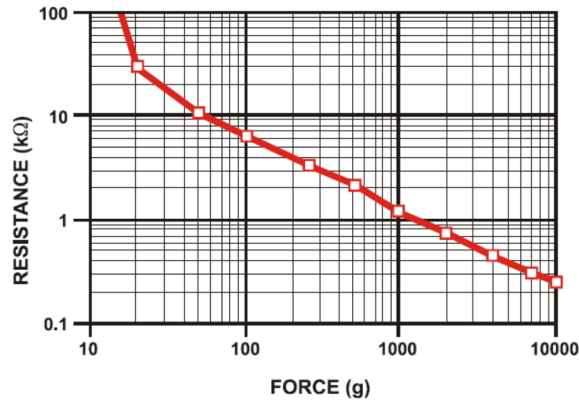


Figure 4.3: The relation between force and resistance for the FSR402 as given in the Interlink Electronic's FSR Integration Guide [37].

quad-opamp, meaning that a total of four operational amplifiers are deployed within the same chip. The relation between the resistance value of the sensor R_{FSR} and the output signal V_{out} is given as follows:

$$V_{out} = -V_{ref} \frac{R_g}{R_{FSR}} \quad (4.1)$$

A negative reference voltage therefore has to be chosen to yield a positive voltage swing. The value for R_{FSR} approaches infinity when unloaded and can be approximated as following an inverse power law characteristic (roughly $1/R$) [37] (see Figure 4.3). In an unloaded condition, this results in a 0V output signal. Its maximum output is determined by the resistance value for R_g and the reference voltage value V_{ref} . Some qualitative tests were performed with the sensors integrated in the circuit given in Figure 4.4 to obtain acceptable values for V_{ref} . It was found that a reference between $-1.7V$ and $-1V$ seemed to be an acceptable range when tested with $R_g = 4.7k\Omega$. These tests were required to ensure the current remained below the limit of $1mA$ when loaded with a 1500g load (see Figure 4.12).

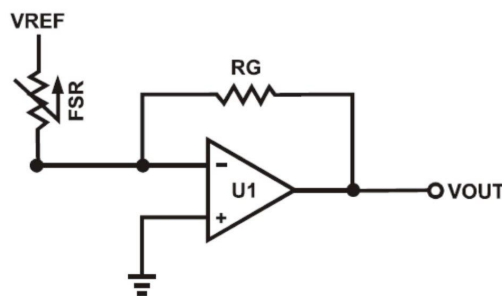


Figure 4.4: A current-to-voltage converter circuit that will be used for this application as a conditioning circuit. Image obtained from Interlink's FSR INtegration Guide [37].

As the other components require a positive voltage (+5V), a dual power supply is necessary where the positive terminal of one of the supplies is connected with the negative terminal of the other, resulting in a negative voltage rail, a ground rail and a positive voltage rail. For the system to be able to operate semi-remotely, as stated in the requirements, it was decided that it should have an integrated power supply to provide power to all components. This meant that an additional voltage regulator circuit had to be designed in order to produce a constant voltage from power supplied by a 7.2V NiMH [68] and a 3.6V NiCd [67] rechargeable battery pack. These batteries were chosen over lighter lithium-ion alternatives for safety reasons [18]. The circuit required a total of two different voltage regulators: the

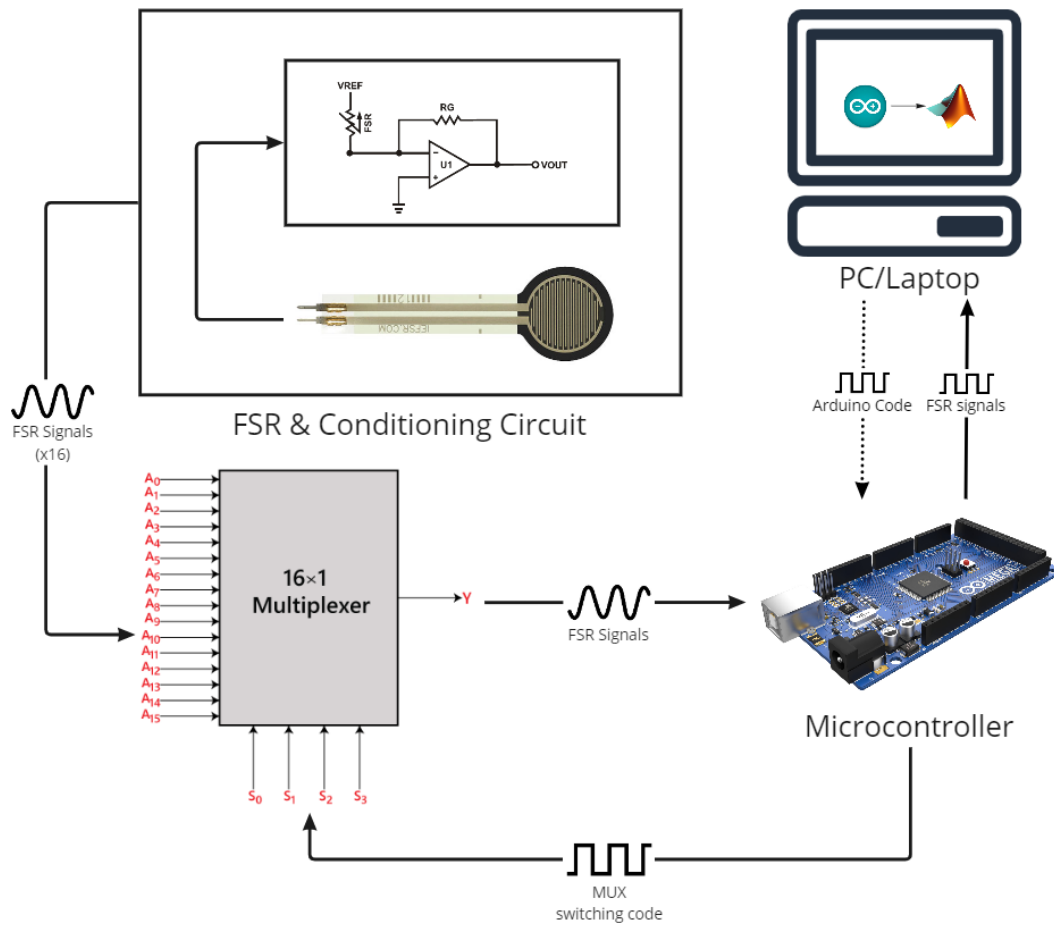


Figure 4.5: A diagram illustrating an overview of the system architecture. The pressure sensors require integration in a conditioning circuit. A multiplexer (MUX) is then used to switch between the sensors. The multiplexer is controlled using a microcontroller which is also used for analog to digital conversion (ADC). The code that is used to control the multiplexer is uploaded once (dotted line). The microcontroller may then send the data to the PC every $1/f_{sample}$. The square wave denotes a digital signal and the sinusoidal wave an analog signal.

LM78M05 by Texas Instruments [82] was used to produce a constant +5V output and the LM317to by Texas Instruments [83] variable voltage regulator was used to obtain the $-1.5V$ reference voltage. The voltage regulator circuit that was designed for this purpose can be found in Appendix B.1.

System Overview and Basic Operation

A complete overview of the final system architecture is given in Figure 4.5. The diagram illustrates the connection of a single multiplexer, which can switch between 16 FSRs, each integrated in a conditioning circuit as discussed in the previous section. The board is controlled using code written in the standard Arduino IDE software, which is uploaded to the board once (hence the dotted line). Port manipulation is used to send a binary code switching between each of the FSRs connected to the multiplexer. A single analog signal is then sent to the microcontroller and the PC at every f_{sample} . The data is then recorded using serial communication in MATLAB. As mentioned in Chapter 1, the maximum sampling rate depends on the number of sensors in the array and the hardware that is used. However, it was found that this maximum sampling rate was limited by MATLAB's serial communication interface. The sensor pad, which will be discussed in Section 4.3, was designed with an integrated array of 15 FSRs. The maximum sampling rate that the array could be sampled was found to be limited to 22.2Hz, which is still acceptable according to the requirements.

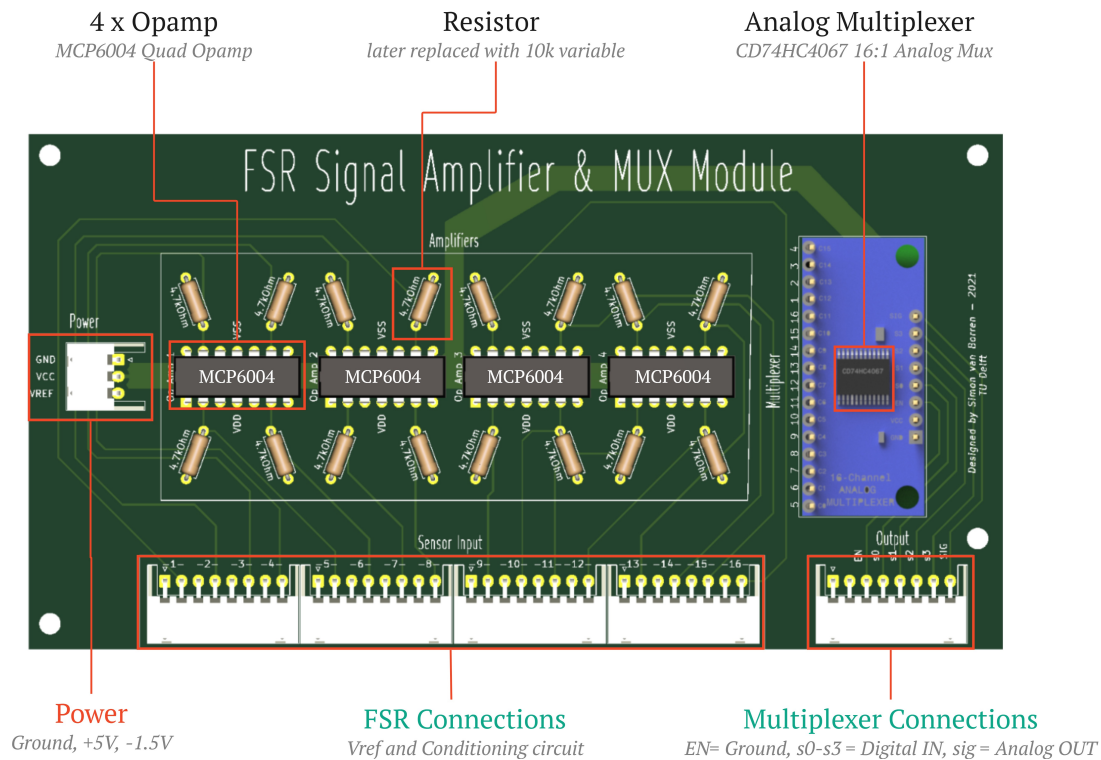


Figure 4.6: A model of the final design for the signal conditioning module printed circuit board (PCB). The module has a total of 4 MCP6004 quad-opamps, amounting to a total of 16 operational amplifiers (opamps). This allows for connection of up to 16 force sensitive resistors (FSRs). The board also includes a 16:1 multiplexer (CD74HC4067). The multiplexer is mounted with its breakout board using through hole pins. The dimensions of the board are $145 \times 77 \times 8\text{mm}$.

4.2.4 PCB Design

Introduction

In order to minimize the effect of noise and other external error sources it was decided to integrate the components discussed in the previous section on custom designed circuit boards. Two different circuit boards were designed: a processing module and a voltage regulator / data-transfer module. The two-layer circuitboards were designed using PCB design software KiCAD and were manufactured by Eurocircuits GmbH.

Signal Conditioning Module

The signal conditioning module was designed for four MCP6004 quad-opamps, which allowed for connection of up to 16 FSRs, all integrated in a circuit as depicted in Figure 4.4. Each module also allowed for mounting of a CD74HC4067 16:1 multiplexer breakout board. A track width of 10 mils (0.25mm) was chosen for the signal carrying connections. Power was supplied to the opamps and the multiplexer using a polygon pour, to account for larger currents, and the reference voltage was routed with a track width of 20 mils (0.50mm). A copper pour was added to the bottom layer to function as ground. All track widths were based on design rules and recommendations provided by Eurocircuits [22]. A detailed layout of the routing of the tracks can be found in Appendix B.3. The circuit board was designed for fixed resistors, which were initially chosen to be $4.7\text{k}\Omega$, but were later replaced by $10\text{k}\Omega$ variable resistors. External connection was achieved using JST-XH connectors (4 x 90deg-8pin and 1 x 90deg-3pin) [38]. The entire design of the PCB is given in Figure 4.6. A fully assembled version of the PCB, with all components soldered into place is given in Figure 4.8a.

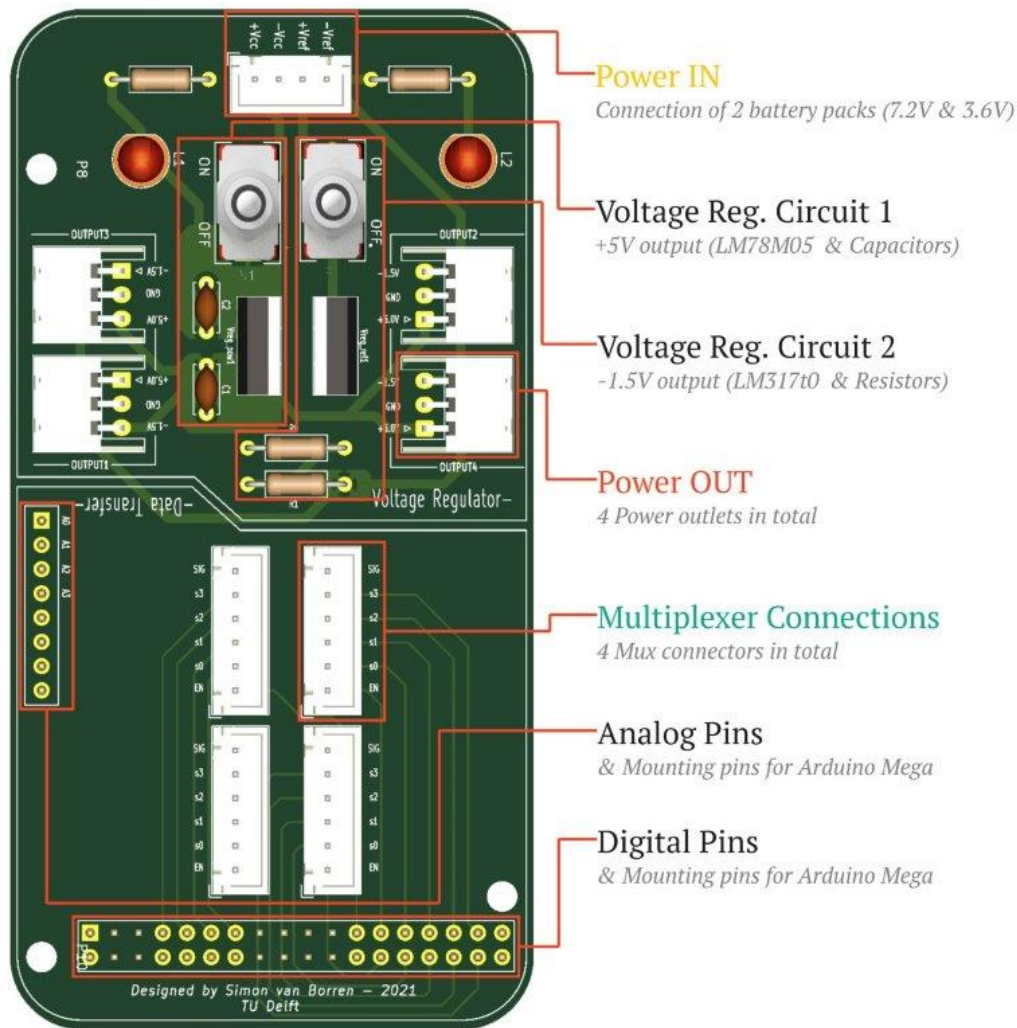


Figure 4.7: A model of the final design for the voltage regulator & data-transfer module printed circuit board (PCB). The module is separated into two parts where the upper part serves as a voltage regulator and the lower part as the data-transfer hub. The module is mounted directly on top of the Arduino and is connected to a dual power supply. A signal conditioning module is connected with the multiplexer (MUX) connection and with the power output. The dimensions of the board mounted on the microcontroller (up to the top of the toggle switch) are $107 \times 55 \times 39\text{mm}$.

Voltage Regulator & Data-Transfer Module

Another module was designed that had the dual function of a voltage regulator on the one hand and facilitating the connection between the signal conditioning module and the Arduino. The module was designed to be mounted directly on the Arduino and allowed for connection of up to four signal conditioning modules using. Each module could be connected with two JST-XH connectors, amounting to 8 connectors for connecting signal conditioning modules ($4 \times 6\text{pin}$ and $4 \times 90\text{deg-}3\text{pin}$) and 1 connector for connection of the power supplies ($1 \times 4\text{pin}$). The track widths were chosen following the same rules as for the conditioning module. The module was designed with two mechanical switches (including two indicator LEDs) for turning the power supplies on and off. The design of the PCB is given in Figure 4.7 and a picture of the fully assembled PCB mounted on the Arduino Mega is given in Figure 4.8b.

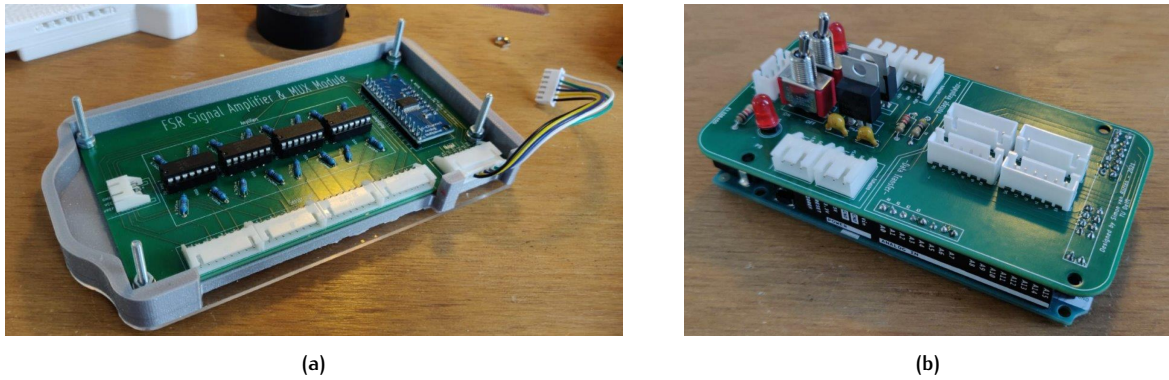


Figure 4.8: Figure showing a (a) fully assembled signal conditioning module in a 3D-printed test-housing and (b) a fully assembled voltage regulator & data-transfer module mounted on an Arduino Mega board. The circuit boards were designed for through hole soldering of the components. The routing of the circuit boards can be found in Appendix B.3 and B.2.

4.2.5 Integration and Connection

As mentioned before, voltage regulator and data-transfer module allows for connection of up to four signal conditioning modules. For protection of the electronics and more convenient use, a housing had to be designed where all components were integrated together. A belt-like housing was designed for this purpose with three interconnected links. The central link contained the two battery packs, the arduino and the mounted circuit board. The two other links contained two signal conditioning modules each, allowing for connection of up to 64 FSRs. The belt-like housing of the system allows the user to attach it around their waist, thus allowing for semi-remote system operation. Data from the FSRs is then transferred from the Arduino to a PC using a 5m long USB-B to USB-A cable. An overview of the entire system is given in Figure 4.10. The housing was 3D printed with an FDM printer using PLA. A picture of the assembled prototype is given in Figure 4.9. The entire system (including the two battery packs) has a mass of approximately 1800g. Its dimensions are given in Figure 4.10.

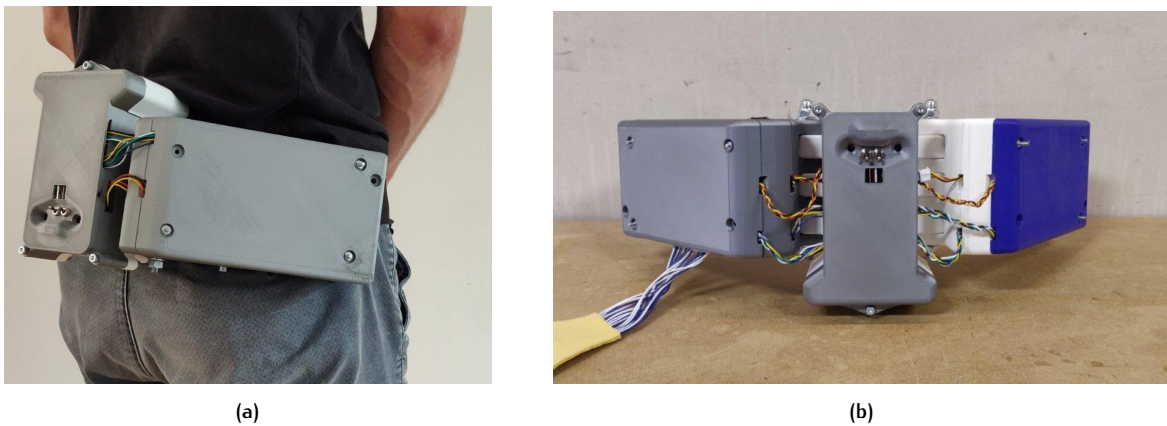


Figure 4.9: Figure showing a (a) picture of the fully assembled prototype worn around the waist and (b) a frontal view of the fully assembled prototype connected to a first version of the sensor pad (see Figure 4.14d).

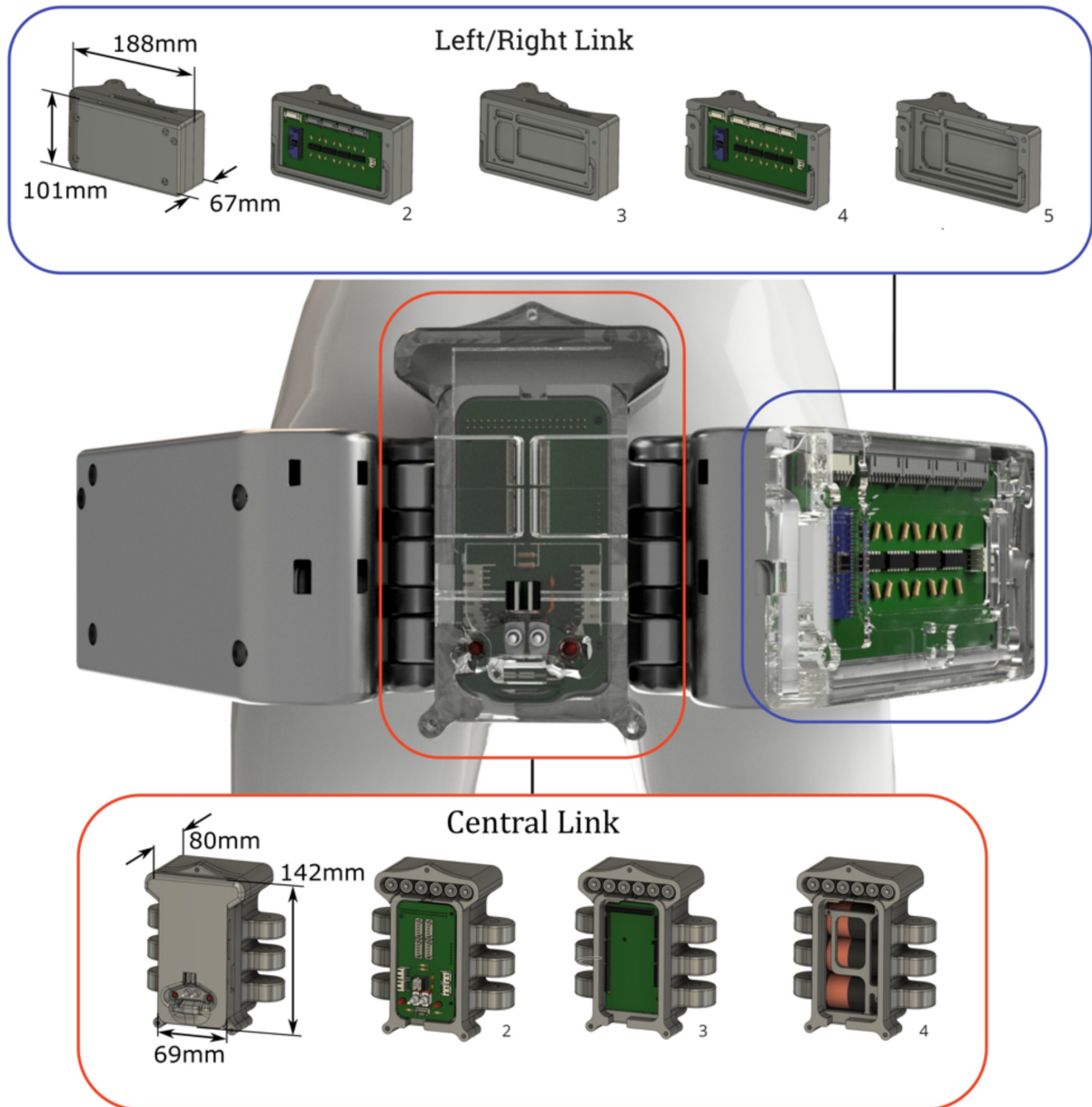


Figure 4.10: Figure showing a rendered model of the entire electronic hardware of the prototype including its dimensions and how it is assembled.

4.3 SENSOR PAD DESIGN

4.3.1 Design Process

Similar to the design process for the electronic hardware, the sensor pad was designed through an iterative design process. Preliminary testing uncovered several characteristics of the FSRs that had to be dealt with by integrating the sensors in a surrounding structure for more consistent and reliable actuation. Several different integration concepts were tested before arriving at the final integration design. The integrated sensors were then combined to form an array, fitting the pressure pad location that was to be measured. Figure 4.11 illustrates this design process as a flowchart. The system requirements for the spatial resolution had to be considered for achieving the required spatial resolution.

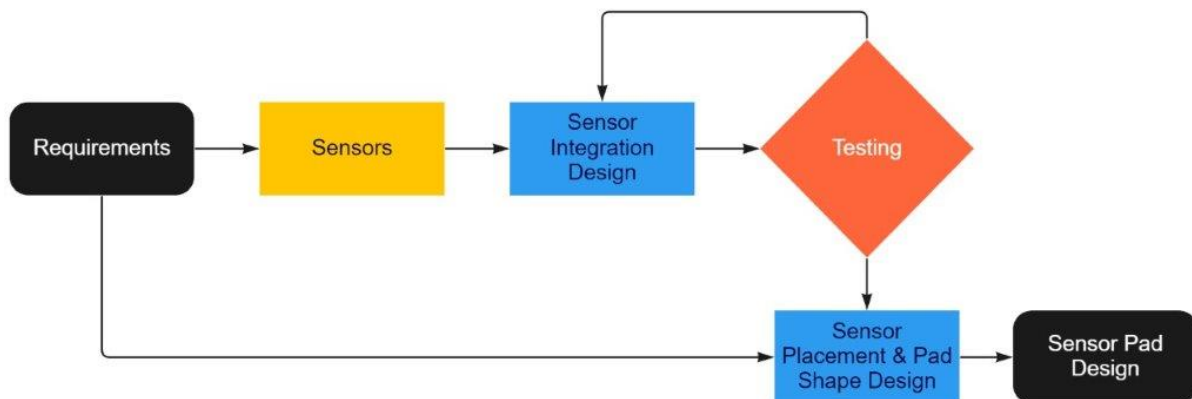


Figure 4.11: Flowchart illustrating the design process for the sensor integration and the sensor pad. Different sensor integration designs were tested during preliminary testing and design iteration 1,2 and 3. The final integration design was then used for the design of the sensor pad.

4.3.2 Sensor Integration Design

Preliminary Testing

In order to understand the behavior of the FSR, one has to be aware of its structure and the mechanisms that cause an applied force to be translated to a decrease in resistance. The FSR402 is a type of shunt mode piezoresistive pressure sensor. Thru mode and shunt mode piezoresistors both rely on the same basic principle where two terminals are separated by a piezoresistive material, which increases in conductivity when pressure is applied [37, 80]. In shunt mode piezoresistors, like the FSR402, the terminals are arranged as two sets of electrically separated interdigitated fingers, glued onto a flexible substrate. This layer is separated by a spacer from another layer with a piezoresistive ink. When a force is applied, the two terminals are moved towards the piezoresistive layer, which causes an electrical connection of the terminals with a resistance depending on the force magnitude that is applied [37]. This also implies that the conductivity depends on the actuation area as a larger actuation area is expected to result in higher conductivity. Strictly speaking, the force sensing resistor therefore senses pressure rather than force. This has significant implications for the actuation of the sensor, which was also experienced during preliminary testing with the setup illustrated in Figure 4.12.

Testing showed a significantly different output signal when the mass was placed with a small offset with respect to the center. This meant that in order to obtain a consistent output required for calibration, the FSRs required integration in some surrounding structure which would ensure consistent actuation. This also required a more reliable actuation system, which is discussed in more detail in Chapter 6. It should be noted that another actuation system was tested before this, which can be found in Appendix A.2. Factors that were found to affect the output were the size of the actuation tip and

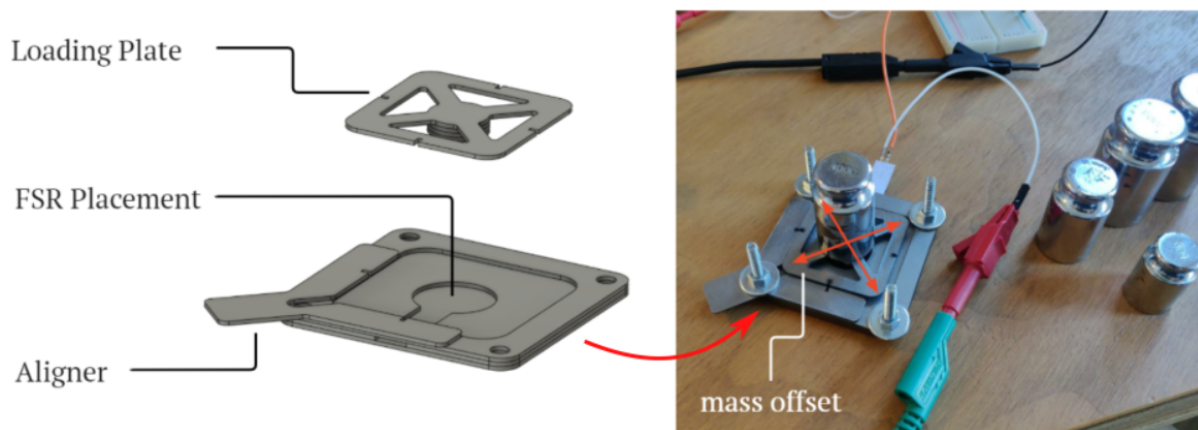


Figure 4.12: Figure illustrating the preliminary test set up that was lasercut from a sheet of 1.5mm steel including a **(Left)** loading plate, room for placement of the force sensitive resistor (FSR) and an aligner for aligning the loading plate. **(Right)** The offset of the mass with respect to the middle was found to have a significant effect on the output of the sensor.

the material placed between the tip and the sensor. Placing a softer material between the tip and the FSR was found to distribute the pressure more evenly over the sensing area, making it less sensitive to slight differences in actuation. Due to its excellent molding capabilities, a two component silicone material was chosen for this purpose, Soft Flex 00-35 [73]. Silicone rubbers are also recommended in an FSR integration guide provided by force sensor manufacturer Sensitronics [72]. The silicone material has a 1:1 mixing ratio and can easily be used in combination with 3D printed molds. It was found that increasing the silicon layer thickness also caused a decreased sensitivity of the sensor and significantly more hysteresis, which is to be expected as elastomers tend to show hysteresis when loaded [94].

Another factor that was found to affect the output of the FSR was the actuation tip diameter. Using a larger area was also found to result in lower sensitivity, potentially caused by the edges of the sensing area preventing adequate deflection of the terminals.

Design Iteration 1

Having found that the silicone rubber has excellent molding capabilities, while also distributing the applied pressure over the sensing area, the first integration design concept was aimed at investigating the possibility of molding the silicone in combination with the sensors to form an array of integrated FSRs. The first concept that was tested was therefore that of a silicone sheet with the FSRs molded into it. This was achieved by designing and 3D printing a mold, with holes to fit the FSRs (see Figure 4.13a). The silicone was then poured over the sensors while the tails and cables were kept vertical. This resulted in an array of 16 integrated FSRs as depicted in Figure 4.13b. The sheet was designed to be thicker at the locations of the sensing areas to ensure pressure would be concentrated onto the sensing areas.

While this first prototype looked very promising, it was found to have some issues that had to be addressed. First of all, inconsistent layer thicknesses ($\pm 1mm$) and air bubbles made the sheet vulnerable to tearing. The sheet at the location of the sensing areas were required to have a minimum thickness of 5mm for ensuring the FSRs were kept into place, which caused significant hysteresis and a decrease in sensitivity. The tails of the sensors also created an uneven back surface, which is undesirable for any FSR integration application [37, 72]. The concept was therefore found to be unfeasible due to limited manufacturing capabilities. However, further research may revisit this concept using a high pressure chamber, a closed mold and potentially FSRs with shorter tails to manufacture a silicone sensor pad as the one tested here. It should however be noted that this would potentially also require strengthening of the silicone sheet as well as a rigid top and bottom plate for reliable actuation to be achieved.

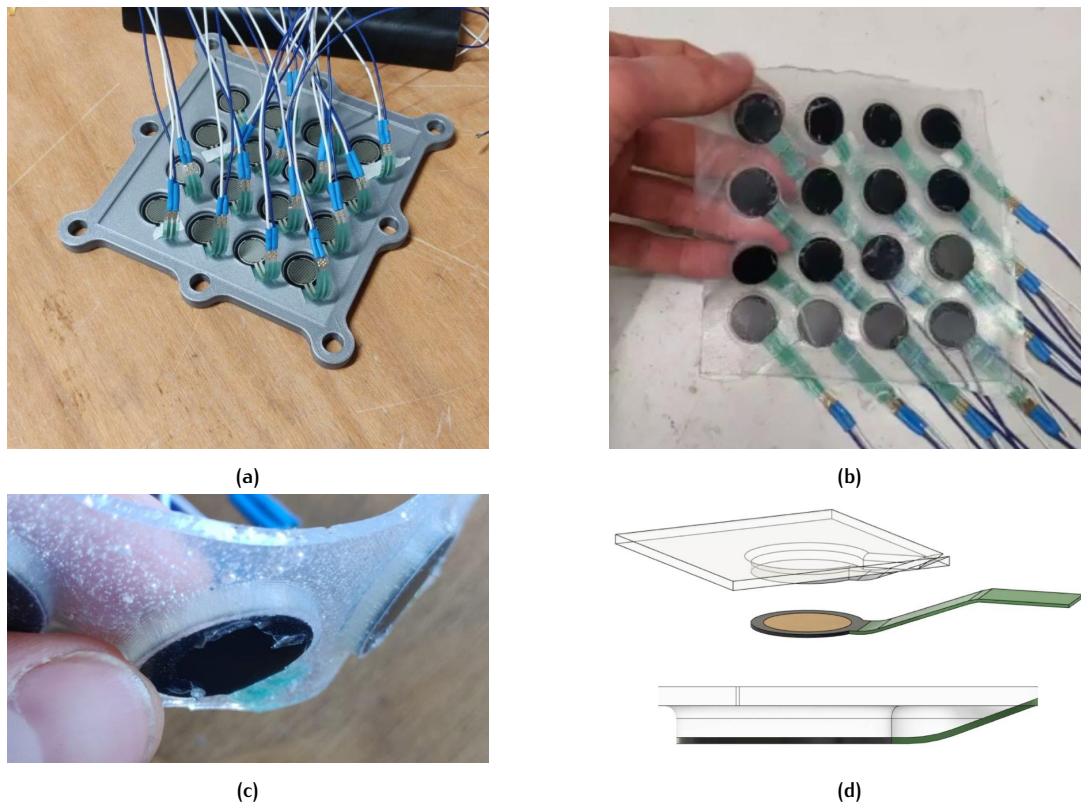


Figure 4.13: Manufacturing of the silicone sensor pad that was tested during the first design iteration. (a) FSRs are first placed in the 3D printed mold over which the silicone is poured to form a sensor pad as depicted in (b). (c) and (d) show how a single sensor is integrated within the silicone. The top silicone sheet layer connecting the sensors to form an array was designed to have a layer thickness of 1.5mm with the buttons covering the sensing area of the FSRs having a thickness of 3.5mm .

Design Iteration 2

The second design iteration focused on individual sensor integration, which could be used to construct an array by combining several integrated sensors together. The concept that was tested during this iteration consisted of a rigid 3D printed bottom plate with room for the FSR to be placed in. This was covered by a thin layer of silicone and an actuation puck with four legs for linear guidance of the puck (see Figure 4.14b). The bottom plate also left room for the tails of the adjacent sensor to be integrated, thus avoiding an uneven back surface to be created. All prints were done using an FDM 3D printer (Crealty Ender 3 pro) with PLA using a standard layer thickness of 0.2mm . A silicone layer thickness of 1mm was found to be sufficient for facilitating the distribution of pressure over the sensing area, while also minimizing the hysteresis and decrease in sensitivity. The layer thickness could better be controlled than in the first design iteration as only a very small mold was required.

Different actuation puck diameters were then tested of $[0.5d_{sens}, d_{sens}]^2$ ($0.5, 0.6, 0.7$ etc.). It was found that a puck diameter of d_{sens} caused a significant reduction in sensitivity. On the other hand, a puck diameter of $< 0.6d_{sens}$ caused a significant increase in sensitivity, but also resulted in inconsistent output when loaded with the set up visualized in Figure 4.12. These findings were found to be in line with the recommendations given in the Sensitronics FSR Integration Guide, where an actuation puck diameter of $0.8d_{sens}$ is recommended [72].

This concept was then tested in a brace for evaluating the sensitivity of the sensors (see Figure 4.14e). A total of 12 of these integrated FSRs were combined in a sensor pad as given in Figure 4.14d. The sensor pad was made by combining the sensors between two layers of synthetic chamois leather. This

² $d_{sens} = 12.7\text{mm}$, the sensing area of the FSR.

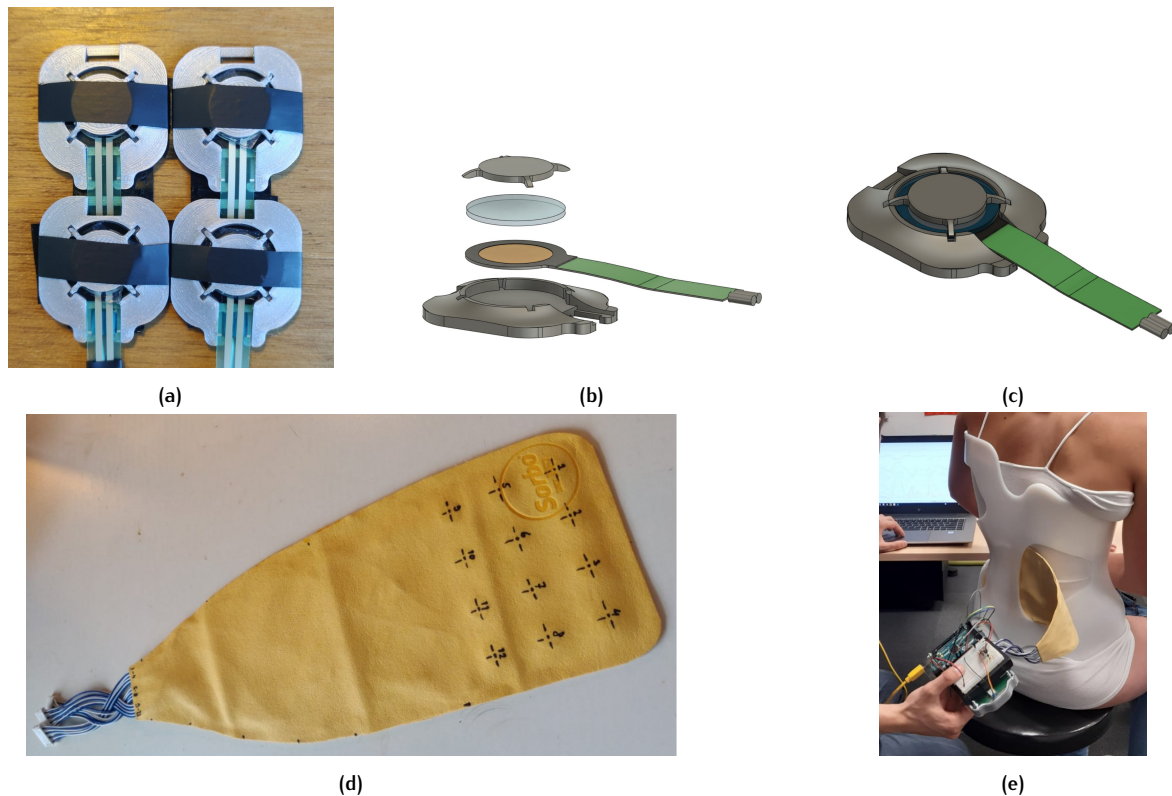


Figure 4.14: Figures showing the concept that was tested in the second design iteration. A total of 12 force sensing resistors were integrated as shown in (b) and (c) and combined as shown in (a) in a sensor pad as given in (d). The pad was placed at the lumbar pad during this first test as shown in (e).

material was chosen as it would provide a soft, yet strong surface that would not cause any discomfort to the patient. Testing was done using a signal conditioning module and an equivalent to the voltage regulator circuit³ as discussed in Section 4.2.4.

This first test showed that the integrated sensors were not sufficiently sensitive as the output signal would only reach a maximum of half of its full range (approximately 2.5V with a full range of 0 – 5V) when the test subject would be instructed to inhale fully. Additionally, it was noted by the orthotist that the thickness of the entire sensor pad was too high and was expected to interfere too significantly with the measurements. It was therefore concluded that the thickness of the entire pad should not exceed a maximum of 5mm, with the sensor pad given in Figure 4.14d being close to 8mm. Additionally, measures had to be taken to increase the sensitivity of the sensors.

Design Iteration 3

For this third and final design iteration the concept discussed in the previous section had to be reduced in thickness, while also ensuring the integrated sensors were increased in sensitivity. The design was therefore simplified significantly to allow for a thinner structure to be 3D printed. This final integration design for the FSRs consists of two 3D-printed plates, that were printed using an FDM printer with PLA with an adjusted layer thickness of 0.1mm (see Figure 4.15a). Both plates have a nominal thickness of 0.5mm, with the upper plate also having bumpers with a thickness of 1.35mm and an actuation puck of 0.8mm.

³ The voltage regulator circuit PCB and the housing was not yet fully assembled at this point.

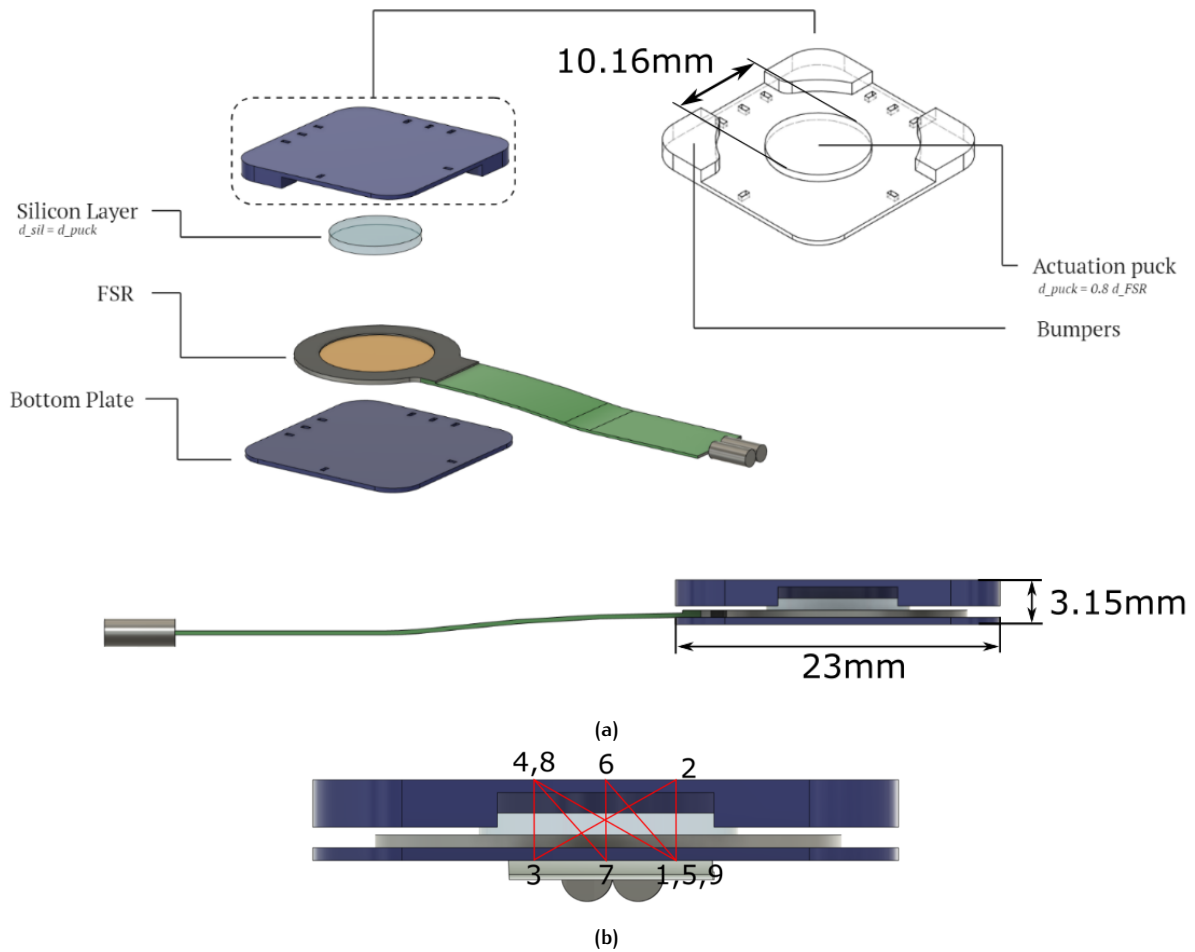


Figure 4.15: Figure illustrating the design of the concept that was tested in the third design iteration. (a) The integration design of the FSR including a bottom plate, top plate and molded silicon layer where $d_{sil} = d_{puck} = 0.8d_{FSR} = 10.16\text{mm}$. The entire integration design has a height of 3.15mm with the surface of the top plates being 514.3mm^2 . (b) The threading pattern for the bottom and top plate connection. Note that this pattern was not always entirely possible due to 3D printing errors.

The design was inspired by a similar integration design used in a study by Ghonasgi et al. (2021) that focused on the design of a device for measuring pressure in the upper arm [28]. The integration design used a larger top surface area that concentrated the load onto the sensing area of the FSR, thus increasing its sensitivity. This was found to be optimal for this application and was therefore adopted in this integration design. The FSR is mounted on the bottom plate using the adhesive tape on the back of the sensor. Centering is done using the holes on the bottom plate. These holes were also used for connection of the upper and lower plate using 0.2mm nylon chord as depicted in Figure 4.15b.

The final integration design had a nominal thickness of 3.15mm (see Figure 4.15a), which resulted in a real thickness of $3.3 \pm 0.2\text{mm}$ (see Figure 4.16). Using two layers of the synthetic chamois leather with a thickness of 0.8mm as was tested in the second design iteration resulted in a total thickness of $4.9 \pm 0.2\text{mm}$. The sensor placement and arrangement of the array for the final sensor pad design will be discussed in the next section.

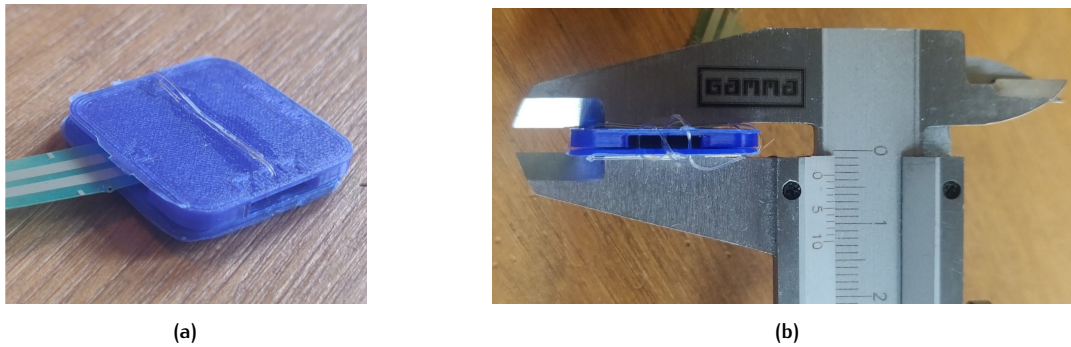


Figure 4.16: (a) Picture of the fully assembled final sensor integration design (b) having a thickness of 3.4mm.

4.3.3 Sensor Placement and Pad Shape

The final sensor pad design was obtained by arranging 15 integrated sensors as discussed in the previous section to fit the area of the pressure pad that was to be measured. The lumbar pad was chosen as the orthotist reported that this pad is often placed in the same relative location in the brace with respect to the torso and would therefore be more easily located on a 3D CAD scan. This was expected to ease the process of mapping, which will be discussed in more detail in the next chapter. The lumbar pad area covered a total of 16439.04mm^2 of which a total of 7759.1mm^2 ($\sim 47\%$) was covered by the integrated sensor area⁴. Assuming that 100% of the pressure is transferred through the integrated sensor area an equivalent lumbar pad area can be defined of $A'_{lb} = 7759.1\text{mm}^2$, which amounts to a spatial resolution⁵ of 0.19cm^{-2} . It should be noted that this is a simplification as the load is expected to be transferred over a larger area. This research will use this value as a valid approximation, but further research will be required for validation.

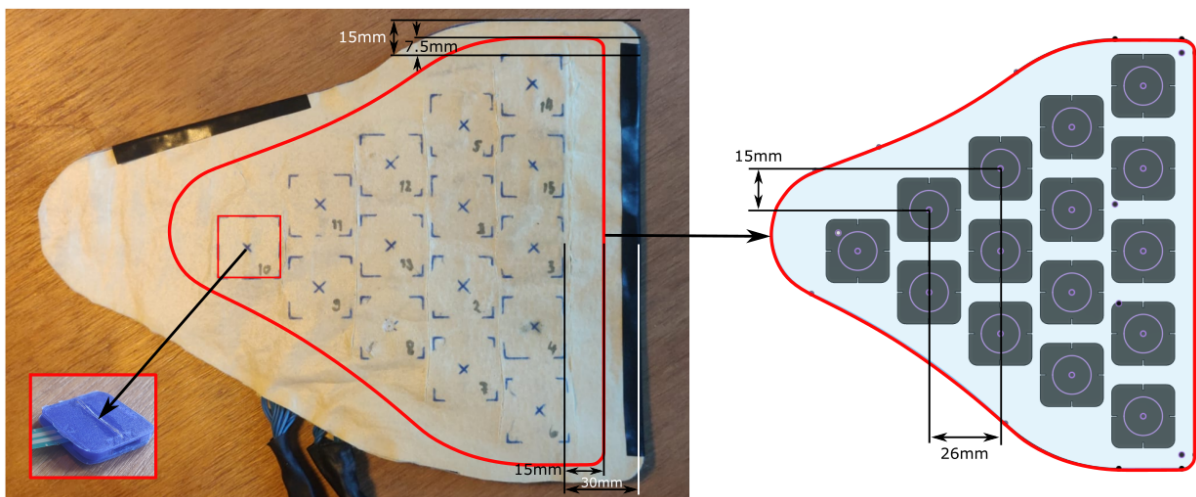


Figure 4.17: Figure illustrating the final sensor pad with a total of 15 integrated sensors. The pad could be correctly placed at the location of the lumbar pad by aligning the upper and right edge of the sensor pad at a distance of 7.5mm ($\sim 8\text{mm}$) and 15mm from the lumbar pad edges.

The triangle array was arranged in such a way that the geometric center of the array would coincide with the geometric center of the lumbar pad shape with the column of 5 vertically placed FSRs arranged in line parallel to the straight side of the pad. Placing the sensors as such would ensure that

⁴ $15 \times 517.3\text{mm}^2 = 7759.1\text{mm}^2$

⁵ $15\text{sensors}/77.56\text{cm}^2 = 0.19\text{cm}^{-2}$

the measured COP would approximate the COP of the entire lumbar pad. The final sensor pad design as depicted in Figure 4.17 did cover a larger area as more room was required for integration of all the cables and to leave some room for gluing the top and bottom chamois leather layers together. The upper horizontal edge of the pad and the vertical edge on the right were used as reference to locate the real pressure pad shape (see Figure 4.17).

5

SPATIAL RECONSTRUCTION METHODS

5.1 INTRODUCTION

As discussed in Chapter 2, relating the measured pressure distribution to a change in brace function requires mapping of the relative two dimensional sensor locations to their associated three dimensional global locations in the brace as well as a reconstruction of the spinal geometry. The latter is necessary to quantify the equivalent bending moments, which are used to infer the function of the brace. In recent years, advancements in imaging techniques have made it possible to reconstruct the spinal geometry based on images obtained with small radiation dosages. However, these systems are still very costly compared to conventional equipment and may therefore not always be available [53]. A method was therefore developed that sought to explore the possibility of mapping the two dimensional sensor pad geometry as well as reconstructing the spinal geometry in three dimensions based on a standard AP¹-radiograph and a surface model of the torso only. A visual coding language called Grasshopper was used to construct two generative design algorithms to reconstruct the sensor pad and spinal geometry in three dimensions within a 3D CAD design application called Rhinoceros 3D. Specific landmarks in the radiograph and standard vertebra proportions were used to construct low resolution three dimensional models of the vertebrae alongside an estimate of the associated global coordinates of the centroids of the vertebral bodies and the intervertebral discs (IVDs). The sensor pad was reconstructed using its dimensions and the associated two dimensional relative sensor locations. The radiograph and surface model that were used belonged to the patient included for validation. The resulting data will be used in Chapter 7 for computation of the equivalent bending moments. This chapter discusses the basic principles of the developed algorithms and the assumptions they are based on.

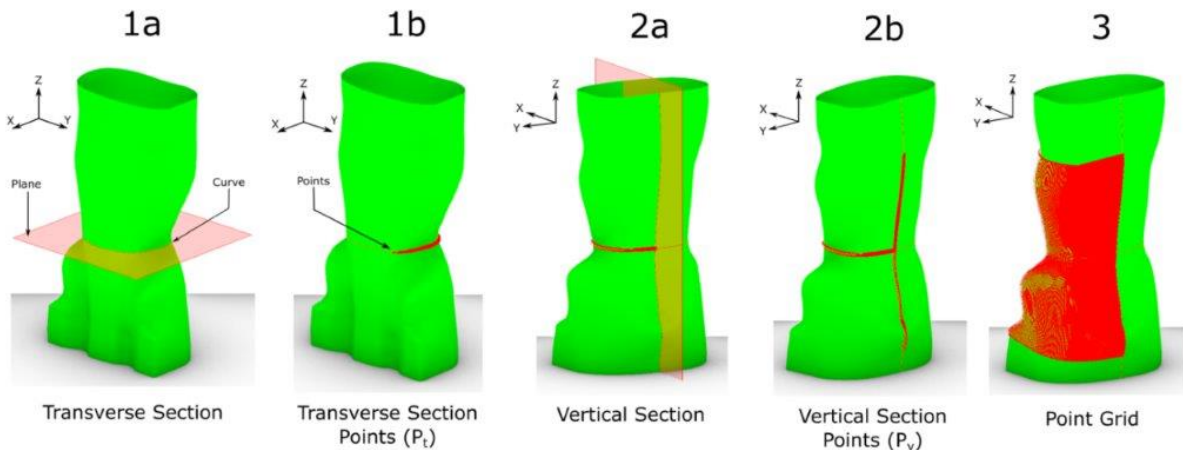


Figure 5.1: Figure illustrating the process for construction of the point grid using Grasshopper for redefining the geometry of the sensor pad on. **(1a)** Transverse section curve is found by intersecting the boundary representation (BREP) and the transverse plane **(1b)** A set of n section points are constructed on transverse section curve. **(2a)** Vertical section curve(s) is (are) found by intersecting BREP and vertical plane through $P_t(k)$. **(2b)** A set of $2m+1$ section points are constructed on the vertical section curve. **(3)** Point grid is created by iterating step (2.) for $k \rightarrow n$

¹ Anterior(=front) to Posterior(=back)

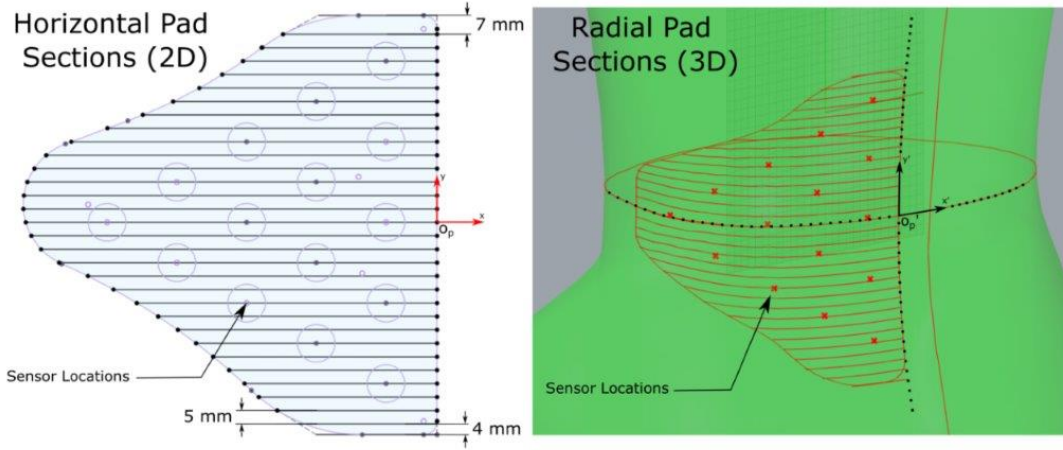


Figure 5.2: Figure illustrating how (Left) the horizontal sections of the sensor pad are used to redefine its geometry on the torso surface by translating the sections to (Right) radial sections with equal relative dimensions using the point grid that is defined on the torso surface (see Figure 5.1) as a reference. The horizontal sections are vertically spaced at a distance of 5mm and at a distance of 4mm and 7mm with respect to the top and bottom edges of the pad respectively. The exact vertical and radial placement of the sensor pad can be defined using the projected pad origin o'_p , which can be defined using the a Grasshopper script provided with two sliders (see Appendix C.2).

5.2 SENSOR PAD MAPPING

Mapping the sensor pad and relative sensor locations to their associated global location in the brace requires an undistorted reconstruction of its original two dimensional geometry onto a three dimensional surface model of the torso. This means that the reconstructed relative dimensions should stay the same. A grid was therefore constructed on a surface model of the torso that was used as a reference to redefine the geometry of the sensor pad on. The surface model represented the inner geometry of the brace, which is assumed to be equivalent to the torso surface when the brace is being worn, and was obtained using photogrammetry. The mesh surface representing the torso was first converted to a *Boundary Representation*, or BREP, which is required for further processing. The point grid is then created as follows:

1. *Construct transverse section points P_t .* This is done by intersecting the BREP with a transverse plane close to the estimated height of the lumbar pad, which also defines the global $XY - plane$ ². A set of n equally spaced points $P_t(k)$ is created on the section curve, with $dX = P_t(k) - P_t(k-1) = 1mm$.
2. *Construct first set of vertical section points P_v .* This is done by intersecting the BREP with a vertical plane defined by a point at the geometric center of the transverse section curve (O), a translation of this point with $Z = 10mm$ (O') and the first point on the subdivided transverse section curve ($P_t(1)$). This curve is then divided into $2m + 1$ equally spaced points with $dY = dX = 1mm$ and where there are m points above and below the transverse section.
3. *Repeat (2.) for every point $P_t(k)$ for $k \rightarrow n$.* This yields a point grid of a total of $2nm + n$ points, which can be used as a reference to define any two dimensional geometry on.

The geometry of the sensor pad can then be defined on the point grid by dividing the two dimensional geometry of the sensor pad in a total of j equally spaced horizontal sections as depicted in Figure 5.2. The sensor locations are defined in the body fixed local $xy - frame$ and all coincide with one of the sections. Assuming that the horizontal sections in 2D translate to radial sections in 3D, the pad geometry as well as the relative sensor locations can be redefined by radial and vertical placement of the projected pad origin o'_p . The grasshopper script is provided with two sliders that can be used

² Note that the surface model was originally placed automatically at the geometric center of its enclosed volume.

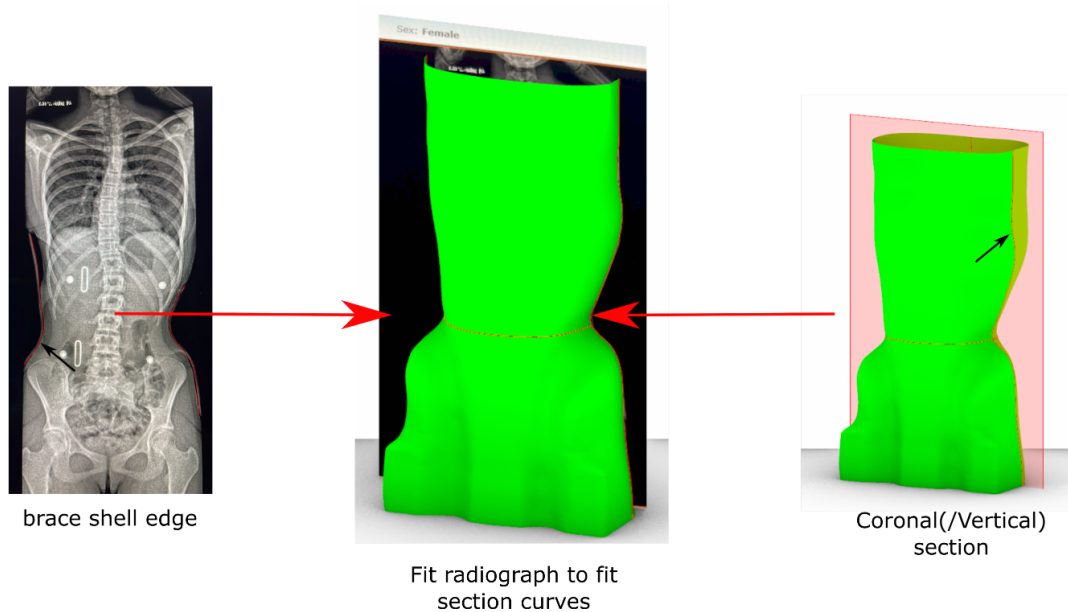


Figure 5.3: Figure illustrating the placement of the radiograph on the YZ-plane with the brace shell edge colinear with its coronal/vertical section curve, which are given in red.. The section curves and planes are obtained using Grasshopper (see Figure 5.1). The radiograph and surface model are of a 15 year old female patient treated with Cheneau-type scoliosis brace which was included for the validation test discussed in Chapter 7.

to change the vertical and radial location of the sensor pad in order to place it at the location of the lumbar pad (see Appendix C.2). When the pad has been placed at the appropriate location, the global coordinates of the sensor locations can be saved as a CSV file to be used in any other application.

5.3 SPINAL RECONSTRUCTION

5.3.1 Introduction

As stated before, the geometry of the spine can be reconstructed using an in-brace AP - radiograph, the BREP model of the inner surface of the brace used in the previous section and standard vertebra and IVD proportions. The developed generative design algorithm was used to reconstruct the lumbar spine in particular, but could in theory be used to reconstruct the entire spine if necessary. This section discusses the steps that are taken in the algorithm to reconstruct the lumbar vertebrae and IVDs.

5.3.2 Vertebra and IVD Data

The standard morphometric proportions that were used to reconstruct the the vertebrae were obtained from an open source database of morphometric measurements provided by the University of Michigan [55], a study by Gilad and Nissan (1985) [59], a study by Azophra-Monge and Aleman Aguilera (2020) [9] and a study by Onishi et al. (2019) [62]. The database was used to find the skin thickness in the lumbar area and the three other studies were used to find vertebra and IVD proportions. The database yielded growth curves with estimates based on a reference population of approximately 6000. An estimate could therefore be obtained based on sex and age and values were obtained for an average 15 year old female. The studies that were used to estimate the vertebra dimensions on the other hand, were based on mostly (male) adults (157m [59], 46m//48f [9] and 150m/150f [62]) as limited to no data was found that corresponded with the provided radiograph and surface model of the 15 year old female patient. However, it was assumed that the dimensions could be used to approximate the required geometry.

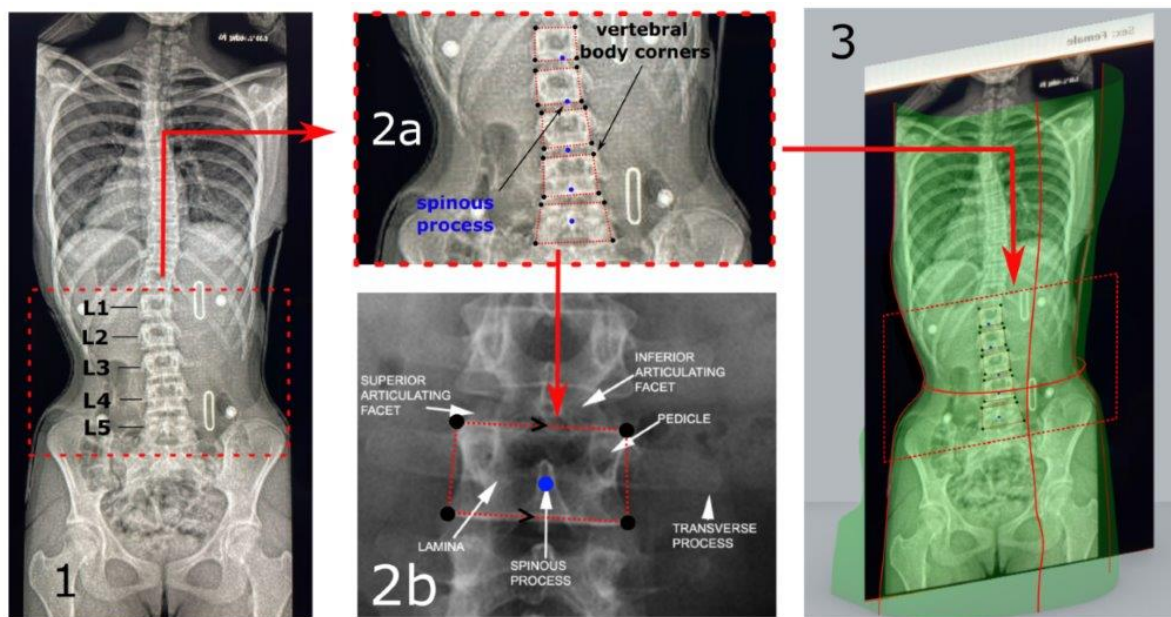


Figure 5.4: Figure illustrating the process of landmark identification of the lumbar vertebrae including the 4 outer corners of the vertebra and the spinous process. **(1,2a)** The spinous processes and the vertebral body corners are identified. **(2b)** Illustration of the trapezoidal shape (for an arbitrary radiograph) that is used to approximate each vertebral body. **(3)** The landmarks are identified as points on the global YZ-plane. Radiographs depicted in 1, 2a and 3 are of a 15 year old female patient that was included for the validation test discussed in Chapter 7. The radiograph in 2b depicts the L3 vertebra and was obtained from [51].

5.3.3 Scan Placement and Landmark Identification

The first step was to load the radiograph into the same file as the surface model and place it on the global $YZ - plane$, with the global coordinate frame being as defined in the previous section. The outer³ edges visible in the radiograph can be assumed to be colinear with the coronal cross section (in the $YZ - plane$) of the surface model, as both are defined by the rigid brace shell. The radiograph can therefore be scaled proportionally in the $YZ - plane$ to fit the coronal section curves as depicted in Figure 5.3.

Then, the anatomical landmarks can be identified on the radiograph. For each of the lumbar vertebrae, points were created on the $YZ - plane$ at the spinous process and the four corners of the vertebral body as depicted in Figure 5.4. The shape of each vertebral body in the radiograph was approximated as a trapezoid, with the lines connecting the upper two and lower two corner being parallel and the lines connecting the upper and lower left and the upper and lower right corners being equal in length (see Figure 5.4).

5.3.4 Reconstruction Algorithm

A generalized parametric model was created based on a figure provided by Gilad and Nissan. The model was simplified as depicted in Figure 5.5(1) and was translated to a three dimensional model. The vertebrae are simplified as a cubic shape connected to a pyramid, representing the spinous process. As the vertebrae are not oriented perfectly with the $ABCD$ -plane parallel to (3) as depicted in Figure 5.5, some distortion can be expected in the image plane of the radiograph (see Figure 5.6). However, the simplifications made to represent the vertebra geometry allowed to extrapolate the five identified

³ More accurately, the inner edge of the brace shell

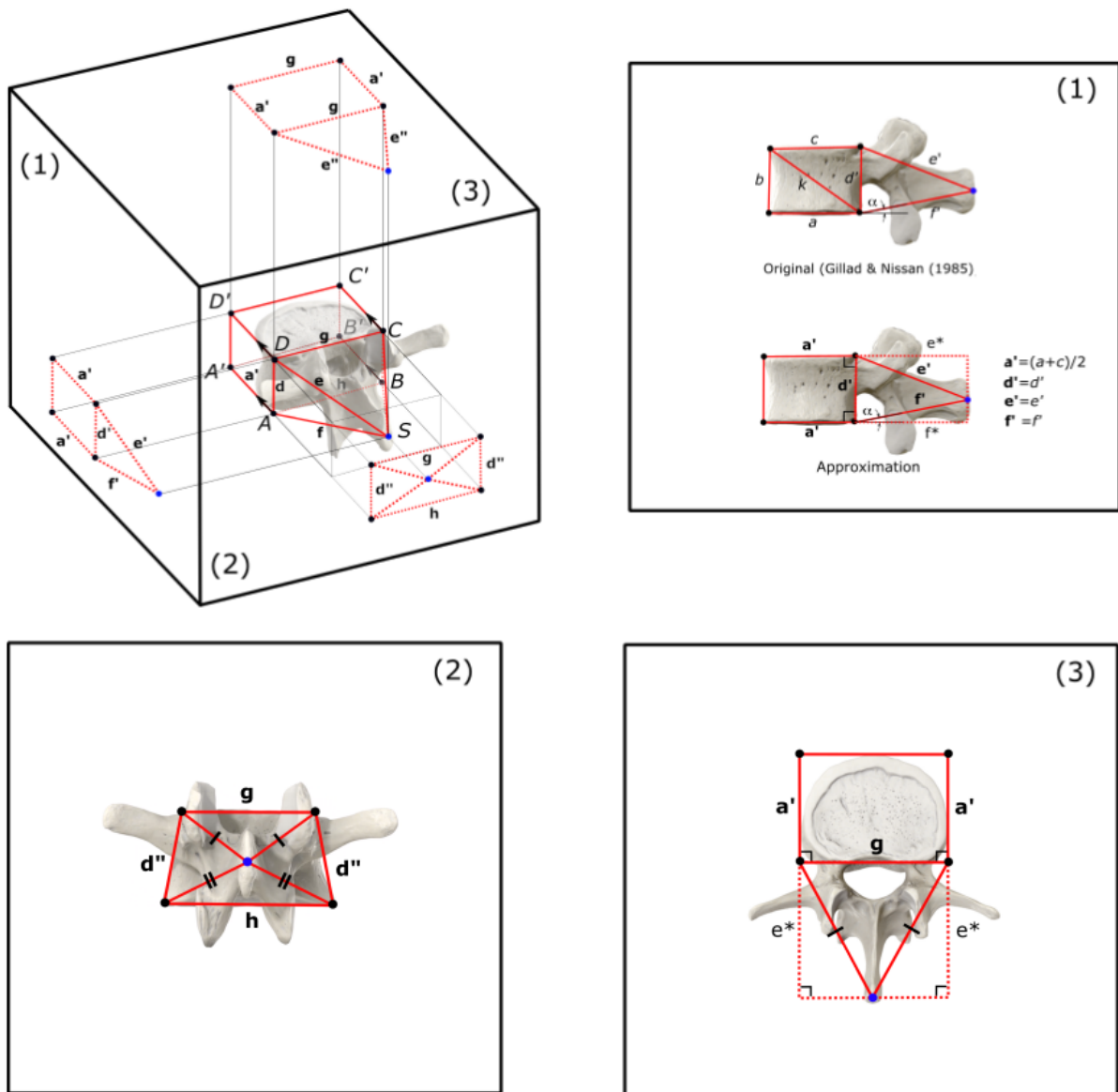


Figure 5.5: Illustration of the wireframe model that was used to approximate the vertebra geometry including projections on a local transverse, sagittal and coronal plane. (1) A simplification of the figure from Gillad and Nissan (1985) [59] is used to approximate the dimensions in a local sagittal plane. The approximation takes a' (representing the vertebral body depth) to be equal on the cranial and caudal side of the vertebral body and perpendicular to the vertebral body height d' . (2) Posterior view of a vertebra with the projected dimensions in a local coronal plane. In the local coronal plane the projection is a perfect isosceles trapezoid with equal sides d'' . (3) Superior view of a vertebra with projected dimensions in a local transverse plane. The dimensions a' and e^* are same as defined in (1) and g is the same as defined in (2). The L₃ vertebra model used for this illustration was obtained from [69].

landmarks to the wireframe representation of the vertebra as depicted in Figure 5.5. The generative design algorithm that was used to reconstruct the vertebrae essentially followed two steps:

1. Construct the spinous process ABCDS - Figure 5.7. This is done by projecting the identified landmarks onto the torso surface model. These projections are created by intersecting a line perpendicular to the coronal section illustrated in Figure 5.3 with the surface model. All projections are then moved inward (positive X - direction) with a distance $D_{skin,Lx}$, which is defined as the distance from the skin surface to the spinous process and was obtained directly from the morphometric measurement database mentioned earlier. Then, as the vertebrae are assumed to be

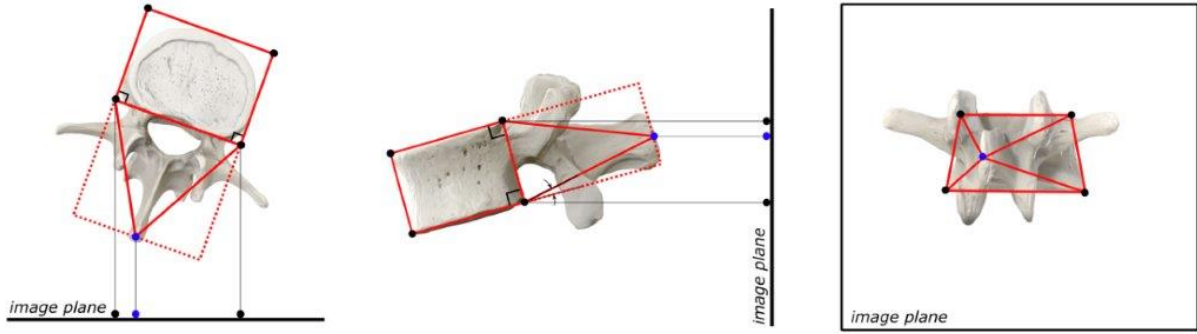


Figure 5.6: Illustration showing how the projected landmarks identified in the radiograph do not perfectly represent the posterior view of the vertebra illustrated in Figure 5.5(2). Assuming symmetry of the vertebra does however still allow for an approximation to be made of its spatial geometry. The L₃ vertebra model used for this illustration was obtained from [69].

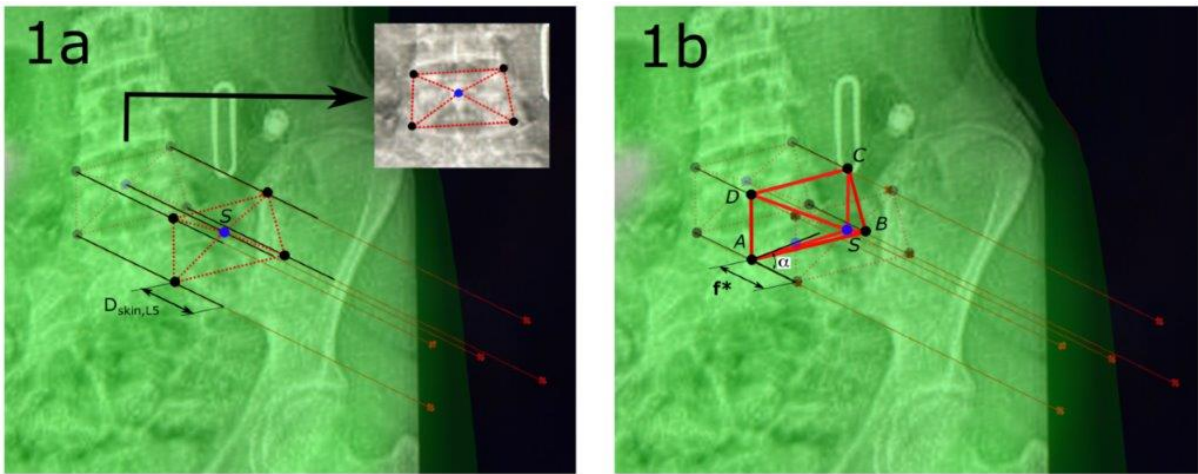


Figure 5.7: Figure showing the process of constructing the spinous process. **(1a)** The projected landmarks are moved inward over a distance $D_{skin,LS}$. **(1b)** spinous process is defined by the distance of S to plane ABD , f^* and the inclination angle α (the angle between planes ABD and ABS .)

symmetrical, the distances of the vertebral body corner to the spinous process point S are constrained assuming $AS = BS = f$ and $DS = CS = e$ with all corner points coinciding with their respective projection line. As the landmark identification will always have some error, no values for e and f can be found that result in the line segments AB and CD being parallel. The surface $ABCD$ is therefore described by two planes, where the plane ABD is chosen as a reference plane for the posterior surface of the vertebral body. Using the dimensions obtained from Gillad and Nissan, the inclination angle α was used to define the angle between the planes ABD and ABS and $f^* = \cos(\alpha)f'$ was used to define the distance between ABD and S .

2. Construct the anterior vertebral body plane $A'B'C'D'$ - Figure 5.8. This is done by translating the posterior vertebral body surface over a distance a' in the normal direction with respect to its reference plane ABD . The normal vector is found by computing $\vec{AB} \times \vec{AD}$. The value for a' also followed from the dimensions defined by Gillad and Nissan (see Figure 5.5(1)).

This process can be repeated for all vertebrae, yielding a simplified wireframe representation for each vertebra.

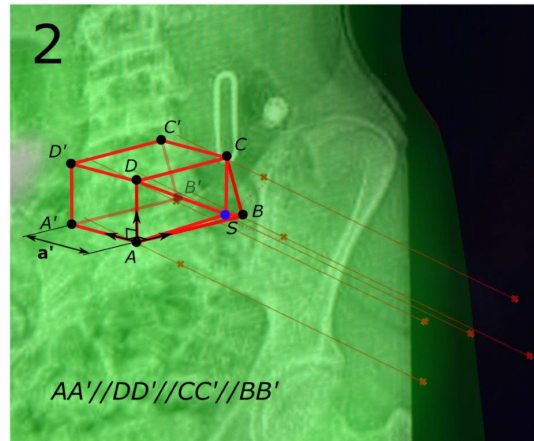


Figure 5.8: Figure showing the reconstruction of the vertebral body by translating the posterior vertebral body surface $ABCD$ over a distance a' in the normal direction w.r.t. the ABD plane. Note that the line segments connecting $ABCD$ and $A'B'C'D'$ are parallel and are equal to the vertebral body depth a' .

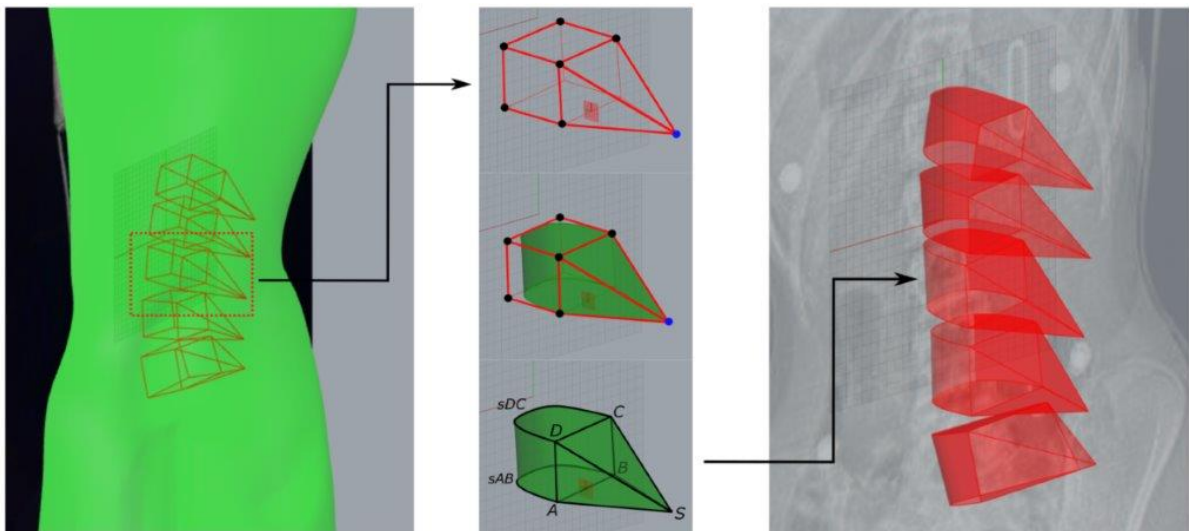


Figure 5.9: Figure showing the final step in reconstructing the vertebrae using Grasshopper. Splines are created on the cranial and caudal vertebral body surfaces (sAB and sDC) to better approximate the vertebral body shape. The centroids of the vertebrae are computed as the centroid of the volume enclosed by AB - sAB and CD - sCD and the spinous process $ABCD$.

5.3.5 Vertebral body and IVD Centroid Computation

In a final step, the centroids of the vertebral bodies and IVDs were computed. This required conversion of the spatial geometry to an enclosed volume for each vertebra. A better approximation of the vertebral body shape was constructed by constructing a spline from C to D (sCD) and from A to B (sAB) on the superior and inferior vertebral body plane respectively, using the line segments DD' , $C'D'$, CC' , AA' , $A'B'$ and BB' as tangents. (see Figure 5.9). The global location of the vertebral body centroid is then found by computing the centroid of the volume enclosed by surface AB - sAB and surface CD - sCD . The intervertebral discs are found by constructing a volume enclosed by neighbouring superior and inferior vertebral body planes. This can be done for all IVDs except for the $L5S1$, which was reconstructed based on the proportions obtained from Onishi et al. (2019) This study defined posterior as well as anterior IVD heights, which could be used to define the angle β between the superior and inferior planes enclosing the volume of $L5S1$ and the posterior disc height relative to the posterior height of the $L45$ IVD ($u = x'_{L5S1} / x'_{L45}$). The $L5S1$ was reconstructed by rotating the inferior

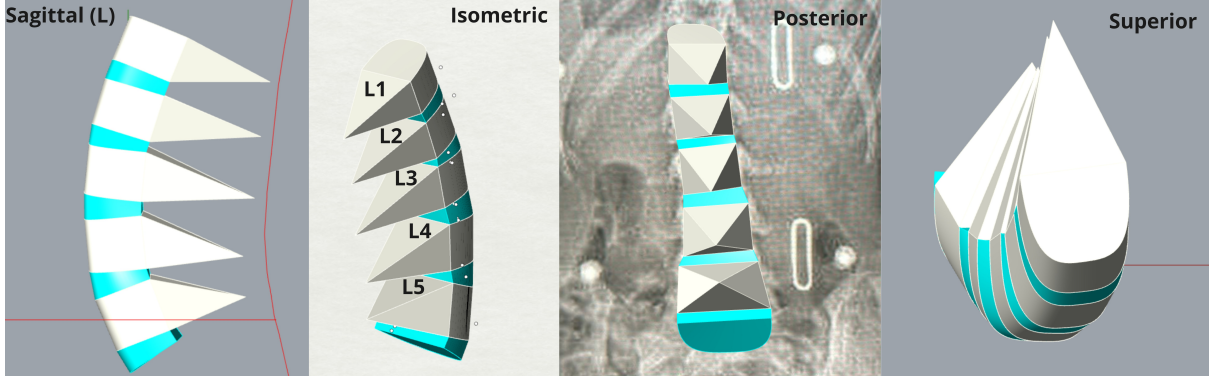


Figure 5.10: Figure illustrating a complete reconstruction of the lumbar spine that was obtained using Grasshopper. A sagittal (left), isometric, posterior and superior view is shown of the L1-5 lumbar vertebrae and the associated inferior intervertebral discs (IVDs).

vertebral body plane with an angle β relative to an axis defined by AB and translating it in the normal direction over a distance $x_{L5S1} = ux_{L45}$. As such the global coordinates were obtained for centroids of all 5 lumbar vertebrae as well as their respective inferior IVDs. The entire reconstruction of the lumbar spine is depicted in Figure 5.10.

5.3.6 Local Vertebra Frame and Rotation Matrix

Using the centroids defined in the previous section as the local origin, a local body fixed V_y -frame can be constructed for each vertebra as well as a rotation matrix describing the orientation of the vertebra with respect to the global M -frame (or vice versa). This can be done as follows:

1. *Construct the local z' -axis.* This axis is assumed to be colinear with the line segment connecting the centroid of the vertebra (${}^M\mathbf{GC}_{Vy}$) and the centroid of its inferior adjacent IVD (${}^M\mathbf{GC}_{Vxy}$):

$${}^M\mathbf{e}_{z'} = {}^M\mathbf{GC}_{Vy} - {}^M\mathbf{GC}_{Vxy} \quad (5.1)$$

2. *Construct the local y' -axis.* This axis is perpendicular to the local $x'z'$ -plane, which is defined by any two points on the local z' -axis and the spinous process of the vertebra (${}^M\mathbf{S}_{Vy}$). The local y' -axis can then be found by taking the cross product of any line parallel to the $x'z'$ -plane with the local z' -axis:

$${}^M\mathbf{e}_{y'} = [{}^M\mathbf{S}_{Vy} - {}^M\mathbf{GC}_{Vy}] \times {}^M\mathbf{e}_{z'} \quad (5.2)$$

3. *Construct the local x' -axis.* This done by computing the cross product of the previously defined local z' -axis and local y' -axis:

$${}^M\mathbf{e}_{x'} = {}^M\mathbf{e}_{y'} \times {}^M\mathbf{e}_{z'} \quad (5.3)$$

4. *Define Rotation Matrix $M \rightarrow V_y$.* This is done by normalizing the previously found vectors and combining them as follows:

$${}^{V_y}\mathbf{C}_M = \begin{pmatrix} {}^M\hat{\mathbf{e}}_x^T \\ {}^M\hat{\mathbf{e}}_y^T \\ {}^M\hat{\mathbf{e}}_z^T \end{pmatrix} \quad (5.4)$$

The resulting data yields a spatial representation of each vertebra. The computation described above is done in MATLAB using a CSV file containing the global coordinates of the wireframe representation defined in 5.2.4 as well as the global coordinates of the centroids defined in 5.2.5.

6

STATIC CALIBRATION OF FORCE SENSITIVE RESISTORS

6.1 INTRODUCTION

As the force sensitive resistors, or FSRs, implemented in the sensorpad produce a digital voltage signal as output, they require calibration in order to translate the measurement to an associated pressure value. The output of the FSR depends on its relation between force and resistance and the conditioning circuit discussed in Chapter 4. This results in a complex non-linear relation which is found to be affected by hysteresis and creep. This chapter discusses a method for calibration of the FSRs based on a generic model with variable parameters.

6.2 METHODS

6.2.1 Test Setup

As discussed in Chapter 4, it was found that the signal output is affected significantly by where on the sensing area the pressure is applied. For this reason, the sensor was integrated in a surrounding structure that is supposed to distribute the pressure more evenly, making it less sensitive to slight differences in actuation. However, a point load may still cause a different output when not applied in the same location on the top plate of the sensor. As calibration is most accurately done by applying point loads of a known magnitude to the sensor, a test setup was required that could be used to apply a load consistently in the same location perpendicular to the top plate of the integrated sensor. Therefore, the apparatus depicted in Figure 6.1 was designed.

The setup consists of a yoke connected to a hook by a chord that is attached on either side as can be seen in Figure 6.1b. The yoke is attached by another chord to a drill-stand. The drillstand allows for vertical linear motion of the yoke by pulling the handle down. The yoke can be moved down until the black rubber knob in the middle makes contact with the top plate of the integrated sensor and is no longer supported by the drill stand (Figure 6.1a). The handle of the drill stand is then secured, which allows the yoke to balance freely on the top plate of the integrated sensor. The hook can then be loaded with additional weight, creating a point load perpendicular to the sensor surface of $F_{load} = (m_{yoke} + m_{hook} + m_{weight})g$. The yoke has a partially 3D printed PLA outer structure and partially lasercut steel inner structure resulting in a mass of 114g in total (see Appendix A.3) and was designed to have its center of gravity to be below the black rubber knob.

6.2.2 Test Procedure

In order to find a relation between the applied load and the output signal, the sensor needs to be loaded and deloaded incrementally, which allows for the hysteresis behavior of the sensor to be modelled. As it is assumed that the interface pressure in the brace will not change with particularly high frequencies, a static calibration procedure was thought to suffice for this application. This procedure is based on defining model parameters obtained through a series of static loading tests. These parameters define a model that describes the sensor response of the FSR. The inverse of this model can then be used to relate a measured voltage value to a value for pressure. Obtaining reliable estimates of these model parameters required a specific test protocol and data processing method of the raw voltage signal.

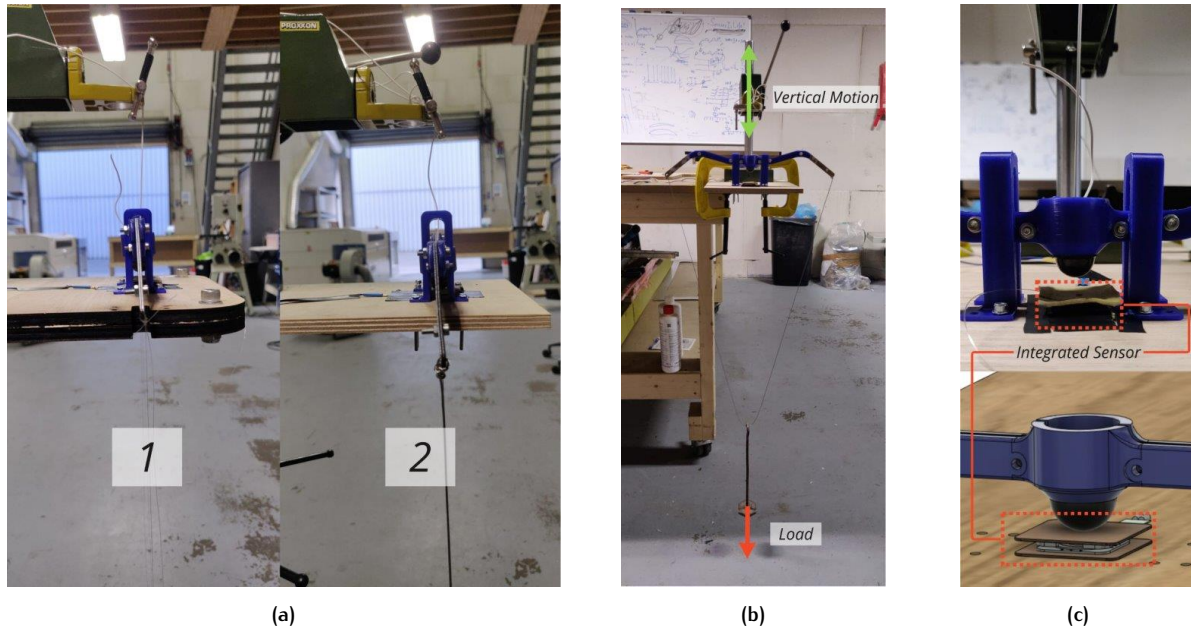


Figure 6.1: Figures showing the test setup that was used for the actuation of the sensors (a) Actuation of the FSR is initialized by moving the handle of the drill stand down. (b) Complete Test Setup including the drill stand, yoke, testplate and the hook.(c) This figure shows an integrated test sensor. Calibration and testing of the FSRs integrated in the sensor pad was done by moving the guide brackets to the edges of the test plate to make room for the larger area of the pad.

Table 6.1: Table showing the loads that are used for loading the sensors . Without additional weight, the mass is equal to that of the yoke and the hook.

	Mass [g]	Load [N]	Pressure [kPa]
0.	0	-	-
1.	161.0 ^a	1.579	3.073
2.	361.0	3.541	6.890
3.	611.0	5.994	11.66
4.	861.0	8.446	16.43
5.	1111	10.90	21.20
6.	1361	13.35	25.98

^a ($m_{yoke} + m_{hook}$)

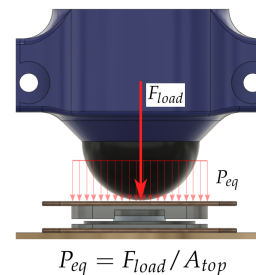


Figure 6.2: A load F_{load} applied on the top plate of the integrated sensor can be translated to an equivalent pressure P_{eq} by dividing over the top plate area $A_{top} = 514mm^2$

FSR Testing Protocol

Based on the requirement for the effective range of the system defined in Chapter 3, a 6 point calibration range was defined as denoted in table 6.1. Data was acquired by performing 7 load-deload cycles for each FSR. Each loading cycle was initiated by pulling down and securing the handle as depicted in Figure 6.1a, which results in a load of 1.58N, equivalent to a pressure of 3.02kPa (1.). The hook is then incrementally loaded (manually) with approximately 10 - 15s¹ time intervals using weights of 200g and 250g up until a load of 13.35N, which is equivalent to a pressure of 25.98kPa (6.) (see Figure 6.2). When the maximum load is reached, the sensor is incrementally deloaded from 6. - 0. , also with 10 - 15s time intervals. During preliminary testing it was found that the sensors required a few loading cycles for the signal output to become consistent. The first 2 of these 7 loading cycles are

¹ the time required for the signal to converge to a constant value

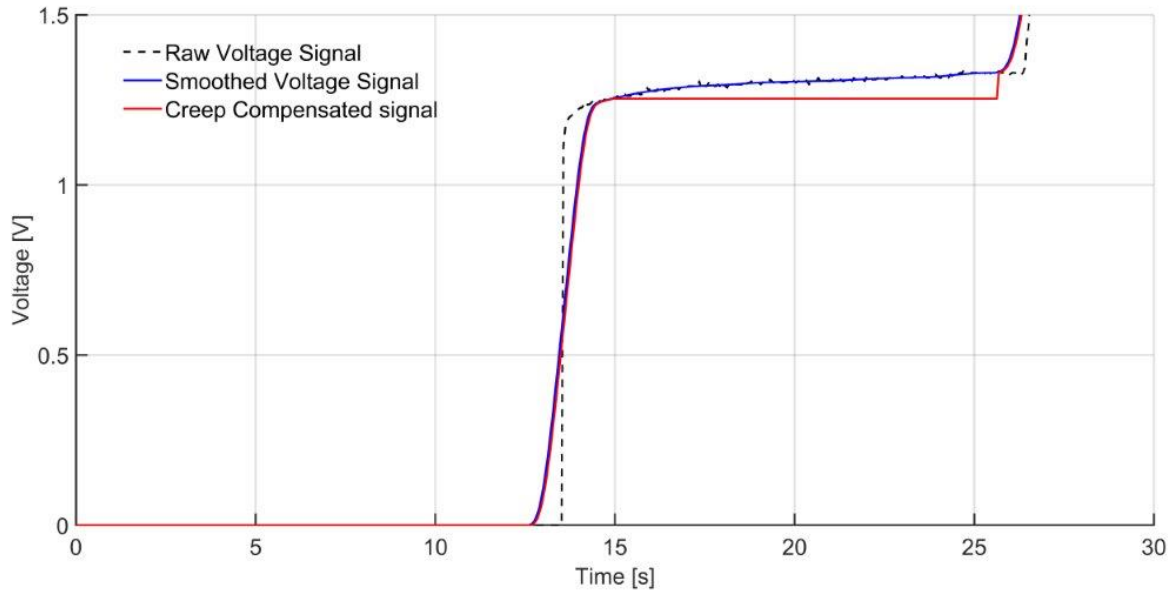


Figure 6.3: Figure showing the raw, smoothed and creep compensated signal response of the force sensitive resistor to a 161g load, which is equivalent to a pressure on the top plate of 3.073kPa (see Table 6.1 and Figure 6.2).

therefore used for excitation of the FSR, while the remaining 5 cycles are used for further processing. All loading cycles performed for a single FSR were done with 2 minute intervals.

Signal Processing

Preliminary tests discussed in Chapter 4 also showed that the raw output signal of the FSR contained noise and was subject to *creep*. The latter causes the FSR to slowly decrease in resistance over time when a load is applied, which results in an increase in output signal. However, this can easily be compensated for by using a method proposed by Florez et al. (2010) [25]. This method assumes that an increase in signal output below a certain value can only be related to creep. This implies that when the derivative of the signal is found to be below a certain value, the signal should hold its previous value (see Algorithm 6.1). It was found that a value of $dV/dt = 0.03V/s$ was optimal for this purpose. In addition to this, a moving average filter was applied to the signal to filter out the noise. A window length of 40 data points was used, which is equivalent to approximately $1.8s^2$. The resulting signal is depicted in Figure 6.3.

Algorithm 6.1: Creep Compensation Function

Input: The (smoothed) voltage signal V with length n and its derivative dV with length n

Output: The creep compensated voltage signal V_{cc} with length n ($V_{cc}(1) = V(1)$)

```

1  $V_{cc}(1) = V(1)$ 
2  $dV(1) = 0$ 
3 for  $k = 2 \rightarrow n$  do
4    $dV(k) = V(k) - V(k-1)$ 
5   if  $0 < |dV(k)| \leq 0.03$  then
6      $V_{cc}(k) = V(k-1);$            % hold previous value
7   else
8      $V_{cc}(k) = V(k);$ 

```

² Assuming a sampling frequency of $\sim 22.2Hz$

6.2.3 Hysteresis Compensation Method

As stated before, the output signal of the FSR is affected by hysteresis. This means that loading the sensor follows a different function than deloading. The output of the sensor therefore depends on its previous state. A conversion model is therefore required that defines a set of functions for load increase and load decrease, based on current and previous values. This set of functions consists of two *major* conversion curves for loading and deloading, with fixed parameters that were obtained with the load/deload tests and a set of equivalent *minor* curves. These minor curves are based on the major curves, but have variable parameters that are estimated based the previous voltage and pressure value. Conversion of the creep compensated voltage signal V_{cc} to a pressure signal p is done using an algorithm that can be described with the pseudocode given in 6.2. Note that both the creep compensation as well as the hysteresis compensation was not required to run in real time.

Algorithm 6.2: V-p Conversion Algorithm

Input: The creep compensated signal V_{cc} and the major loading and deloading functions F_l and F_{dl}

Output: The estimated pressure signal p with length n

```

1  $p(V_{cc}(1)) = F_l(V_{cc}(1))$                                 % First value defined by the major curve
2 for  $k = 2 \rightarrow n$  do
3   if  $V_{cc}(k) \geq V_{cc}(k-1)$  then
4      $f_{l,k} = f(F_l, V_{cc}(k-1), p(k-1))$                 % Minor loading curve
5      $p(V_{cc}(k)) = f_{l,k}(V_{cc}(k));$ 
6   else
7      $f_{dl,k} = f(F_{dl}, V_{cc}(k-1), p(k-1))$           % Minor deloading curve
8      $p(V_{cc}(k)) = f_{dl,k}(V_{cc}(k));$ 

```

Calibration of the FSRs was done by obtaining the parameters necessary to define F_l and F_{dl} , which are used in the conversion model to convert a voltage value to a pressure value. (A more detailed calibration protocol is given in Appendix D.)

6.2.4 Measurement Uncertainty

When estimating the uncertainty in the calculated pressure, one has to take into account the random error in the voltage signal and the systematic modelling error when converting the voltage to a pressure value. Both error contributions were estimated based on the 5 (effective) loading tests done for each sensor. Assuming that these errors are independent of the sensor number and therefore similar for all sensors, an estimation can be made of the random and systematic error, based on the measurements done with the 15 FSRs integrated in the sensor pad. The former can be obtained by taking the root mean square of the standard deviations for every discrete voltage value that followed from the loading tests. As such, the (relative) random errors $\delta V_{cc,l}$ (error for load increase) and $\delta V_{cc,dl}$ (error for load decrease) can be estimated for loading and deloading, resulting in a propagated error δp_l and δp_{dl} . The propagated random error for loading as well as deloading based on the load/deload tests can then be obtained as follows:

$$\delta p_l(V_{cc}) = \delta V_{cc,l} \frac{dF_l(V_{cc})}{dV_{cc}} \quad (6.1)$$

$$\delta p_{dl}(V_{cc}) = \delta V_{cc,dl} \frac{dF_{dl}(V_{cc})}{dV_{cc}} \quad (6.2)$$

Assuming that the random error is independent of the load direction (increase or decrease), the propagated random error for any voltage value V_{cc} is obtained as follows:

$$\delta p(V_{cc}) = \sqrt{\frac{\delta p_l^2(V_{cc}) + \delta p_{dl}^2(V_{cc})}{2}} \quad (6.3)$$

The modelling error on the other hand is the result of a systematic difference between the model prediction and the real pressure value. The model may overshoot or undershoot the actual pressure value, which causes the estimated pressure value to be positively or negatively biased depending on the applied pressure. In contrast to the random error, it cannot be assumed that the systematic error is independent of the load direction. The function describing the load increase may fit the data better than the function for load decrease. The modelling error can therefore be described with a bias for a load increase Δ_l as well as a bias for load decrease Δ_{dl} for every associated voltage value V_{cc} . A pressure measurement $p(V_{cc})$ can therefore be denoted as follows:

$$p(V_{cc}) = \begin{cases} F_l(V_{cc}) + \Delta_l(V_{cc}) \pm \delta p(V_{cc}) & \text{for a load increase} \\ F_{dl}(V_{cc}) + \Delta_{dl}(V_{cc}) \pm \delta p(V_{cc}) & \text{for a load decrease} \end{cases} \quad (6.4)$$

Note that Equation 6.4 is only valid for the uncertainty in the measurements over a full range, described by the major conversion curves. In reality, a pressure measurement is described by the variable minor curves $f_{l,k}$ and $f_{dl,k}$ with the associated biases $\delta_{l,k}$ and $\delta_{dl,k}$, which depend on the current and previous voltage value $V_{cc}(k)$ and $V_{cc}(k-1)$. Therefore, a more accurate description of the relation above can be defined as follows:

$$p(V_{cc}(k)) = \begin{cases} f_{l,k}(V_{cc}(k)) + \delta_{l,k}(V_{cc}(k)) \pm \delta p(V_{cc}) & \text{for } V_{cc}(k) \geq V_{cc}(k-1) \\ f_{dl,k}(V_{cc}(k)) + \delta_{dl,k}(V_{cc}(k)) \pm \delta p(V_{cc}) & \text{for } V_{cc}(k) < V_{cc}(k-1) \end{cases} \quad (6.5)$$

A more accurate estimation of the measurement uncertainty would therefore require data obtained from measurements over different ranges, which can be used to estimate the biases associated to the minor curves. However, this exceeds the limitations of the available actuation system and was therefore out of scope for this study, which focused on providing an estimation based on Equation 6.4 only.

6.3 RESULTS

6.3.1 Hysteresis Compensation Model

Every loading cycle resulted in a plot of time against voltage as depicted in Figure 6.4. Each load increment yields a constant voltage value in the creep compensated signal. As such, a dataset of discrete voltage values was obtained for each load-deload test. Computing the mean of five of these datasets allows one to fit a function estimating the conversion curve from voltage to force for loading and deloading. The curve fitting tool in MATLAB was used to model the relation between voltage and force using polynomial regression with the least absolute residual (*LAR*) robust method. The *LAR* robust method was chosen as this method assumes less anomalies in the data and weighs every data point equally, which is believed to be valid in this case as the curve is fitted through the means of the data points. A first, second, third and fourth order polynomial function was fitted to the dataset and the respective RMSE were analyzed (Figure 6.5). A third order polynomial function was found to be optimal. The major conversion curves can therefore be described with the following functions:

$$F_l(V_{cc}) = a_0 V_{cc}^3 + b_0 V_{cc}^2 + c_0 V_{cc} + d_0 \quad (6.6)$$

$$F_{dl}(V_{cc}) = a_1 V_{cc}^3 + b_1 V_{cc}^2 + c_1 V_{cc} + d_1 \quad (6.7)$$

with $d_0 = d_1 = P_0 = 0kPa$ being the output for no load. The curve fitting tool in MATLAB was used to estimate the parameters a_0, b_0 and c_0 . For each of the 15 FSRs a conversion curve could be computed for the load and deload data (Figure 6.6a), allowing a measured voltage value to be mapped to a respective pressure value. The inverse of these conversion curves represents the hysteresis behavior of the FSR (Figure 6.6b).

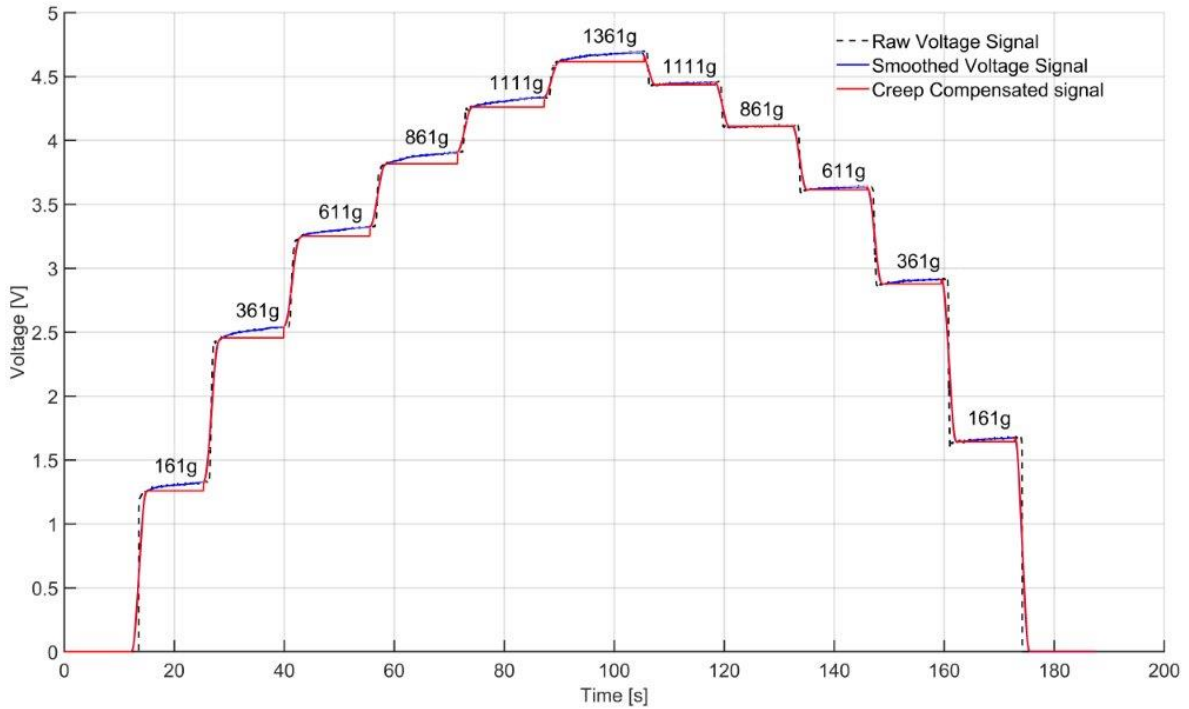


Figure 6.4: A plot of time against voltage as a result of a load-deload test. The higher output for a similar load when deloading is clear evidence of the hysteresis behavior of the force sensitive resistor (FSR). The creep can also be observed to be more significant during loading than during deloading.

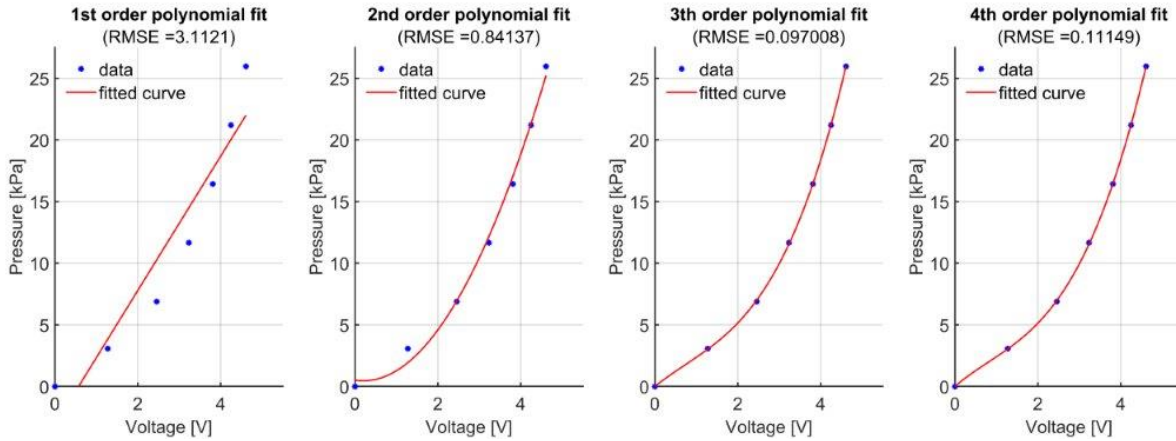


Figure 6.5: Plots for a first, second, third and fourth order polynomial fit to the loading data obtained from the sensor response depicted in Figure 6.4. Similar root mean square errors (RMSE) were found for the fourth and third order polynomial fit.

Based on the major curves, a set of equivalent minor curves can be defined for both loading and deloading. The minor deload curves can easily be obtained by manipulating the a_1 parameter while keeping b_1 and c_1 constant as for these curves $f_{dl,k}(0) = 0$ also applies. The minor load curves on the other hand can not so easily be computed as the latter does not apply. However, assuming that these curves also follow a third order polynomial function and converge to the major load curve towards the maximum load value, the minor load curves can be obtained by performing polynomial regression over its previous value and a set of three points estimated by the major loading curve towards the outer end of the range. The curve fitting tool in MATLAB is therefore used to find a third order polynomial fitting the previous data point $[V_{cc}(k-1), p(k-1)]$ and set of three fixed data points on the major curve defined by $F_l(V_{cc,max} - 2e)$, $F_l(V_{cc,max} - e)$ and $F_l(V_{cc,max})$. The value for $V_{cc,max}$ was the maximum measured value for the loading tests and e was an increment value that was chosen to be $0.05V$. Instead of the LAR robust method, the minor load curves are estimated using the *Bisquare* method, which estimates the fit by minimizing the weighted squared sum of the residuals. The fit is therefore affected less by the fixed data points on the major load curve, which are certain to be outliers. A more detailed version of the Algorithm 6.2 is given in 6.3. The resulting (major and minor) conversion curves are given in Figure 6.6a.

Algorithm 6.3: V-p Conversion Algorithm (*detailed*)

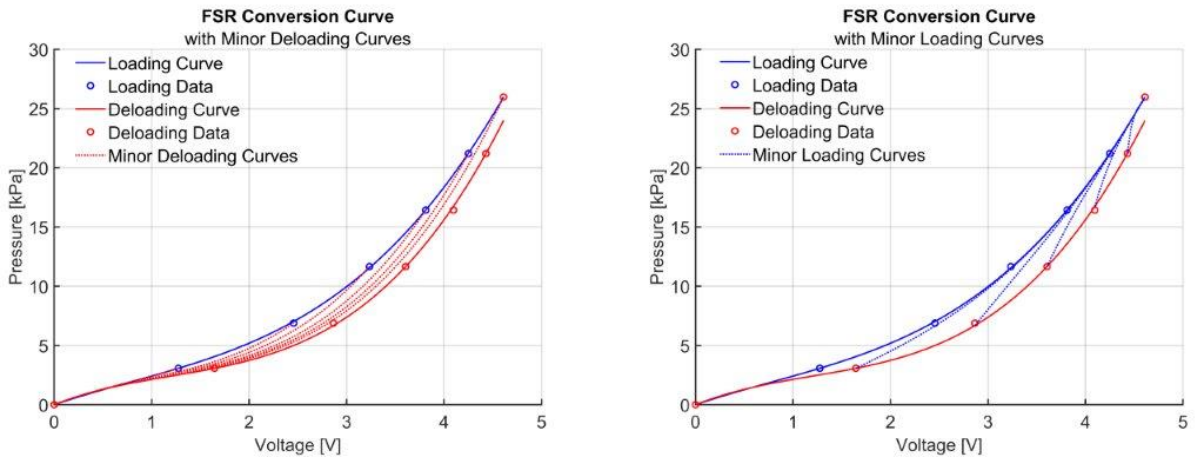
Input: The creep compensated signal V_{cc} , the parameters of the major curves a_0, b_0, c_0, a_1, b_1 and c_1 and a value for $V_{cc,max}$ and e

Output: The pressure signal p with length n

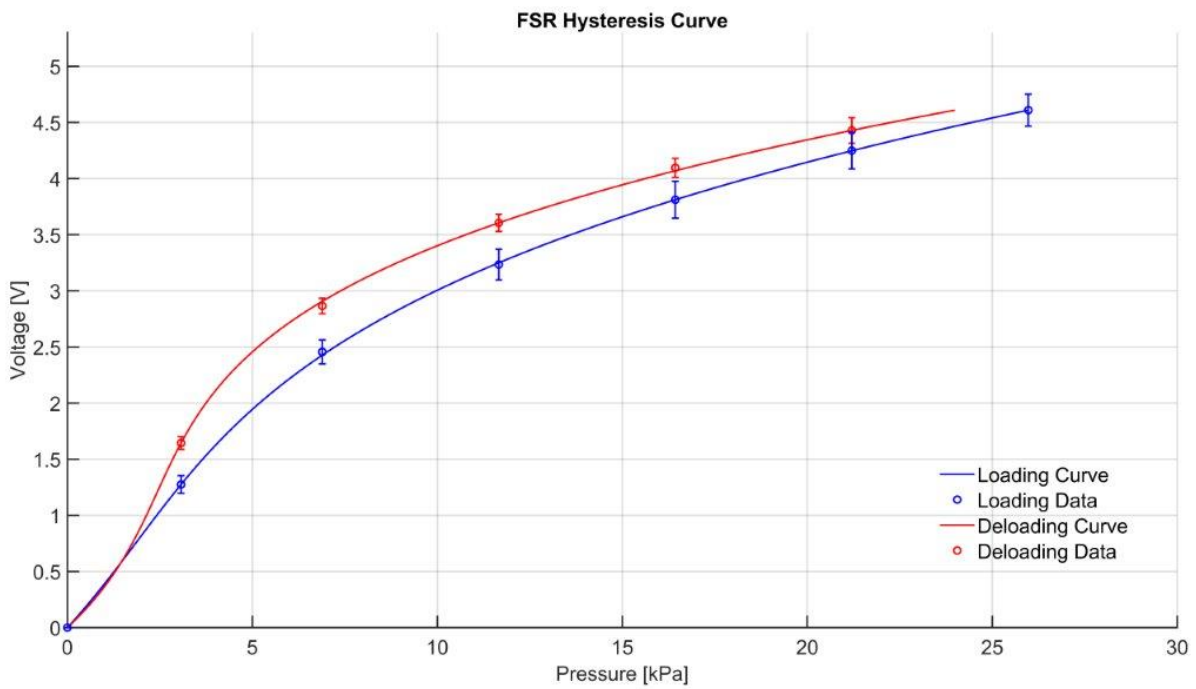
```

1  $p(V_{cc}(1)) = F_l(V_{cc}(1));$ 
2 for  $k = 2 \rightarrow n$  do
3   if  $V_{cc}(k) \geq V_{cc}(k-1)$  then
4      $x_{data} = [V_{cc}(k-1), V_{cc,max} - 2e, V_{cc,max} - e, V_{cc,max}];$ 
5      $y_{data} = [p(k-1), F_l(V_{cc,max} - 2e), F_l(V_{cc,max} - e), F_l(V_{cc,max})];$ 
6      $[a_{0,k}, b_{0,k}, c_{0,k}, d_{0,k}] = fit(x_{data}, y_{data}, 3^{th});$  % find variable parameters
7      $f_{l,k}(V_{cc}(k)) = a_{0,k}V_{cc}^3(k) + b_{0,k}V_{cc}^2(k) + c_{0,k}V_{cc}(k) + d_{0,k};$  % minor loading curve
8      $p(V_{cc}(k)) = f_{l,k}(V_{cc}(k));$ 
9   else
10     $a_{1,k} = (p(k-1) - b_1V_{cc}^2(k-1) - c_1V_{cc}(k-1)) / V_{cc}^3(k-1);$  % find variable parameter
11     $f_{dl,k}(V_{cc}(k)) = a_{1,k}V_{cc}^3(k) + b_1V_{cc}^2(k) + c_1V_{cc}(k);$  % minor deloading curve
12     $p(V_{cc}(k)) = f_{dl,k}(V_{cc}(k));$ 

```



(a)



(b)

Figure 6.6: Figures showing (a) the conversion curves with minor loading curves and deloading curves for conversion of voltage to pressure and (b) the hysteresis behavior of the force sensitive resistor (FSR) including the error margins representing $\pm 1.96SD$ (standard deviation). Note that the hysteresis curve in (b) is identical to the conversion curves in (a), but inverted.

6.3.2 Measurement Uncertainty

With the data from the 15 integrated FSRs the random error could be estimated using Equations 6.1, 6.2 and 6.3. This yielded an estimate of the random error for loading and deloading based on the root mean square of the standard deviation data from all FSRs. Assuming that the random error is independent of load direction, the average (root mean square) error is calculated using Equation 6.3. The random error is given in Figure 6.7a relative to the applied pressure (see Table 6.1). An insignificantly higher error was found for a load increase. The average random error was found to be approximately 4% throughout the entire range.

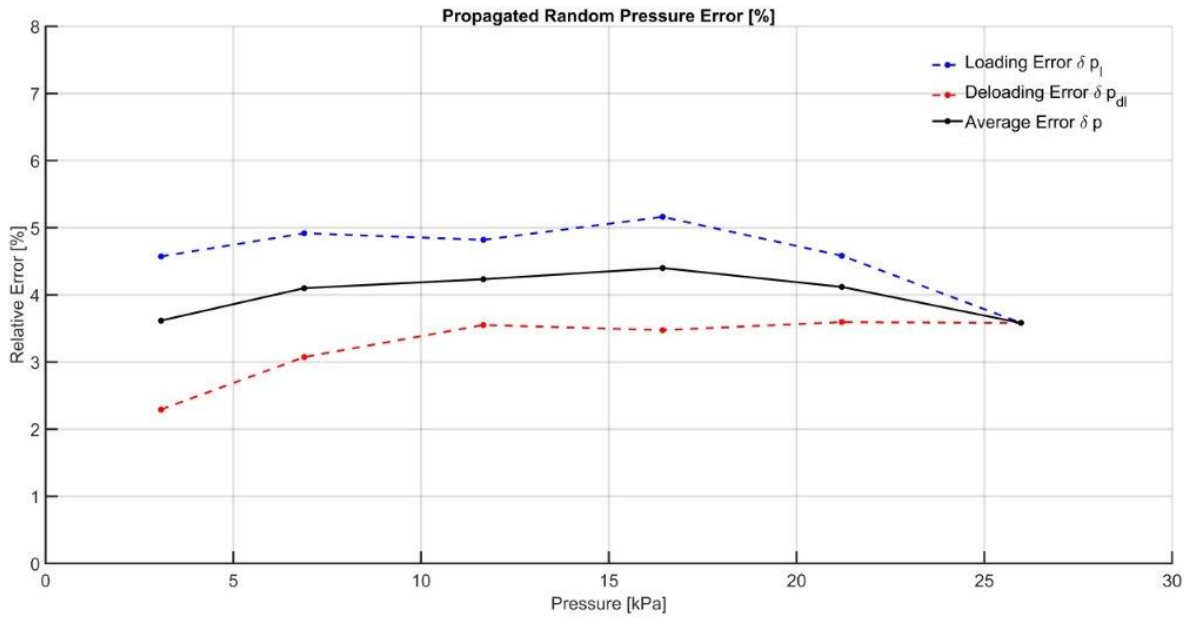
As discussed in Section 6.2.4, an additional systematic error should be defined, resulting from the difference between the real pressure and the predicted pressure. This difference can be visualized with a Bland-Altman (BA) plot, which is a method for qualitative analysis of the relation between two variables. Typically, it displays the average between two parameters versus their difference as well as the mean bias and the 95% limits of agreement. The mean bias is calculated as the mean of all systematic errors and displays whether the model typically overshoots or undershoots the real value. The limits of agreement on the other hand are calculated as the mean bias \pm 1.96 times the standard deviation of the difference between the two parameters and are used to depict the 95% confidence interval of the differences between the two parameters. The BA-plots in Figure 6.7b depict the relative systematic error between the predicted pressure and the applied pressure based on the major loading and deloading curves that were fitted to the data.

When looking at the BA-plot for the loading curve, a slightly positive mean bias can be observed of +0.94%. The modeled value seems to overshoot the real pressure in the lower range beyond the limits of agreement for 4 of the 15 FSRs, with an outlier overshooting the real pressure by 38.6%. The opposite seems to be the case for the deloading curve, which seems to typically undershoot the real pressure (Mean Bias = -2.64%). However, one can see three points for the major deloading curve that showed a 0% relative difference for all 15 FSRs. This means that all the deloading curves coincided perfectly with the data in these points. The plots show that the fitted curves provide a reasonable estimate of the real pressure, with the bias for the loading curve having a 95% confidence interval of [-10.41, 12.31]% and for the deloading curve of [-13.55, 8.28]%.

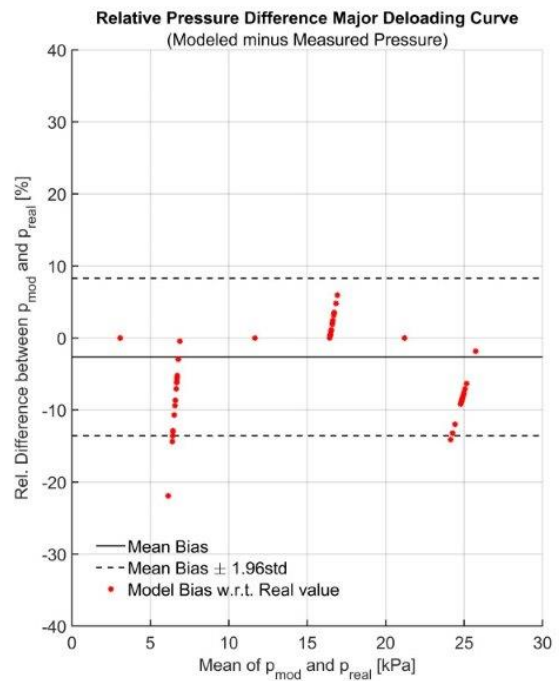
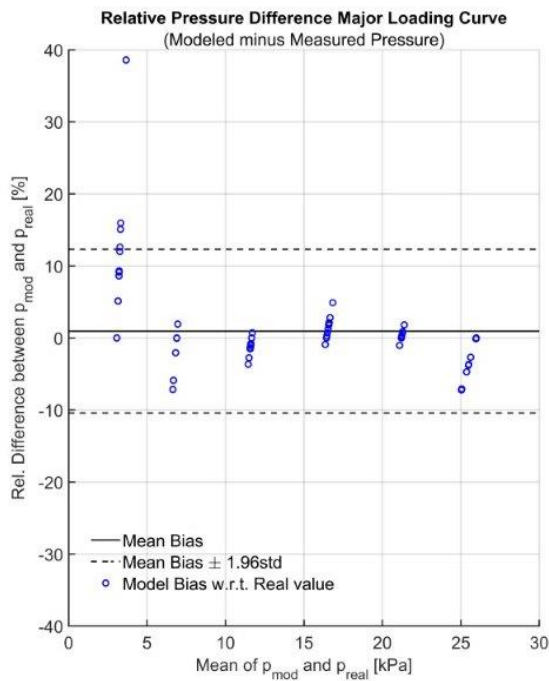
6.4 DISCUSSION

The study discussed in this chapter showed a method for converting a measured voltage signal to a pressure signal based on a generic model describing the hysteresis behavior of the integrated FSR. The model was based on a set of fixed parameters describing a conversion curve for a load increase and a load decrease. These parameters were obtained through a series of load-deload tests for each FSR individually. The process of (re)defining these parameters based on these load-deload tests was used for calibration of the FSRs integrated in the sensorpad and is described in more detail in Appendix D. While the method discussed in this chapter seems to yield promising results for compensating the undesired creep and hysteresis behavior of the FSR, there are some limitations that should be taken into account when interpreting these results.

First of all, it should be noted that the tests were not conducted in a controlled environment with a constant temperature. As the resistance of the FSRs is expected to be affected by temperature, it should be taken into account that their behavior at body temperature may be different than at room temperature. In general, FSRs become increasingly more resistive as ambient temperature increases [71, 72]. The higher body temperature may therefore result in a lower voltage signal for a certain load than it would be at room temperature, causing the measured pressure to be lower than the actual value. Future studies should therefore consider using a heated bed in their test setup to eliminate any possible error that might occur as a result.



(a)



(b)

Figure 6.7: Figures showing the estimated random and systematic error. (a) Plot showing the average propagated random error as calculated using Equation 6.1 and 6.2 for loading, deloading and the average of the two. (b) Bland-Altman plots showing the relative difference between the modeled pressure and the real pressure $(p_{mod} - p_{real})/p_{real} \times 100\%$ for major loading and deloading curves for all 15 force sensitive resistors including the limits of agreement (dashed line) which illustrates the mean ± 1.96 times the standard deviation of the difference between the modeled pressure value p_{mod} and the measured pressure value p_{real} .

Second of all, it was found that the FSRs decreased significantly in sensitivity throughout the testing period, causing significant differences in sensitivity between FSRs. However, it was found that this decrease in sensitivity seemed to be most significant for the first 20 to 30 loading cycles after which

the FSR would remain relatively constant in its sensitivity. While the exact reason for this decreased sensitivity is not certain, it may possibly be related to permanent deformation of the sensor, that causes the properties of the sensor to change drastically within the first loading cycles. It is therefore recommended that the FSRs go through a cyclic preloading procedure prior to their application. Nevertheless, a large inter-part variability may still remain, making simultaneous operation of the FSRs as required for the sensor pad problematic. Individual calibration of the FSR is therefore crucial to ensure a proper operation of the sensor array. This also involves tuning the sensitivity of the FSRs by changing the variable resistor value of R_m to ensure that all sensors are sensitive within approximately the same range. In Appendix D it is explained in more detail how this is applied during calibration of the entire sensor pad.

In addition to this, it should be noted that the random error that was found in this study may only describe the error after the two excitation load cycles and when the sensor is loaded exactly as described in the test procedure. While the error is very similar to the values advertised in the datasheet of the FSR 402 (single part repeatability of 2 - 5%) [37], a higher error is to be expected in practice. This is because the initial load that is applied to the sensor may result in a higher error than the subsequent load increments, as the resulting deformation of the FSR's microstructure may be less predictable. A better estimate of the random error may therefore be obtained by performing single load tests, where the FSR is loaded and deloaded a couple of times with different loads from 0 to F_{load} .

Finally, it should also be noted that the systematic error visualized in the BA plots in Figure 6.7b only provides an estimate of the bias in the predicted pressure value when the sensor is loaded and deloaded over its full range and can be predicted by the major curves. In that case, the BA plots essentially provide a visual assessment of the fitted curve. The difference between the real pressure and the fit is determined by the chosen settings when using the curve fitting tool in MATLAB. The LAR robust method that was used in this case makes the fit less sensitive to extreme outliers. This explains why the fit coincides perfectly with some datapoints in the deloading curve. The BA plots show that on average, the loading curves provide a reasonable estimate of the real pressure, which is evidence that the third order polynomial is suitable to describe the hysteresis behavior of the sensors. While the FSR is expected to show the same behavior when pressure is described by the minor curves, further research is required to assess the systematic error for loading cases other than the one used in this study.

7

EVALUATION OF BRACE FUNCTION FOR A CHENEAU TYPE SCOLIOSIS BRACE

7.1 INTRODUCTION

This chapter discusses a preliminary study that served as validation of the developed prototype. The metrics discussed in Chapter 2 were quantified for a scoliosis brace of a patient with mild scoliosis. As this first version of the prototype does currently not allow yet for long term monitoring, this study was aimed at illustrating the possibility of functional brace evaluation with the prototype using the metrics that were defined for this purpose.

For the purpose of this validation, this study aims to describe the function of the lumbar pad in a seated and a standing position. As braces are commonly fitted in a standing position, it is hypothesized that they will be more optimized for this position than for other positions, even though the patient may not be standing at all for the majority of the time. A study by Harrington et al. (2011) on a total of 111 teenage girls aged 15-18 found that an average of 19 hours per day are spent either sitting or lying down [30]. When taking into account that an estimated 7-9 hours are spent sleeping, it is safe to assume that most of these 19 hours are spent in a seated position. Based on pressure measurements at the lumbar pad, this study aims to find whether a seated position may cause the brace to function differently than expected. As the function of the brace is thought to not only be the result of passive forces, but also additional variable forces as a result of respiratory movement, this study aims to describe the effect of both contributions and how posture may affect this.

7.2 METHODS

7.2.1 Patient Details and Research Objective

The subject included for this study was a 15 year old female patient that was treated for a right thoracic-left lumbar (RTLL) curve pattern¹ using a Cheneau type scoliosis brace. The developed prototype was used to measure pressure at the brace-torso interface of the lumbar pad. The focus of this test was to describe the relation between respiratory movement and the resulting changes in pressure distribution for a seated and a standing position in terms of the previously defined evaluation metrics.

7.2.2 Test Procedure

Test Preparation

Before conducting the measurements, the sensors were calibrated according to the protocol discussed in Chapter 6 and detailed in Appendix D. Calibration was done approximately 1 hour before the measurements. The sensor pad was taped into place at the location of the lumbar pad. The patient was then asked to put on the brace with the sensor pad and tension it loosely. The sensorbelt was secured around the waist and connected to the sensor pad and a laptop that was used to read out the measurements (*HP Z-book G7 Workstation*).

¹ **Out of brace:** 24 degrees right thoracic, 17 degrees left lumbar, **In brace:** 17 degrees right thoracic, 12 degrees left lumbar (see Figure 7.3a)

Test Protocol

Once the device was properly installed and ready for measurement, a series of three measurements were conducted in each position. For all measurements, the patient's breathing tempo was coached using a breathing exercise called *box breathing*. The exercise requires the patient to inhale for 4 seconds, hold their breath for 4 seconds, exhale for 4 seconds and hold their breath again for 4 seconds. The exercise can be visualized as a box where each side represents one of the four phases of this breathing cycle. Using this, a more manageable dataset could be created, where the estimated breathing frequency was assumed to remain constant. This allowed for the relation between respiratory movement and pressure distribution to be more easily identified.

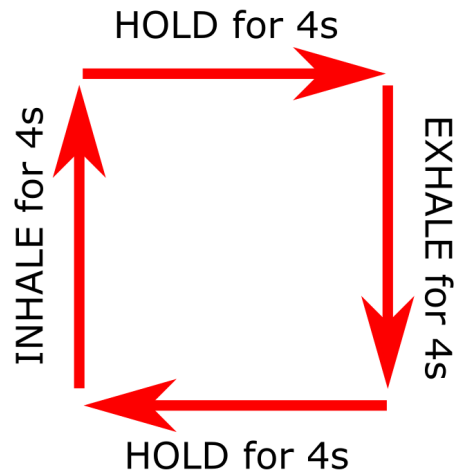


Figure 7.1: Figure visualizing the box breathing exercise resulting in a controlled breathing pattern with a 4 second inhale, 4 second hold, 4 second exhale and a 4 second hold.

The exercise was guided by a youtube video² that coached the patient when to inhale, hold and exhale. The video was played on a smartphone that was placed on a stand directly in front of the patient. Each measurement was conducted with the following protocol:

1. The patient is asked to tension the brace as prescribed.
2. The sensor belt is turned on by the researcher.
3. Measurement is started by opening the serial port in MATLAB.
4. Patient assumes required position.
5. Box breathing exercise is started.
6. Patient starts exercise with a 4 second inhalation.
7. Patient follows the exercise for approximately 120 seconds.
8. Measurement is stopped by closing the serial port in MATLAB
9. The sensor belt is turned off again by the researcher
10. The patient returns to a standing position.
11. The patient loosens the brace straps.

² <https://www.youtube.com/watch?v=aPYmZOOhJF5Q&t=51s>

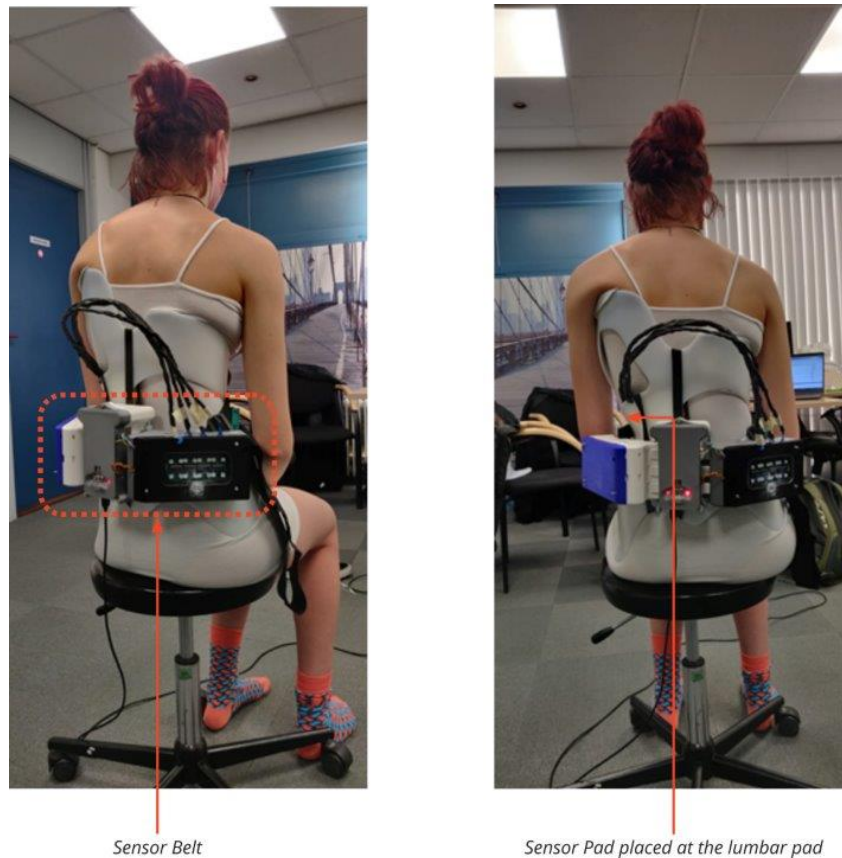


Figure 7.2: Patient in a seated position during one of the measurements with the sensor belt mounted around the waist and the sensor pad taped into place at the lumbar brace pad.

The patient would start all measurements in a standing position. At Step 4 of the protocol the patient would remain in this position for the standing tests or would sit down for the seated tests. A measurement would take approximately 150 seconds as Step 1 - 4 would take roughly 30 seconds on average. A series of two measurements were done in each position to familiarize the patient with the exercise and the protocol in general. This was followed by a series of three tests that were done for the standing position and three measurements that were done for the seated position. All measurements followed a pause of roughly 2 minutes that was used to process and save the measurement data.

7.2.3 Evaluation Metrics

Once the measurements were performed, the data was processed for further analysis. Using the model discussed in Chapter 6, the recorded data obtained from each measurement was translated from a digital voltage signal to a pressure signal for each of the 15 integrated FSRs in the sensor pad. Knowing the relative 2D coordinates of the sensors, the associated 3D global locations were obtained using the mapping method discussed in Chapter 5. The orthotist was consulted for digital placement of the lumbar pad. The interface that was developed was used to place the pad according to the real location of the lumbar pad in the brace. The global sensor locations that followed from the grasshopper script were then loaded into MATLAB. The 3D geometry of the spine was reconstructed with the standard 2D AP radiograph using the reconstruction method discussed in Chapter 5. The global coordinates of the inferior intervertebral discs (IVD) of the L1-L5 vertebrae were also loaded into MATLAB. By combining the reconstructed geometry with the measurement data, the metrics defined in Chapter 2 were quantified for each of the associated evaluation types.

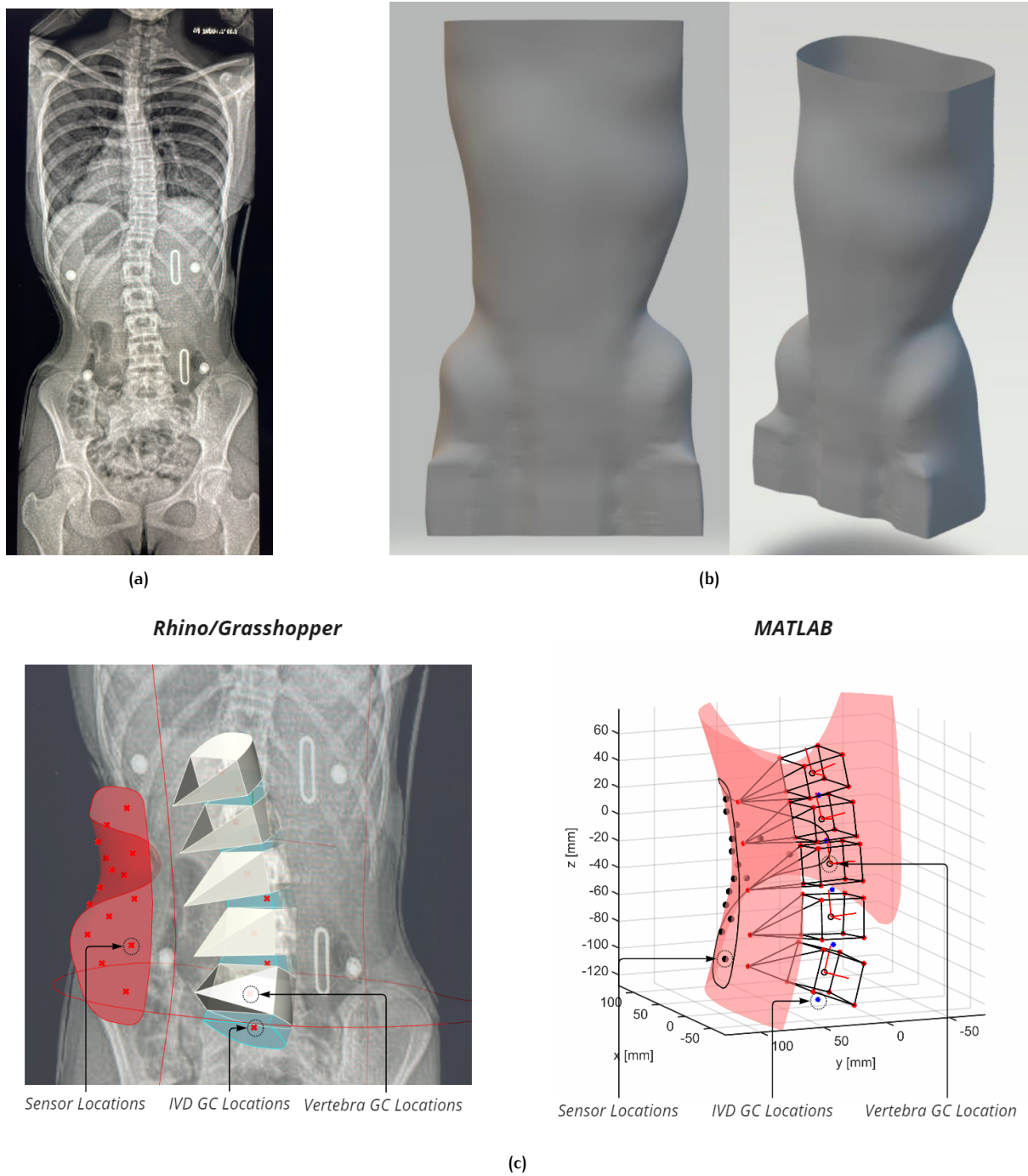


Figure 7.3: Figures Illustrating the (a) Standard in-brace AP radiograph of the patient, (b) Geometry of the inner surface of the brace and (c) Reconstructed model of the lumbar spine and the lumbar sensor pad in Rhino/Grasshopper and in MATLAB including the sensor locations, the intervertebral disc (IVD) centroids (GC) and the vertebra centroids with the reconstructed model in MATLAB also including the vertebra frames (see Section 5.3.6).

One Dimensional Evaluation Metrics

As discussed in chapter 2, the mean pressure magnitude $P_{avg}(t_i)$ as well as the pad pressure variance $s_p^2(t_i)$ can be calculated using the measured data of all individual pressure sensors and does not require any information on spatial locations. In addition, the moving average of the mean pressure magnitude $P_{avg,ma}(t_i)$ can be computed by averaging the signal over a time window of length $n\hat{T}_{bc}$ with $P_{avg,ma}(t_i) = NaN$ for the interval $t_i = [0, n\hat{T}_{bc}]$. The average breathing cycle period \hat{T}_{bc} can be

computed from the measurements in each position, yielding a value for the seated position ($\hat{T}_{bc,se}$) as well as for the standing position ($\hat{T}_{bc,st}$). A value of $n = 2$ was found to be optimal for smoothing out the pressure differences due to respiratory movement.

In order to give a more general representation of the measurements which would allow for comparison of the data resulting from both postures, an **average breathing cycle** is computed for the seated as well as the standing position. This is done by identifying all cycles for the three measurements done in each position and combining them, while scaling them in length to match the average breathing cycle period \hat{T}_{bc} for the associated position (see Figure 7.4). Averaging all cycles results in the average breathing cycle, which describes the (average) mean pressure magnitude signal $\hat{P}_{avg}(t_m)$ related to one cycle of the box breathing exercise, with t_m being any time instance within $[0, \hat{T}_{bc}]$. In a similar fashion, the variance *between* breathing cycles $s_{bc}^2(t_m)$ can be calculated, which can be used as a metric for the repeatability of each part of the breathing cycle. As the average breathing cycle data is useful for comparison of the two postures, it will also be used for the four and five dimensional evaluation.

Three Dimensional Evaluation Metrics

Using the dimensions of the sensor pad and the associated integrated FSR locations, a pressure distribution can be described for every time instance. This is done using the average breathing cycle signal for each sensor individually, which is denoted as $\hat{p}_k(t_m)$, with $k = 1, 2, \dots, 15$ and corresponds to the number/location of the sensor. The average breathing cycle signals of all sensors can be combined in one vector:

$$\hat{\mathbf{P}}(t_m) = \begin{pmatrix} \hat{p}_1(t_m) \\ \vdots \\ \hat{p}_{15}(t_m) \end{pmatrix} \quad (7.1)$$

Using bilinear interpolation [19], a heat map can be constructed, representing the pressure at every location within the 15 sensor locations. The resolution of the pressure distribution is determined by the grid dimensions of the two dimensional mesh defined in MATLAB. The constructed mesh consisted of 50 x 50 nodes with individual nodes being 2.5mm apart (see Figure 7.5).

In addition to the heat map, the COP can be calculated. Equation 7.2, describing the x and y component of the COP locaton, can also be represented in vector notation. In a local two dimensional frame \mathcal{N} describing the sensor locations, the COP at time instance t_m can be denoted as follows:

$${}^{\mathcal{N}}\mathbf{COP}(t_m) = \begin{pmatrix} {}^{\mathcal{N}}COP_x(t_m) \\ {}^{\mathcal{N}}COP_y(t_m) \end{pmatrix} = {}^{\mathcal{N}}\mathbf{X}_s \hat{\mathbf{P}}(t_m) [\mathbf{J}_{1,15} \hat{\mathbf{P}}(t_m)]^{-1} \quad (7.2)$$

with ${}^{\mathcal{N}}\mathbf{X}_s$ being a time-independent matrix describing the sensor locations in the local two dimensional frame \mathcal{N} :

$${}^{\mathcal{N}}\mathbf{X}_s = \begin{pmatrix} {}^{\mathcal{N}}x_1 & \cdot & \cdot & \cdot & {}^{\mathcal{N}}x_{15} \\ {}^{\mathcal{N}}y_1 & \cdot & \cdot & \cdot & {}^{\mathcal{N}}y_{15} \end{pmatrix} \quad (7.3)$$

and $\mathbf{J}_{1,15}$ being a vector of 1 by 15 containing only ones:

$$\mathbf{J}_{1,15} = (1 \quad \cdot \quad \cdot \quad \cdot \quad 1) \quad (7.4)$$

As such, the COP at every time instance t_m can be computed, yielding a trajectory in the \mathcal{N} frame for both positions for the time interval $[0, \hat{T}_{bc}]$.

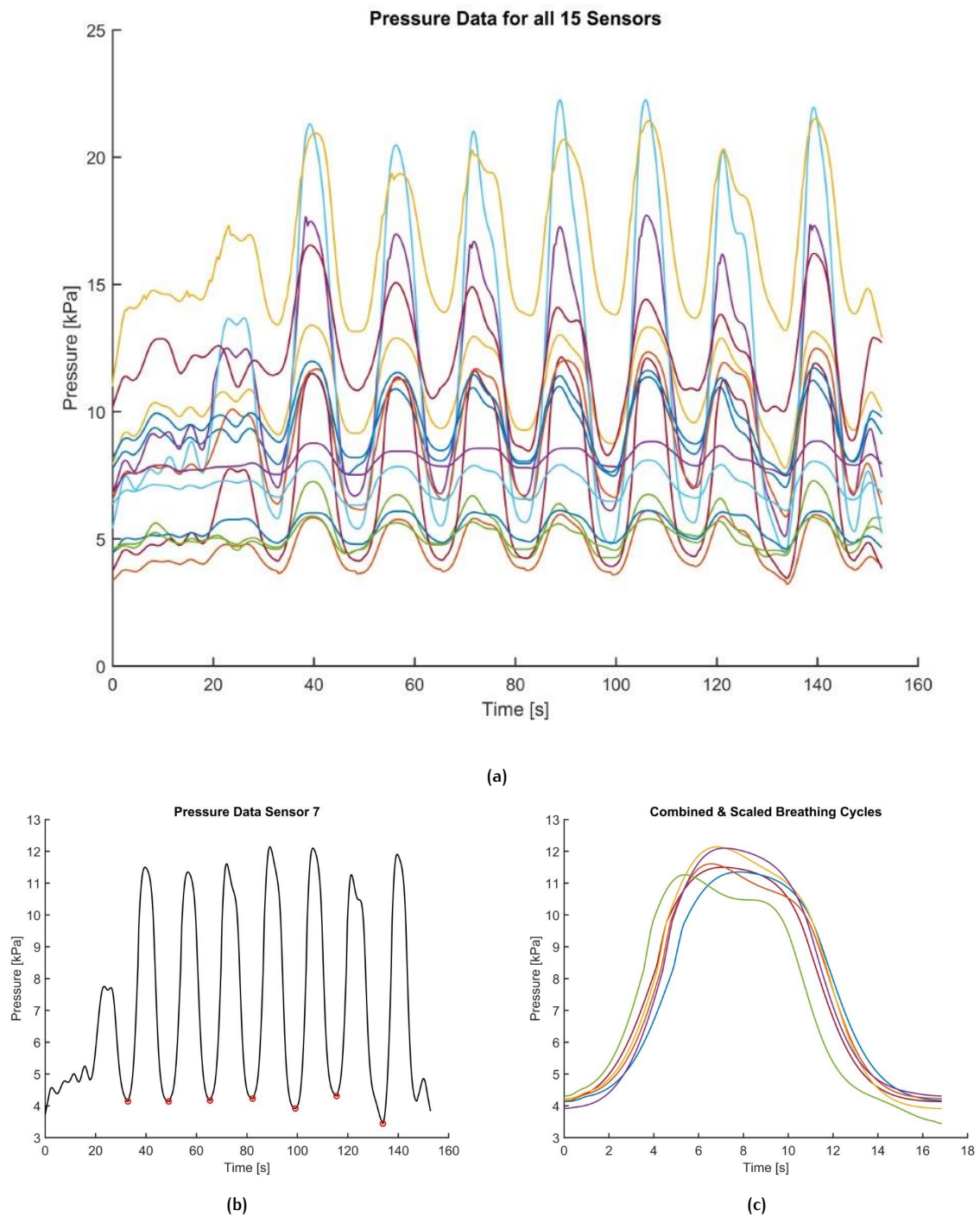


Figure 7.4: Figures illustrating the computation of an average breathing cycle. **(a)** Plot of the pressure data of all 15 sensors combined obtained from a measurement as described in Section 7.2.2. **(b)** Plot of the pressure data of a single sensor including the identified minima used to define the breathing cycles. **(c)** Plot combining the identified breathing cycles from (b) and scaled in length to the average breathing cycle period \hat{T}_{bc} .

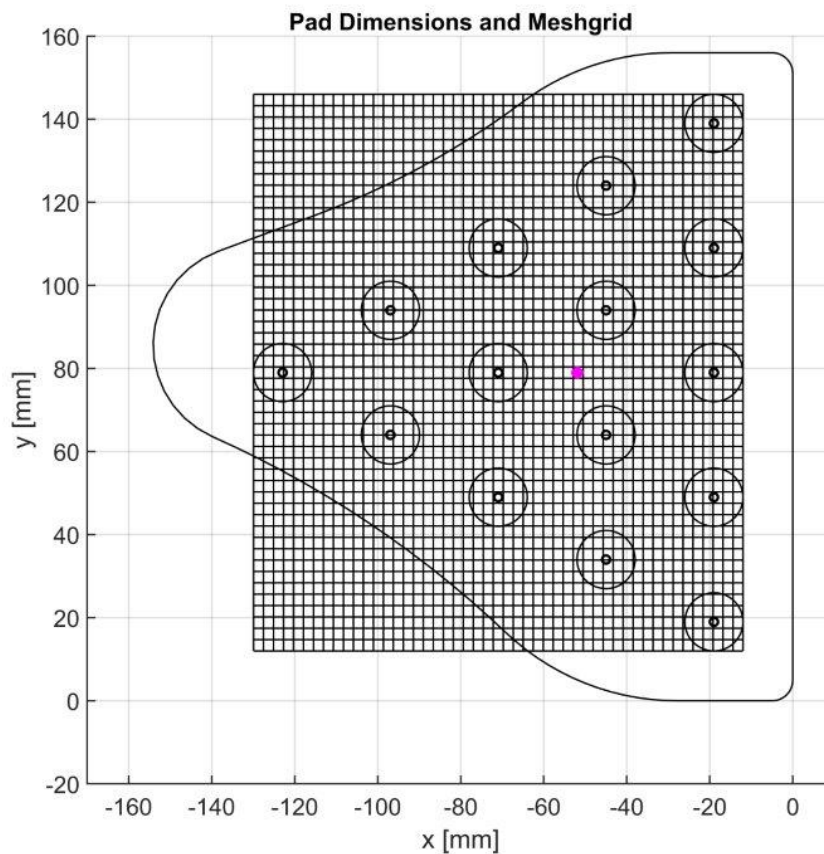


Figure 7.5: Figure showing the meshgrid that was used for linear interpolation of individual pressure measurements. The circles represent the sensor location and with respect to the outer edges of the sensor pad. The purple dot represents the geometric center of the lumbar pad, which coincides with the geometric center of the sensor array.

Four Dimensional Evaluation Metrics

Using the average pressure magnitude, the global COP location, the global vertebra centroid locations/orientations and the global centroid locations of the IVDs, the lumbar contribution to the equivalent bending moments can be calculated for each vertebra individually. This requires the computation of the equivalent lumbar force vector ${}^M\mathbf{F}_{lb}(t_m)$ and a position vector ${}^M\mathbf{d}_{lb,Vxy}(t_m)$, which are both described in the three dimensional global M frame. Both the force vector and the position vector depend on the global COP location ${}^M\mathbf{COP}(t_m)$, which can be calculated using equation 7.2 by substituting ${}^N\mathbf{X}_s$ for ${}^M\mathbf{X}_s$, representing the global sensor locations in a three dimensional frame M :

$${}^M\mathbf{X}_s = \begin{pmatrix} Mx_1 & \dots & Mx_{15} \\ My_1 & \dots & My_{15} \\ Mz_1 & \dots & Mz_{15} \end{pmatrix} \quad (7.5)$$

The mapping of the sensor locations from the N frame to the M frame is done using the Grasshopper script discussed in chapter 5. Recalculating the COP location ${}^M\mathbf{COP}(t_m)$ yields a global x-component ${}^M\text{COP}_x(t_m)$, a global y-component ${}^M\text{COP}_y(t_m)$ and a global z-component ${}^M\text{COP}_z(t_m)$.

Using MATLAB, a normal vector can be calculated at the global location ${}^M\mathbf{COP}(t_m)$ at a certain time instance t_m , perpendicular to the torso surface. The equivalent force vector ${}^M\mathbf{F}_{lb}(t_m)$ can then be calcu-

lated using this normal vector and a magnitude that is obtained by multiplying the average pressure magnitude signal with the estimated effective lumbar pad area A'_{lb} :

$${}^M\mathbf{F}_{lb}(t_m) = {}^M\hat{\mathbf{n}}_{\perp COP}(t_m)\hat{P}_{avg}(t_m)A'_{lb} \quad (7.6)$$

The equivalent lumbar bending moments can be calculated using a position vector ${}^M\mathbf{d}_{lb,Vxy}(t_m)$ describing the COP location with respect to the centroid of the IVD Vxy , inferior to vertebra V_y :

$${}^M\mathbf{d}_{lb,Vxy}(t_m) = {}^M\mathbf{COP}(t_m) - {}^M\mathbf{X}_{gc,Vxy} \quad (7.7)$$

with ${}^M\mathbf{X}_{gc,Vxy}$ representing the centroid location of IVD Vxy :

$${}^M\mathbf{X}_{gc,Vxy} = \begin{pmatrix} {}^Mx_{gc,Vxy} \\ {}^My_{gc,Vxy} \\ {}^Mz_{gc,Vxy} \end{pmatrix} \quad (7.8)$$

The equivalent bending moments can then be computed by taking the cross product of the position vector and the equivalent force vector. The equivalent lumbar bending moment over any (lumbar) vertebra $V_y = L1, L2, L3, L4, L5$ represented in the global M frame for a particular time instance t_m can then be calculated as follows:

$${}^M\mathbf{M}_{lb,Vy}(t_m) = {}^M\mathbf{d}_{lb,Vxy}(t_m) \times {}^M\mathbf{F}_{lb}(t_m) \quad (7.9)$$

In a final step, the equivalent bending moments should be represented in the fixed local frame associated to the corresponding vertebra. Using the vertebra dimensions and orientation that followed from the Grasshopper script, a rotation matrix can be computed for each vertebra that describes the local vertebra frame (see Section 5.3.6). The equivalent bending moments can then be projected to the local frame as follows:

$${}^{Vy}\mathbf{M}_{lb,Vy}(t_m) = {}^{Vy}\mathbf{C}_M {}^M\mathbf{M}_{lb,Vy}(t_m) \quad (7.10)$$

with ${}^{Vy}\mathbf{C}_M$ being the rotation matrix mapping the global M frame to the local Vy frame. The equivalent bending moment components expressed in this frame, will be referred to as lateral bending, axial torsion and sagittal bending components respectively (see Figure 2.3).

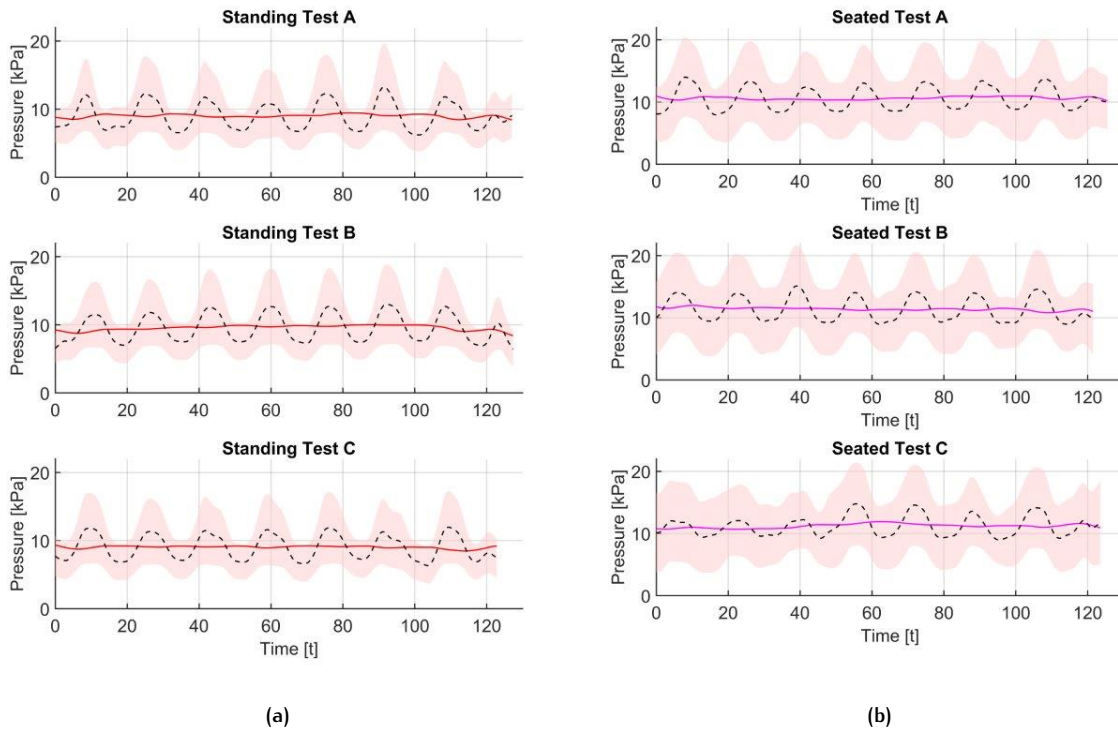


Figure 7.6: The mean pressure magnitude (dashed), moving average mean pressure magnitude (red/purple solid) and the pad pressure variance (red area) for (a) standing and (b) seated position for each of the total of 6 measurements.

7.3 RESULTS

7.3.1 One Dimensional Evaluation

Using the method described in the previous section, the mean pressure magnitude, moving average of the mean pressure magnitude and pressure variance were computed for each of the 6 measurements (Figure 7.6). Figure 7.6a represents the measurements that were taken in a standing position and Figure 7.6b are from the seated position. The dashed line in the figures represent the mean pressure with the bolt red and purple lines representing the moving averages of the standing and seated mean pressure respectively. The pressure variance is visualized as the red zone around the measurement, which represents $P_{avg}(t_i) \pm 1s_p(t_i)$ at every time instance t_i .

When looking at the pressure variance for the measurements in the standing position, it can be observed that it generally tends to increase with inhalation, which means that the pressure does not increase uniformly, but rather in certain locations more than others. A clear difference in pressure variance can be seen with the measurements that were taken in a seated position, which shows a high variance in all phases of the breathing cycle. The higher pressure variance in the seated position is accompanied by a slightly higher moving average of the mean pressure.

The difference in mean pressure magnitude between the two postures is more evident when comparing the average breathing cycles, which are computed as described in Section 7.2.3 and visualized in Figure 7.7. The solid black line represents the mean pressure $\hat{P}_{avg}(t_m)$. The solid red and purple line represent the average mean for the pressure in the standing and seated position respectively. The average mean is a single value for each average breathing cycle and is computed similarly to the moving average, but uses $n = 1$ instead³. The average mean pressure was found to be $10.92 \pm 0.98kPa$ in the standing position and $12.87 \pm 1.3kPa$ in a seated position. While the pressure at the lumbar pad is

³ This is nothing more than the average of all datapoints from the average breathing cycle.

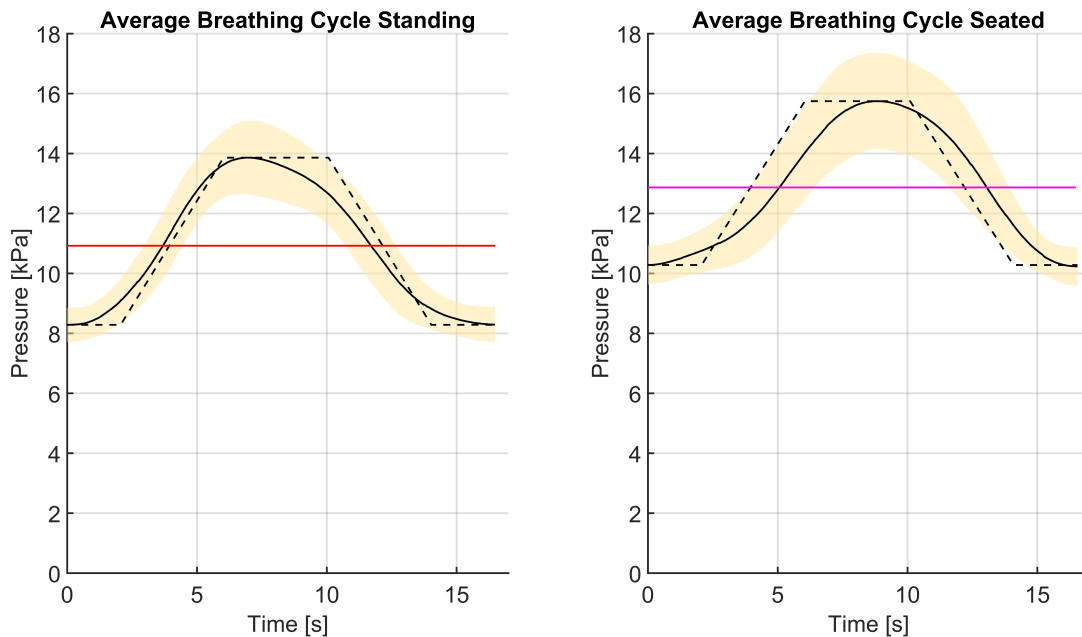


Figure 7.7: The average breathing cycle for (a) a standing and (b) a seated position. The figure shows the mean pressure $\hat{P}_{avg}(t_m)$ (solid black), the (moving) average mean pressure (solid red/purple), the variance between breathing cycles (yellow area) and a theoretic breathing cycle representing an ideal breathing cycle (dashed black) (2s hold-4s inhale-4s hold-4s exhale-2s hold). Breathing cycle periods were $T_{bc,se} = 16.46 \pm 1.08$ s and $T_{bc,st} = 16.54 \pm 0.94$ s for a seated and a standing position respectively.

generally higher in the seated position, the pressure increase as a result of the inhalation was found to be almost identical for both postures. In a standing position the pressure was found to increase with 5.58 ± 1.36 kPa and in a seated position it was found that pressure would increase with 5.51 ± 1.73 kPa.

A difference can also be observed when comparing the *execution* of the exercise, which is reflected by the temporal characteristics of both breathing cycles. The dashed black line in figure 7.7 represents a perfect execution of the box breathing exercise, with a pressure increase from the minimum up to the maximum measured pressure. The breathing cycle should reflect a 2s hold, followed by a 4s inhale, a 4s hold, a 4s exhale and a 2s hold. While both signals are assumed to be affected by smoothing (see Section 6.1.2), it can be observed that the mean pressure signal in the standing position $\hat{P}_{avg,st}(t_m)$ seems to follow the ideal signal much closer than the signal for the seated position $\hat{P}_{avg,se}(t_m)$. The latter can be observed to lag the ideal signal more and reaches its maximum at $t_m = 8.72$ s, whereas for the standing position the maximum pressure is reached at $t_m = 6.89$ s.

In addition to the mean, average mean and theoretical pressure signal, the variance between breathing cycles, denoted as \hat{s}_p^2 , is also visualized in Figure 7.7 as the yellow area, which represents $\hat{P}_{avg}(t_m) \pm 1\hat{s}_p(t_m)$ at every time instance $t_m = [0, \hat{T}_{bc}]$. In Figure 7.8, the pressure variances for both breathing cycles are plotted together. It can be observed that for the measurement in a standing position, the variance increases during the first part of the inhalation, hold and exhalation task and decreases during the second part of each task. The variance reaches its maximum value of $\hat{s}_p^2(t_m) = 1.56$ kPa during the hold task at $t_m = 7.29$ s. For the seated position on the other hand, the variance can be seen to increase throughout the whole duration of the inhalation task. The variance then continues to increase during the first part of the hold task and then decrease up until the start of the exhalation task. A maximum of $\hat{s}_p^2(t_m) = 2.79$ kPa is reached at $t_m = 11.89$ s, about halfway during the exhalation task. While an increase in variance can be observed for each posture during the inhalation - hold - exhalation phase, the generally lower variance in the standing position can be interpreted as a more repeatable breathing cycle for that position.

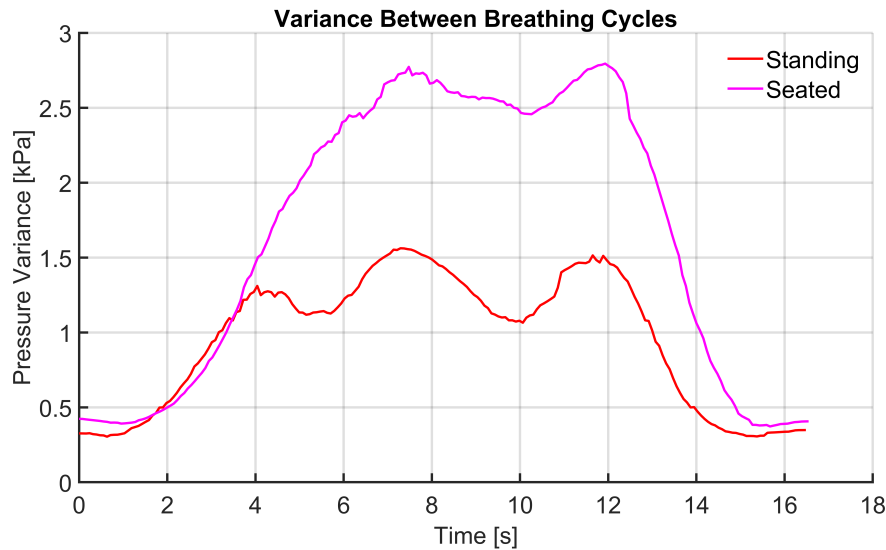


Figure 7.8: Variance between breathing cycles as a function of time for a *standing position* and a *seated position*.

7.3.2 Three Dimensional Evaluation

Having computed the average breathing cycle data for each sensing element within the sensor pad, the related pressure distribution and COP trajectory was computed. Figure 7.9 and Y show the heat maps related to the pressure distribution as well as the COP locations at three time instances during the breathing cycle. For both positions the data is reported for $t_1 = 0s$, $t_2 = 4s$ and $t_{top} = 6.89s/t_{top} = 8.72s$ (top of each breathing cycle). In Appendix F the pressure distribution is also given for both postures at $t_2 = 12s$ and $t_4 = 16s$.

When looking at the pressure distribution at each time instance and comparing the data resulting from the standing position with that of the seated position, some observations can be made that may better describe the data discussed in the previous section. First of all, the heat map shows that the generally higher pressure magnitude that was found for the measurements in the seated position is not caused by a uniform increase in pressure magnitude. Where the pressure variance visualized in Figure 7.6. already showed that that this was the case, the heat maps quantify the exact location of these local pressure points. It can be observed that the seated position may cause pressure to increase locally towards the lower left side of the lumbar pad. An almost equal mean pressure magnitude in both positions at $t_2 = 4s$, being 11.77 ± 1.46 kPa and 11.42 ± 1.29 kPa respectively, can be seen in figure 4. and figure 5. to be the result of a notably different pressure distribution, where the standing position shows more uniformity compared to the seated position.

The data reported in Table 7.1 and 7.2 can also be translated to a COP trajectory, which reflects how the pressure distribution changes during a breathing cycle. Even though the COP only moves a few millimeters, some characteristic differences can be observed between the trajectory resulting from the standing position and the seated position. For example, the local increase towards the lower left side of the pad causes the entire trajectory for the seated position to be shifted in the negative y-direction.

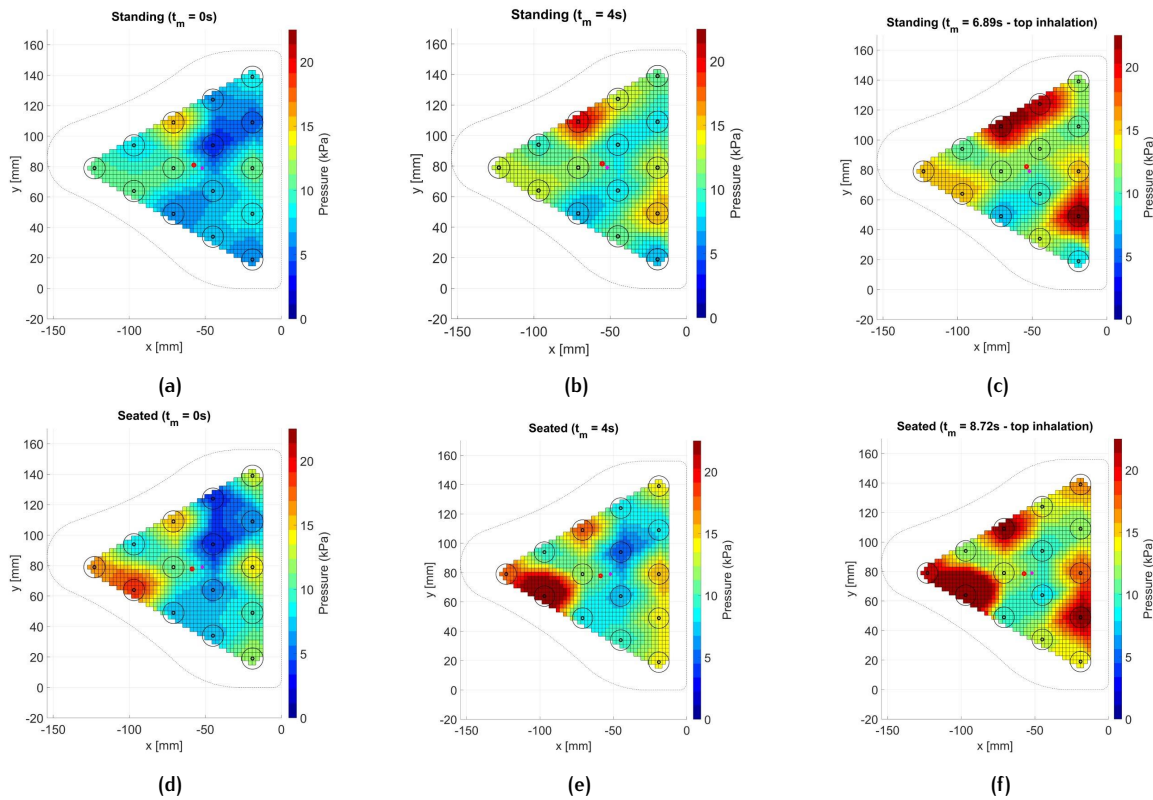


Figure 7.9: Pressure distribution at the lumbar pad area for a standing position during different time instances t_m throughout the average breathing cycle (see Figure 7.7) with (a) $t_m = 0s$, (b) $t_m = 4s$ and (c) $t_m = 6.89s$ and for a seated position at (d) $t_m = 0s$, (e) $t_m = 4s$ and (f) $t_m = 8.72s$

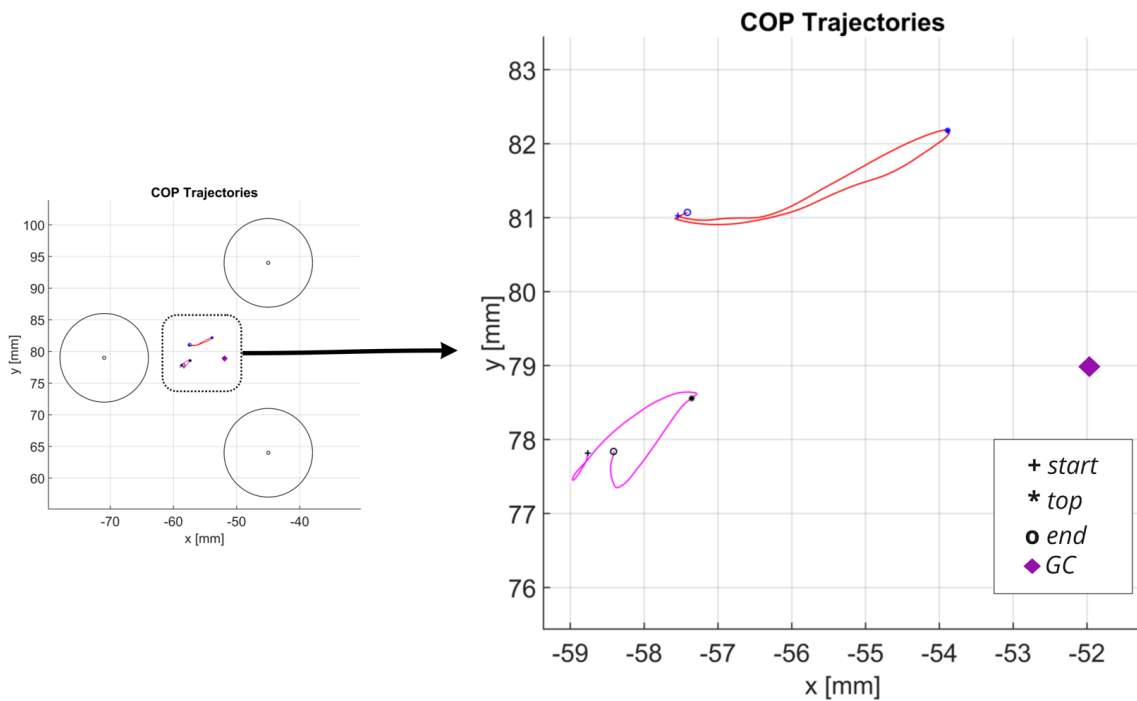


Figure 7.10: Center of Pressure (COP) trajectory for a **standing position** and a **seated position**. The figure on the left shows the trajectories relative to the middle three sensors of the array.

Table 7.1: Center of Pressure (COP) Locations at five time instances during an average breathing cycle for a standing position. Values are given as *mean* \pm *1SD*.

	COP (t=0s)	COP (t = 4s)	COP (t=6.89s)	COP (t=12s)	COP (t=16s)	GC
x[mm]	-57.52 ± 1.17	-55.25 ± 1.19	-53.88 ± 0.94	-55.57 ± 1.30	-57.39 ± 1.18	-51.96
y[mm]	81.03 ± 1.65	81.56 ± 1.76	82.17 ± 1.43	81.26 ± 1.90	81.07 ± 1.66	79.00

Table 7.2: Center of Pressure (COP) Locations at five time instances during an average breathing cycle for a seated position. Values are given as *mean* \pm *1SD*.

	COP (t=0s)	COP (t = 4s)	COP (t=8.72s)	COP (t=12s)	COP (t=16s)	GC
x[mm]	-58.74 ± 1.36	-58.68 ± 1.25	-57.42 ± 1.08	-58.14 ± 1.28	-58.39 ± 1.32	-51.96
y[mm]	77.81 ± 1.80	77.83 ± 1.66	78.64 ± 1.47	77.52 ± 1.70	77.83 ± 1.75	79.00

7.3.3 Four Dimensional Evaluation

In a final step, the equivalent lumbar bending moments were computed using the equations discussed in 7.2.3. Using the rotation matrices that were obtained using the spinal reconstruction method discussed in Chapter 5, the bending moments could be expressed in the associated local frame for each vertebra.

The Figures 7.11a and 7.11b illustrate the change in equivalent bending moment related to the average breathing cycle for a seated as well as a standing position. In addition, in the Tables 7.3-6 the equivalent bending moments are given for $t_m = 0$ and for $t_m = 6.89 / t_m = 8.72s$, which is the point where maximum pressure is reached in the average breathing cycle for a standing/seated position. In the tables, the relative sagittal, lateral and axial bending components (see Figure 2.3) are given as well as the absolute magnitude. The relative components are the result of normalization and thus form

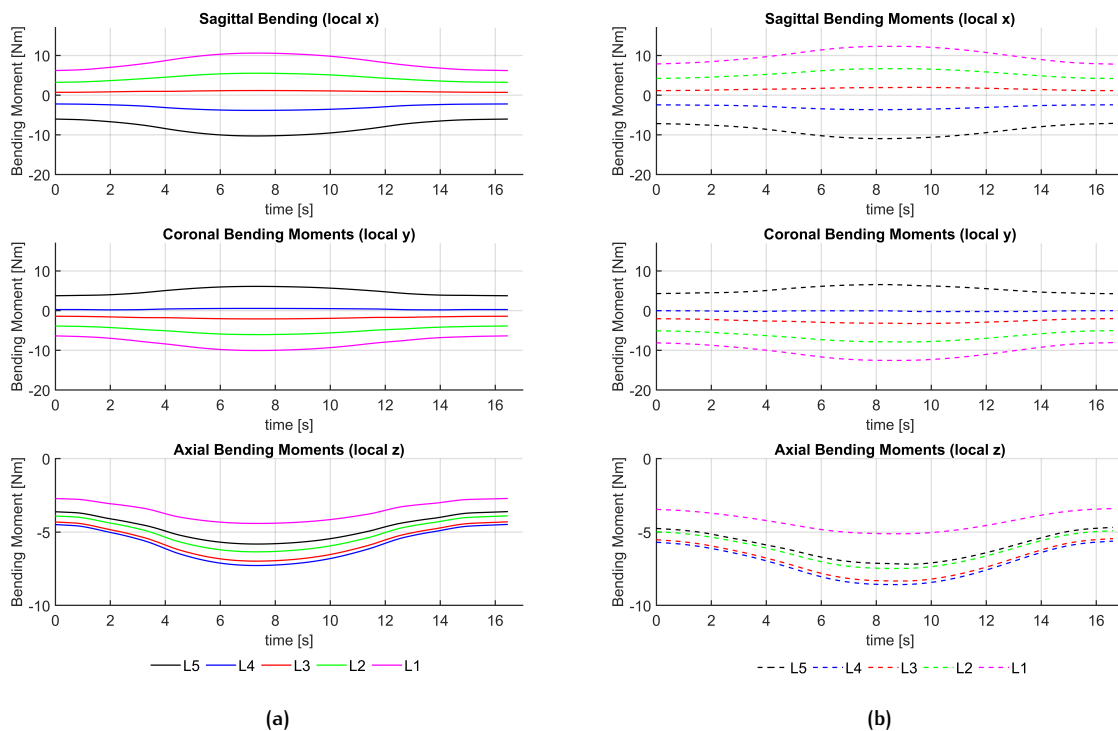


Figure 7.11: The sagittal, lateral(/coronal) and axial bending moment over the L1-L5 vertebrae at every time instant during the associated breathing cycle for a (a) standing position and (b) seated position. Note that the axes for the axial bending moments are scaled for clarity.

Table 7.3: Relative normalized equivalent bending moment components and magnitude for L1 - L5 vertebrae at $t_m = 0$ (during the average breathing cycle as shown in Figure 7.7) for a **standing** position. Values are given as *mean* \pm *1SD*.

	Rel. Sagittal Component [-] ($t = 0s$)	Rel. lateral Component [-] ($t = 0s$)	Rel. Axial Component [-] ($t = 0s$)	Magnitude [Nm]
L5	-0.7558 ± 0.0539	0.4719 ± 0.0490	-0.4539 ± 0.0536	8.0007
L4	-0.4413 ± 0.0277	-0.0544 ± 0.0065	-0.8957 ± 0.0859	5.0315
L3	0.1557 ± 0.0123	-0.3065 ± 0.0243	-0.9391 ± 0.0863	5.0315
L2	0.5078 ± 0.0518	-0.6066 ± 0.0268	-0.6117 ± 0.0692	6.4102
L1	0.6683 ± 0.0708	-0.6841 ± 0.0247	-0.2922 ± 0.0506	9.3403

Table 7.4: Relative *normalized* equivalent bending moment components and magnitude for L1 - L5 vertebrae at $t_m = 6.89$ (during the average breathing cycle as shown in Figure 7.7) for a **standing** position. The last column gives the relative increase in magnitude with respect to the values given in table 6.3 at $t_m = 0s$. Values are given as *mean* \pm *1SD*.

	Rel. Sagittal Component [-] ($t = 6.89s$)	Rel. lateral Component [-] ($t = 6.89s$)	Rel. Axial Component [-] ($t = 6.89s$)	Magnitude [Nm]	Relative Inh. Increase* [-]
L5	-0.7728 ± 0.0324	0.4600 ± 0.0295	-0.4373 ± 0.0322	13.3079	1.6634 ± 0.2522
L4	-0.4649 ± 0.0169	0.4600 ± 0.0295	-0.8827 ± 0.0524	8.2524	1.6401 ± 0.2383
L3	-0.4649 ± 0.0169	-0.2819 ± 0.0152	-0.9462 ± 0.0539	7.3836	1.6017 ± 0.2442
L2	0.5339 ± 0.0320	-0.5827 ± 0.0166	-0.9462 ± 0.0539	10.3672	1.6173 ± 0.2360
L1	0.6954 ± 0.0433	-0.6579 ± 0.0151	-0.2891 ± 0.0310	15.2723	1.6351 ± 0.2227

a unit vector such that the square-root sum of the mean values of the respective sagittal, lateral and axial component is equal to one. The tables 7.4 and 7.6 also provide the relative increase of the bending moment magnitude with respect to the value that was found at $t_m = 0$. The data shows that in both positions the L1 vertebra seems to experience the largest equivalent bending moment magnitude, which can be broken down into a similar sagittal and lateral component and a significantly lower axial component.

When looking at the relative components for both positions, it can be observed that there is no significant difference between the values at $t_m = 0$ and at $t_m = 6.89 / t_m = 8.72$. In addition, the relative increase in equivalent bending moment magnitude as a result of respiratory movement also seems to be similar for all vertebrae in both positions. This means that the equivalent bending moments seem to increase proportionally in all directions during inhalation, regardless of the position. While this is the case, it can be observed that on average the relative increase seems to be slightly (but not significantly) higher in a standing position than in a seated position.

Table 7.5: Relative *normalized* equivalent bending moment components and magnitude for L1 - L5 vertebrae at $t_m = 0$ (during the average breathing cycle as shown in Figure 7.7) for a **seated** position. Values are given as *mean* \pm *1SD*.

	Rel. Sagittal Component [-] ($t = 0s$)	Rel. lateral Component [-] ($t = 0s$)	Rel. Axial Component [-] ($t = 0s$)	Magnitude [Nm]
L5	-0.7445 ± 0.0448	0.4477 ± 0.0407	-0.4952 ± 0.0445	9.6335
L4	-0.3928 ± 0.0224	-0.0043 ± 0.0053	-0.9196 ± 0.0696	6.21175
L3	0.1913 ± 0.0094	-0.3395 ± 0.0186	-0.9209 ± 0.0661	6.0164
L2	0.5106 ± 0.0400	-0.6139 ± 0.0207	-0.6021 ± 0.0535	8.2905
L1	0.6662 ± 0.0557	-0.6861 ± 0.0194	-0.2923 ± 0.0399	11.8646

Table 7.6: Relative *normalized* equivalent bending moment components and magnitude for L1 - L5 vertebrae at $t_m = 8.72$ (during the average breathing cycle as shown in Figure 7.7) for a **seated** position. The last column give the relative increase in magnitude with respect to the values given in table 6.5 at $t_m = 0s$. Values are given as *mean* \pm *1SD*.

	Rel. Sagittal Component [-] ($t = 0s$)	Rel. lateral Component [-] ($t = 0s$)	Rel. Axial Component [-] ($t = 0s$)	Magnitude [Nm]	Relative Inh. Increase* [-]
L5	-0.7209 ± 0.0306	0.4662 ± 0.0278	-0.7373 ± 0.0135	14.1042	1.4641 ± 0.1613
L4	-0.4035 ± 0.0148	-0.0244 ± 0.0035	-0.9146 ± 0.0460	9.3970	1.5128 ± 0.2093
L3	0.1255 ± 0.0063	-0.3630 ± 0.0124	-0.9233 ± 0.0439	9.0573	1.5054 ± 0.2201
L2	0.4417 ± 0.0273	-0.6521 ± 0.0141	-0.6162 ± 0.0364	12.1661	1.4675 ± 0.2054
L1	0.6050 ± 0.0388	-0.7373 ± 0.0135	-0.3005 ± 0.0277	17.0540	1.4374 ± 0.1891

7.4 DISCUSSION

Even though this study was based on limited amount of data and included only a single patient, some interesting observations can be made regarding the function of the lumbar pad and how this is affected by the patient's posture.

First of all, the one dimensional evaluation showed that the higher interface pressure also yields a difference in average breathing cycle. While the relative increase in mean pressure magnitude was found to be similar in both positions, it was found that the variance between breathing cycles was higher in a seated position during inhalation and the (first) hold fase. Moreover, the results show that the theoretic ideal breathing cycle is better matched in a standing position than in a seated position, especially during inhalation. These results can possibly be explained by the fact that the higher brace pressure resulting from the seated position may obstruct respiratory movement to a higher degree, resulting in the patient having to put more effort into performing the box breathing exercise. While it is assumed that this does not affect the function of the brace directly, it illustrates how in a seated position the brace may potentially compromise the patient's respiratory movement more than in a standing position. However, further research is required in order to determine whether this may also affect the patient's quality of life (QOL) or the compliance to the brace treatment.

Second of all, it was illustrated with the three dimensional evaluation that the increase in pressure as a result of inhalation is not uniform in both positions. In the seated position however, it was found that this non-uniformity is more apparent throughout the entire breathing cycle, which was also quantified in Section 7.3.1 as a higher pressure pad variance (see Figure 7.8). In both positions, a local increase towards the upper left side of the lumbar pad can be observed, which is assumed to be related to the lower (left) part of the ribcage moving out during inhalation. A notable difference between

the two positions is the pressure point towards the lower left side of the pad that was observed for the seated position. This pressure point is presumably caused by the bony prominence of the iliac crest. Pressure points in general are to be avoided in orthotics as they can cause discomfort and can lead to skin problems. While it cannot be said that the brace may therefore cause more problems as a result of a seated position, it should be taken into account that the pressure is distributed differently and care should be taken to ensure that the pressure points are kept to a minimum in all positions.

Finally, it was found in the four dimensional evaluation discussed in 7.2.3 that the lumbar pad causes the highest equivalent bending moment over the L1 vertebra, which is the vertebra located at the apex of the (secondary) lumbar curve. As it is expected that this vertebra experiences the largest spinal bending moment of all lumbar vertebrae, an equally large equivalent bending moment is required to counteract this. The sagittal and lateral component of the equivalent bending moment over the L1 vertebra were found to be dominant, which implies that the lumbar pad seems to have a predominantly lordotic and lateral bending effect on that specific vertebra and the lumbar spine in general. In addition, the results seem to indicate that respiratory movement does not cause a significantly different effect as the relative components seem to increase proportionally for both positions. These results should however be interpreted carefully. The calculated equivalent bending moments represent the resulting moments around five fixed points in space in some local frame representing the orientation of the vertebra. Any intrinsic properties (spinal stiffness, bodymass, etc.) and the additional effect of the thoracic, pelvic and the axillary pad were not considered. While these findings seem to illustrate the function of the lumbar pad to some extent, additional data measured at the other pressure pads as well as a full corrected and uncorrected reconstruction of the spine is required in order to provide a meaningful evaluation of the function of the brace.

While this work has demonstrated the feasibility of a cost effective pressure monitoring system for evaluation of brace function, there are some limitations that should not be overlooked and should be taken into account in future research. Some recommendations can be given for each aspect of the design to give direction for further optimization.

Pressure Sensor Performance and Integration

First and foremost, it should be acknowledged that the FSR402 by Interlink Electronics was found to be unsuitable for long term monitoring purposes. While the sensor is cost effective and allows for simple implementation, it was found to be very sensitive to changes in actuation area. This required integration of the FSR in a surrounding structure that would ensure consistent actuation. This significantly increased the thickness of the sensor pad, which is assumed to inevitably have an effect on the measurement of brace-torso interface pressure. In addition to that, the results found regarding the accuracy of the FSRs provide only a limited and ideal perspective of the actual sensor performance. As discussed in 6.4, it is expected that the random error will be higher when tested using single load tests and while the hysteresis compensation algorithm seems promising, further research is required for its validation. The FSRs were also found to be significantly affected by external environmental factors and therefore required frequent calibration of each sensor individually, which is especially impractical for a system that should be robust enough to remain unaffected throughout the brace treatment. It is therefore recommended that the future studies focus on using either capacitive pressure sensors or thru mode piezoresistive pressure sensors. While being more expensive, they are also expected to be more stable than shunt mode piezoresistors as their terminals are assumed to deflect more predictably compared to the interdigitated terminals of the FSR. A sensor integration design as discussed in 4.3.2 may however still be required. It is recommended that stereolithography (SLA) 3D printing or injection molding is used for manufacturing the load plates, which would allow for more detail and therefore a more sophisticated and thinner integration design.

Electronic Hardware Design

Second of all, it should also be addressed that, while not being the focus of this research, the electronic hardware design resulted in a very bulky device, which leaves much room for optimization. The PCBs can be optimized using four or eight layers instead of the two layer design that was used for this prototype. A smaller microcontroller may also be chosen like the ESP8266, which also has an integrated WIFI-module. The most significant weight reduction may however be achieved by optimizing the power supply. The NiMH batteries were chosen for safety reasons to avoid the restrictions for medical devices that are posed for Lithium-ion equivalents [18]. However, accounting for almost 30% of the total weight (510g of 1800g total), measures can be taken to drastically reduce the weight.

Spatial Reconstruction Method

While having demonstrated the feasibility of a novel approach for reconstructing the spatial geometry of the spine and the sensor pad, it should be noted that this also requires more extensive validation for defining the accuracy of the reconstruction. The spacing of the points of the point grid defined on the torso surface is expected to have unequal spacing in the radial direction. This was minimized by taking a small step size of 1mm. However, this may however still cause distortion of the sensor pad geometry and thus also the relative locations projected locations of the FSRs. Measures should

therefore be taken to minimize this if necessary. Other reasons that may cause errors in the spatial reconstruction of the sensor pad is the relatively subjective nature of the interface that is used to place the pad at its digital equivalent location on the surface model. The lumbar pad was chosen to minimize this error as its placement is more universally placed in the same relative location than the other pads. However, measures should be taken that eliminate the subjectivity of the sensor pad reconstruction by identifying landmarks on the torso surface which could be used as reference.

Errors are also to be expected in the spinal reconstruction as a result of interpolation of vertebra geometry using male standard dimensions. Efforts should therefore be made to obtain appropriate standard vertebra dimensions for a more accurate reconstruction. It should also be noted that for a scoliotic spine these standard dimensions may not provide an accurate representation of reality. However, a large amount of radiographic data is available for scoliotic patients which could be used as a reference for a more accurate spinal reconstruction of scoliotic spines. Additionally, it should be noted that this method is also very susceptible to inaccurate landmark identification. However, previous research has demonstrated the feasibility of using deep-learning for accurate and automatic landmark identification on radiographic data [92], which may be used in this application for a more reliable reconstruction method. While this method may provide an alternative to standard methods, it is expected to be inferior to current imaging technology like the EOS system or other more invasive technology. However, when sufficiently optimized, this method may be a promising alternative when these systems are not available and may provide a reasonable estimate of the spinal geometry.

Validation Results

These limitations are also expected to have affected the validation test results, which should therefore be carefully interpreted. As mentioned in Chapter 6, it is expected that the higher body temperature will have had an effect on the sensor behavior, causing the measured pressure to be lower than the actual pressure. Additionally, it should be taken into account that the unknown accuracy of the reconstructed geometry cause the calculated equivalent bending moments to have an additional unknown error. These equivalent bending moments should therefore only be interpreted as a qualitative analysis, providing a rough estimate of the bending moments caused by the lumbar pad. Future research should simultaneously measure pressure at all relevant pressure areas in the brace and compare the in-brace spinal geometry with the out of brace spinal geometry for providing an accurate description of the function of the brace. Nevertheless, the mean pressure magnitude that was measured was found to be very similar to pressures found in other studies [27, 50, 52, 63, 86, 89, 90]. The mean pressure magnitude can be expected to have a higher accuracy than the other metrics as it combined the data from 15 individual FSRs, which is therefore expected to minimize the random error. However, one should keep in mind that the results found in this validation test were based on a single patient only and no definitive conclusions can therefore be drawn. Potential follow-up studies should therefore include a larger sample size and should measure data on multiple occasions. Finally, it is also advised that future research compares data from the prototype with measurements taken with a validated benchmark system with a known performance. Previous research has been found to be hard to compare as studies used different measurement systems and methods. A universal benchmark system and protocol should therefore greatly benefit brace research overall.

9 | CONCLUSION

This work has provided a complete and detailed strategy for the design of a cost effective brace pressure monitoring and functional evaluation system for giving patient and practitioner adequate feedback with the goal of optimizing scoliosis brace treatment. This was done by defining specific evaluation metrics that captured the different functional aspects of a scoliosis brace (1.)¹. These metrics were used in addition to results from previous research to define a set of requirements (2.) for the design of the electronic hardware of the prototype and a data-processing method for reconstructing the three dimensional spatial geometry of the lumbar spine and a lumbar sensor pad (3.). Testing with a repeatable actuation system showed a random error in the sensor output of approximately 4% and an estimated modelling error of -13.55% (4.). Finally, a validation test demonstrated the feasibility of the pressure monitoring and evaluation system by quantifying the evaluation metrics for a patient treated with a Cheneau-type scoliosis brace, which illustrated different aspects related to the function of the brace (5.).

¹ See the sub-objectives defined for this research in Section 1.5

BIBLIOGRAPHY

- [1] Aaro, S. and Ohlund, C. (1984). Scoliosis and pulmonary function. *Spine*, 9(2):220 – 222.
- [2] Ahmad, A., Abu Osman, N., Mokhtar, H., Mehmood, W., and Kadri, N. (2019). Analysis of the interface pressure exerted by the chèneau brace in patients with double-curve adolescent idiopathic scoliosis. *Proceedings of the Institution of Mechanical Engineers, Part H: Journal of Engineering in Medicine.*, 233(9):901–908.
- [3] Angelucci, A., Cavicchioli, M., Cintorrino, I. A., Lauricella, G., Rossi, C., Strati, S., and Aliverti, A. (2021). Smart textiles and sensorized garments for physiological monitoring: A review of available solutions and techniques. *Sensors.*, 21(3):814.
- [4] Antratek Embedded Electronics Media (2021). Flexiforce a201 sensor 100lbs. <https://www.antratek.nl/flexiforce-a201-sensor-100lbs>. Retrieved on 2021-5-6.
- [5] Antratek Embedded Electronics & Media (2021). Fsr-402 force sensing resistor 0.5". <https://www.antratek.nl/force-sensing-resistor-0-5>. Retrieved on 2021-5-6.
- [6] Arduino (2020). Arduino mega 2560 rev3 product reference manual. A000067.
- [7] Arduino (2021). Arduino Uno R3 Product Reference Manual. A000066.
- [8] Aubin, C., Labelle, H., Ruszkowski, A., Petit, Y., Gignac, D., Joncas, J., and Dansereau, J. (1999). Variability of strap tension in brace treatment for adolescent idiopathic scoliosis. *Spine*, 24(4):349–354.
- [9] Azofra-Monge, A. and I., A. A. (2020). Morphometric research and sex estimation of lumbar vertebrae in a contemporary spanish population. *Forensic Sci Med Pathol.*, 16(2):216–225.
- [10] Bavi, A. and Rouhi, G. (2020). The biomechanical performance of the night-time providence brace: experimental and finite element investigations. *Heliyon*, 6(10):e05210.
- [11] Capacitive Piezoresistive Pressure Sensors - Differences ES Systems. (2020). Standard sensors archives singletact. <https://esenssys.com/capacitive-piezoresistive-pressure-sensors-differences/>. Retrieved 2022-4-30.
- [12] Chalmers, E., Lou, E., Hill, D., and Zhao, H. (2021). An advanced compliance monitor for patients undergoing brace treatment for idiopathic scoliosis. *Medical Engineering & Physics*, 37(2):203–209.
- [13] Cheung, J., Cheung, P., Yeng, W. C., and Chan, L. (2020). Does curve regression occur during underarm bracing in patients with adolescent idiopathic scoliosis?. *Clinical Orthopaedics and Related Research*, 478(2):334–345.
- [14] Clin, J., Aubin, C., Parent, S., and Labelle, H. (2011). Biomechanical modeling of brace treatment of scoliosis: effects of gravitational loads. *Med Biol Eng Comput*, 49:743–753.
- [15] Clin, J., Aubin, C., Sangole, A., Labelle, H., and Parent, S. (2010). Correlation between immediate in-brace correction and biomechanical effectiveness of brace treatment in adolescent idiopathic scoliosis. *Spine*, 35(18):1706–1713.
- [16] Coley, B. (2013). *Caffey's Pediatric Diagnostic Imaging E-Book*. Elsevier Health Sciences., 12th edition. edition. 1428 - 1429. ISBN 978-1455753604.
- [17] Crijns, T., Stadhouder, A., and Smit, T. (2017). Restrained differential growth. *Spine*, 42(12):E726–E732.

- [18] CSA Group Testing & Certification Inc. (2021). Making Sense of Regulations for Medical Device Batteries. <https://www.csagroup.org/article/making-sense-regulations-medical-device-batteries/>. Retrieved on 25-6-2021.
- [19] De Jesus, K., Cheng, M., Jiang, L., and Bakhoun, E. (2015). Resolution enhancement method used for force sensing resistor array. *Journal of Sensors*, 2015(647427).
- [20] Dehzangi, O., Iftikhar, O., Bache, B., Shen, C., Wensman, J., and Li, Y. (2018). Force and activity monitoring system for scoliosis patients wearing back braces. *2018 IEEE International Conference on Consumer Electronics (ICCE)*, pages 1–4.
- [21] Emans, J., Hedequist, D., Miller, R., Cassella, M., Hresko, M., Karlin, L., Magin, M., Ryan, K., Hall, J., Miller, J., and McCarthy, C. (2003). Reference manual for the boston scoliosis brace. *Boston, MA: Boston Brace International, Inc.*
- [22] Eurocircuits (2022). Track Width Graphic. <https://www.eurocircuits.com/pcb-design-guidelines/track-width-graphic/>. Retrieved on 2021-5-15.
- [23] F., W. (2015). *Soft Tactile Sensors for Human-Machine Interaction*. In: Tao X. (eds) *Handbook of Smart Textiles*. Springer, Singapore.
- [24] Fan, Y., Ren, Q., To, M., and Cheung, J. (2020). Effectiveness of scoliosis-specific exercises for alleviating adolescent idiopathic scoliosis: a systematic review. *BMC Musculoskelet Disord*, 21(1):495.
- [25] Florez, J. and Velasquez, A. (2010). Calibration of force sensing resistors (fsr) for static and dynamic applications. *2010 IEEE ANDESCON*, pages 1–6. doi: 10.1109/ANDESCON.2010.5633120.
- [26] Fuss, F. K., Ahmad, A., Tan, A. M., Razman, R., and Weizman, Y. (2021). Pressure sensor system for customized scoliosis braces. *Sensors*, 21(4):1153.
- [27] Gesbert, J. C., Colobert, B., Rakotomanana, L., and Violas, P. (2020). Idiopathic scoliosis and brace treatment: an innovative device to assess corrective pressure. *Computer methods in biomechanics and biomedical engineering.*, 24(2):131–136.
- [28] Ghonasgi, K., Youssaf, S., Esmatloo, P., and Deshpande, A. (2021). A modular design for distributed measurement of human-robot interaction forces in wearable devices. *Sensors (Basel)*, 21(4):1–6.
- [29] Grivas, T., de Mauroy, J., Wood, G., Rigo, M., Hresko, M., Kotwizki, T., and Negrini, S. (2016). Brace classification study group (bcsg): part one - definitions and atlas. *Scoliosis and Spinal Disorders*, 11(43).
- [30] Harrington, D., Dowd, K., and Bourke, A. (2011). Cross-sectional analysis of levels and patterns of objectively measured sedentary time in adolescent females. *Int J Behav Nutr Phys*, 8(120).
- [31] Harris, L. and Oliver, M. (2014). Design and Fabrication of a Piezoresistive Tactile Sensor for Ergonomic Analyses. <https://www.researchgate.net/publication/311665970Design-and-Fabrication-of-a-Piezoresistive-Tactile-Sensor-for-Ergonomic-Analyses>. Retrieved on 2021-8-21.
- [32] Hefti, F. (2013). Pathogenesis and biomechanics of adolescent idiopathic scoliosis (ais). *Journal of children's orthopaedics.*, 7(1):17–24.
- [33] Honeywell International Inc. (2003). Pressure sensors FS01/FS03 Force Sensors FS Series. 008092-1-EN.
- [34] Hu, X., Zhao, J., Peng, D., Sun, Z., and Qu, X. (2020). Estimation of foot plantar center of pressure trajectories with low-cost instrumented insoles using an individual-specific nonlinear model. *Sensors (Basel)*, 18(2).

- [35] Huh, S., Eun, L. Y., Kim, N. K., Jung, J. W., Choi, J. Y., and Kim, H. S. (2015). Cardiopulmonary function and scoliosis severity in idiopathic scoliosis children. *Korean journal of pediatrics.*, 58(6):218–223.
- [36] Illés, T. S., Lavaste, F., and Dubousset, J. F. (2019). The third dimension of scoliosis: The forgotten axial plane. *Orthopaedics traumatology, surgery research : OTSR*, 105(2):351–359.
- [37] Interlink Electronics Inc. (2002). Fsr® force sensing resistors® integration guide and evaluation parts catalog. 90-45632 Rev. D.
- [38] JST (2022). JST Catalogue Vol. 120e. <https://www.jst.fr/doc/jst/pdf/jst-connector-catalogue-vol-120e.pdf>. Retrieved on 2022-7-2.
- [39] Kamal, Z., Rouhi, G., Arjmand, N., and Adeeb, S. (2019). A stability-based model of a growing spine with adolescent idiopathic scoliosis: A combination of musculoskeletal and finite element approaches. *Med Eng Phys.*, 64:46–55.
- [40] Katz, D., Herring, J., Browne, R., Kelly, D., and Birch, J. (2010). Brace wear control of curve progression in adolescent idiopathic scoliosis. *The Journal of Bone and Joint Surgery. American Volume*, 92(6):1343–1352.
- [41] Kokai, O., Kilbreath, S., McLaughlin, P., and Dylke, E. (2021). The accuracy and precision of interface pressure measuring devices: A systematic review. *Phlebology.*, 36(9):678–694.
- [42] Kotwicki, T. and Cheneau, J. (2008). Biomechanical action of a corrective brace on thoracic idiopathic scoliosis: Cheneau 2000 orthosis. *Disability and Rehabilitation: Assistive Technology*, 3(3):146–153.
- [43] Lam, B., Stomberg, N., and Laovoravit, T. (20017). Magneforce: Validation of a modular tri-axial force sensor for gait analysis.
- [44] Landauer, F., Wimmer, C., and Behensky, H. (2003). Estimating the final outcome of brace treatment for idiopathic thoracic scoliosis at 6-month follow-up. *Pediatric Rehabilitation*, 6(3-4):201–207.
- [45] Leis, J. (2011). *Digital Signal Processing Using MATLAB for Students and Researchers*. Wiley., hoboken, new-jersey edition. ISBN 9780470880913.
- [46] Li, M., Wong, M., Luk, K., Wong, K., and Cheung, K. (2014). Time-dependent response of scoliotic curvature to orthotic intervention: when should a radiograph be obtained after putting on or taking off a spinal orthosis? *Spine*, 39(17):1408–1416.
- [47] Liu, C., Huang, N., Xu, F., Tong, J., Chen, Z., Gui, X., Fu, Y., and Lao, C. (2018). 3d printing technologies for flexible tactile sensors toward wearable electronics and electronic skin. *Polymers*, 1(6):629.
- [48] Lou, E., Chan, C., Raso, V., Hill, D., Moreau, M., Mahood, J., and Donauer, A. (2005). A smart orthosis for the treatment of scoliosis. *2005 IEEE Engineering in Medicine and Biology 27th Annual Conference*, pages 1008–1011.
- [49] Lou, E., Hill, D., Hedden, D., Mahood, J., Moreau, M., and Raso, J. (2011). An objective measurement of brace usage for the treatment of adolescent idiopathic scoliosis. *Medical Engineering & Physics*, 33(3):290–294.
- [50] Lou, E., Raso, J., Hill, D., Mahood, J., and M.J., M. (2004). Correlation between quantity and quality of orthosis wear and treatment outcomes in adolescent idiopathic scoliosis. *Prosthetics and Orthotics International.*, 28(1):49–54.
- [51] Loyola University of Chicago Health Sciences Division (2022). Radiological Anatomy of Bones for Non Radiologists. <http://www.meddean.luc.edu/lumen/meded/radio/curriculum/Bones/Bone-anatomy-f.htm>. Retrieved on 2022-5-21.

- [52] Mac-Thiong, J., Petit, Y., Aubin, C., Delorme, S., Dansereau, J., and Labelle, H. (2003). Biomechanical evaluation of the boston brace system for the treatment of adolescent idiopathic scoliosis. *Spine*, 29(1):26–32.
- [53] Mahboub-Ahari, A. (2016). Eos imaging versus current radiography: A health technology assessment study. *Med J Islam Repub Iran*, 30:331.
- [54] Mayo Clinic (2021). Scoliosis. <https://www.mayoclinic.org/diseases-conditions/scoliosis/symptoms-causes/syc-20350716>. Retrieved on 2021-9-21.
- [55] Michigan Medicine - University of Michigan (2018). Morphomics - Reference Analytic Morphomic Population (RAMP). <https://www.med.umich.edu/surgery/morphomics/ramp.html>. Retrieved on 2022-4-2.
- [56] Microchip Technology Inc. (2013). Mcp6001/2/4 1 mhz bandwidth low power op amp. DS21733D.
- [57] Muzaffar, S. and Elfadel, I. (2020). Shoe-integrated, force sensor design for continuous body weight monitoring. *Sensors (Basel)*, 20(12).
- [58] National Aeronautics and Space Administration (NASA) (2022). Center of Pressure - cp. <https://www.grc.nasa.gov/www/k-12/airplane/cp.html>. Retrieved on 2022-6-6.
- [59] Nissan, M. and Gilad, I. (1984). The cervical and lumbar vertebrae - an anthropometric model. *Eng Med.*, 13(3):111–4.
- [60] Novel.de (2022). Pedar- footwear pressure distribution measurement — novel.de. <https://www.novel.de/products/pedar/>. Retrieved on 2022-1-27.
- [61] O'Neill, P. J., Karol, L. A., Shindle, M. K., Elerson, E. E., and BrintzenhofeSzoc, K. M. (2005). Decreased orthotic effectiveness in overweight patients with adolescent idiopathic scoliosis. *J Bone Joint Surg Am.*, 87(5):1069–74.
- [62] Onishi, F., de Paiva Neto, M., Cavalheiro, S., and Silva Centeno, R. (2019). Morphometric analysis of 900 lumbar intervertebral discs: Anterior and posterior height analysis and their ratio. *Interdisciplinary Neurosurgery.*, 18:100523.
- [63] Pham, V., Houilliez, A., Schill, A., Carpentier, A., Herbeaux, B., and Thevenon, A. (2008). Study of the pressures applied by a cheneau brace for correction of adolescent idiopathic scoliosis. *Prosthetics and Orthotics International*, 32(2):345–335.
- [64] Rahman, T., Bowen, J. R., Takemitsu, M., and Scott, C. (2005). The association between brace compliance and outcome for patients with idiopathic scoliosis. *Journal of pediatric orthopedics*, 25(4):420–422.
- [65] Rigo, M. and Jelacic, M. (2017). Brace technology thematic series: the 3d rigo chèneau-type brace. *Scoliosis and Spinal Disorders*, 12(10).
- [66] Rigo, M. and Weiss, H. (2008). The chèneau concept of bracing- biomechanical aspects. *Studies in Health Technology and Informatics*, 135:303–319.
- [67] RS Pro (2021a). RS PRO 3.6V 4Ah NiCd Emergency Lighting Battery Pack. RS Stock number 2042757.
- [68] RS Pro (2021b). RS PRO 7.2V NiMH Rechargeable Battery Pack 2Ah. RS Stock number 777-0406.
- [69] Savlovskis, J and Raits, K (2021). Anatomy Standard — Typical Lumbar Vertebra. <https://www.anatomystandard.com/Columna-Vertebris/Vertebrae-Lumbales/Typical-Lumbar.html>. Retrieved on 2022-5-27.
- [70] Schoepp, K., Dawson, M., Schofield, J., Carey, J., and Hebert, J. (2018). Design and integration of an inexpensive wearable mechanotactile feedback system for myoelectric prostheses. *IEEE J Transl Eng Health Med*, 6.

- [71] Schofield, J., Evans, K., Hebert, J., and Marasco, P.D. Carey, J. (2016). The effect of biomechanical variables on force sensitive resistor error: Implications for calibration and improved accuracy. *J Biomech.*, 49(5):786–792.
- [72] Sensitronics LLC (2022). FSR 101 - Force Sensing Resistor Theory and Applications. <https://www.sensitronics.com/pdf/Sensitronics-FSR-101.pdf>. Revision 1.01.
- [73] Silicones and More (2021). Silicone Softflex 00-35. <https://www.siliconesandmore.com/nl/>. Retrieved on 2022-7-2.
- [74] SingleTact Miniature Force Sensors Ultra Thin (2021). Standard sensors archives singletact. <https://www.singletact.com/micro-force-sensors/standard-sensors/>. Retrieved on 2021-5-6.
- [75] Smit, T. (2020). Adolescent idiopathic scoliosis: The mechanobiology of differential growth. *JOR spine*, 3(4):e11115.
- [76] Swanson, E., Weathersby, E., Cagle, J., and Sanders, J. (2018). Evaluation of force sensing resistors for the measurement of interface pressures in lower limb prosthetics. *J Biomech Eng*, 141(10).
- [77] (SWCI), S. W. S. I. (2021). Mild scoliosis. <https://scoliosisinstitute.com/mild-scoliosis/>. Retrieved on 2021-9-21.
- [78] Tekscan (2021). Flexiforce standard model a201. DS Rev C 080717.
- [79] Tekscan (2021). I-scan product selection guide. <https://www.tekscan.com/resources/product-guide/i-scan-product-selection-guide>. Retrieved on 2021-11-24.
- [80] Tekscan Inc. (2017). How does a force sensitive resistor (FSR) work? <https://www.tekscan.com/blog/flexiforce/how-does-force-sensing-resistor-fsr-work>. Retrieved on 2022-1-26.
- [81] Texas Instruments (2003). High Speed CMOS Logic 16 Channel Analog Multiplexer/Demultiplexer. SCHS209C.
- [82] Texas Instruments (2017). LM78M05-MIL Series 3-Terminal 500-mA Positive Voltage Regulator. SNVSAX6.
- [83] Texas Instruments (2020). LM317 3-Terminal Adjustable Regulator. SLVSo44Y.
- [84] Thompson, R., Hubbard, E., Jo, C., Virostek, D., and Karol, L. (2017). Brace success is related to curve type in patients with adolescent idiopathic scoliosis. *J Bone Joint Surg Am.*, 99(11):923–928.
- [85] Trobisch, P., Suess, O., and Schwab, F. (2010). Idiopathic scoliosis. *Deutsches Arzteblatt international.*, 107(49):875–884.
- [86] van den Hout, J., van Rhijn, L., van den Munckhof, R., and van Ooy, A. (2002). Interface corrective force measurements in boston brace treatment. *Eur Spine J*, 11(4):332–335.
- [87] Wang, K., Muralidharan, J., Cuasay, S., Pruthi, S., and Kesavadas, T. (2021). An augmented reality application for clinical breast examination training. *2021 IEEE International Conference on Artificial Intelligence and Virtual Reality (AIVR)*, pages 224–227.
- [88] Weinstein, S., Dolan, L., Wright, J., and Dobbs, M. (2013). Effects of bracing in adolescents with idiopathic scoliosis. *The New England journal of medicine*, 369(16):1512 – 1521.
- [89] Wong, M. and Evans, J. (1998). Biomechanical evaluation of the milwaukee brace. *Prosthetics and Orthotics International*, 22:54–67.
- [90] Wong, M., Mak, A., Luk, K., Evans, J., and Brown, B. (2000). Effectiveness and biomechanics of spinal orthoses in the treatment of adolescent idiopathic scoliosis (ais). *Prosthetics and Orthotics International*, 24:148–162.

- [91] Wood, G. and Rigo, M. (2017). The principles and biomechanics of the rigo chèneau type brace. *InTechOpen*. <http://dx.doi.org/10.5772/intechopen.70381>.
- [92] Yeh, Y., Weng, C., Huang, Y., Fu, C., Tsai, T., and Yeh, C. (2021). Deep learning approach for automatic landmark detection and alignment analysis in whole-spine lateral radiographs. *Sci Rep*, 11(7618).
- [93] Zaina, F., de Mauroy, J., Grivas, T., Hresko, M., Kotwizki, T., Maruyama, T., Price, N., Rigo, M., Stikeleather, L., Wynne, J., and Negrini, S. (2014). Bracing for scoliosis in 2014: state of the art. *European Journal of Physical and Rehabilitation Medicine*, 50(1):93 – 110.
- [94] Zhang, C., Gou, X., and Xiao, R. (2021). Hysteresis in glass microsphere filled elastomers under cyclic loading. *Polymer Testing*, 95(107081). ISSN 0142-9418.
- [95] Zhu, C., Wu, Q., Xiao, B., Wang, J., Luo, C., Yu, Q., Liu, L., and Song, Y. (2021). A compliance real-time monitoring system for the management of the brace usage in adolescent idiopathic scoliosis patients: a pilot study. *BMC Musculoskeletal Disorders*, 22(1):152.

A | ACTUATION SYSTEMS

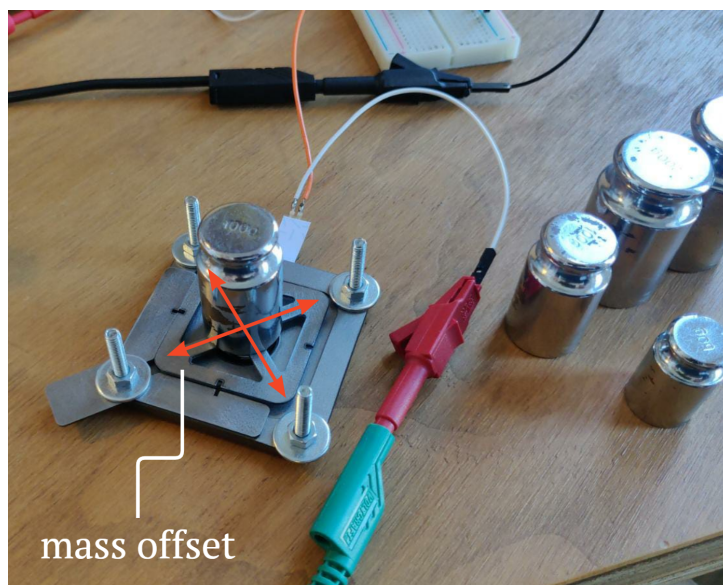


Figure A.1: The first actuation system that was used during preliminary testing.

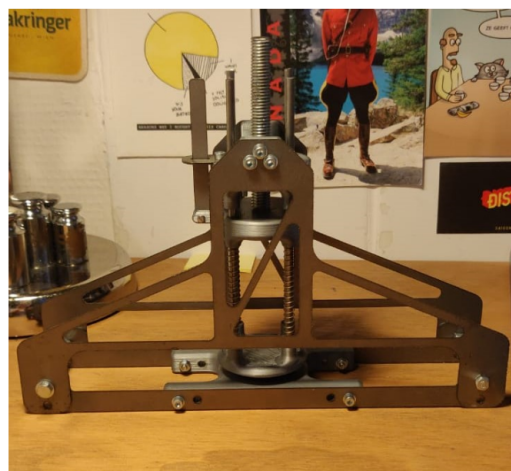
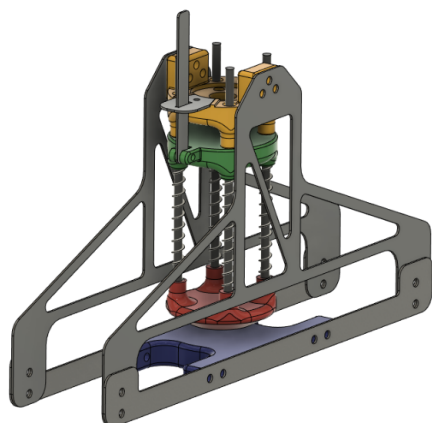


Figure A.2: The second actuation system that was tested consisted of a total four platforms where the middle two platform allowed for free linear vertical motion and were connected with springs (with a known linear spring constant). Moving the second platform downwards would cause compression of the springs, causing a force onto the bottom platform. The system was found to have too much friction in the linear guidance, making it unreliable and was therefore not used during this research

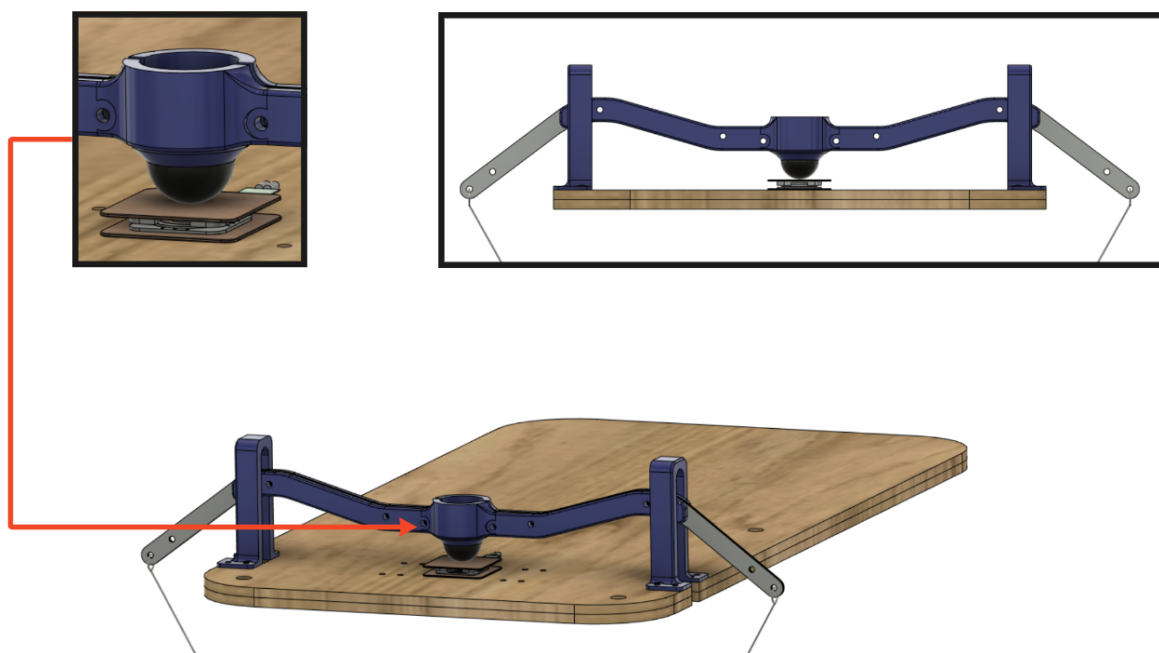
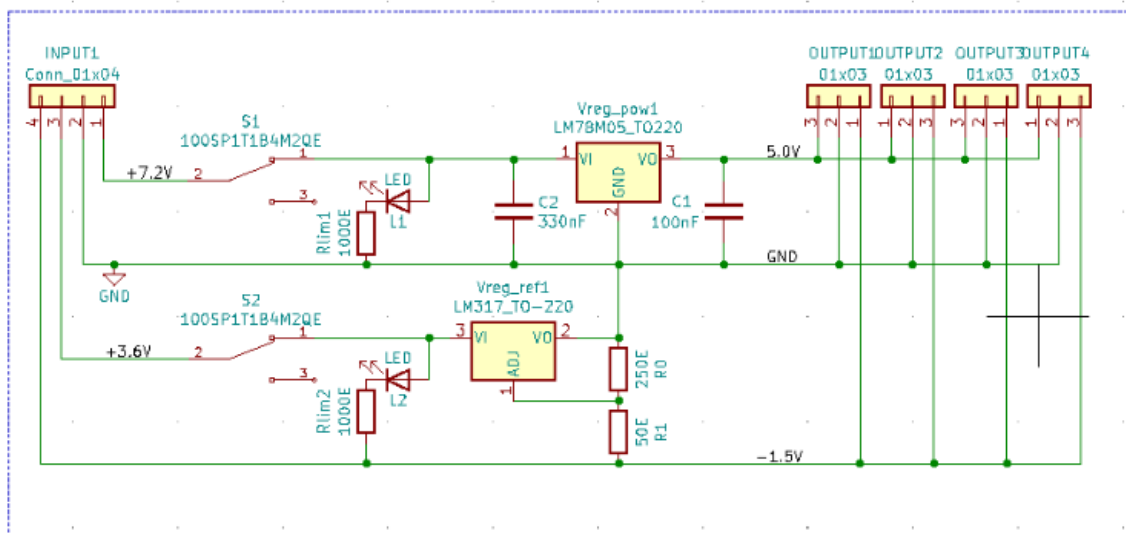


Figure A.3: This actuation system was eventually found to be most suitable for actuation of the sensors. The yoke has a total width of 344mm and when loaded has a center of gravity that is located below the rubber knob. The total mass of the yoke is 114g .

B | PCB ROUTING DESIGN AND CIRCUIT SCHEMATICS

Voltage Regulator Circuit



Data Transfer Circuit

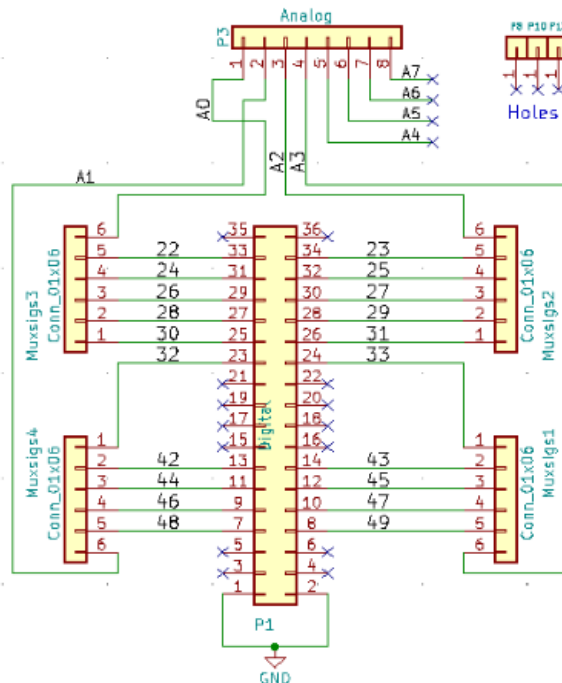


Figure B.1: Voltage Regulator and Data-Transfer Circuit.

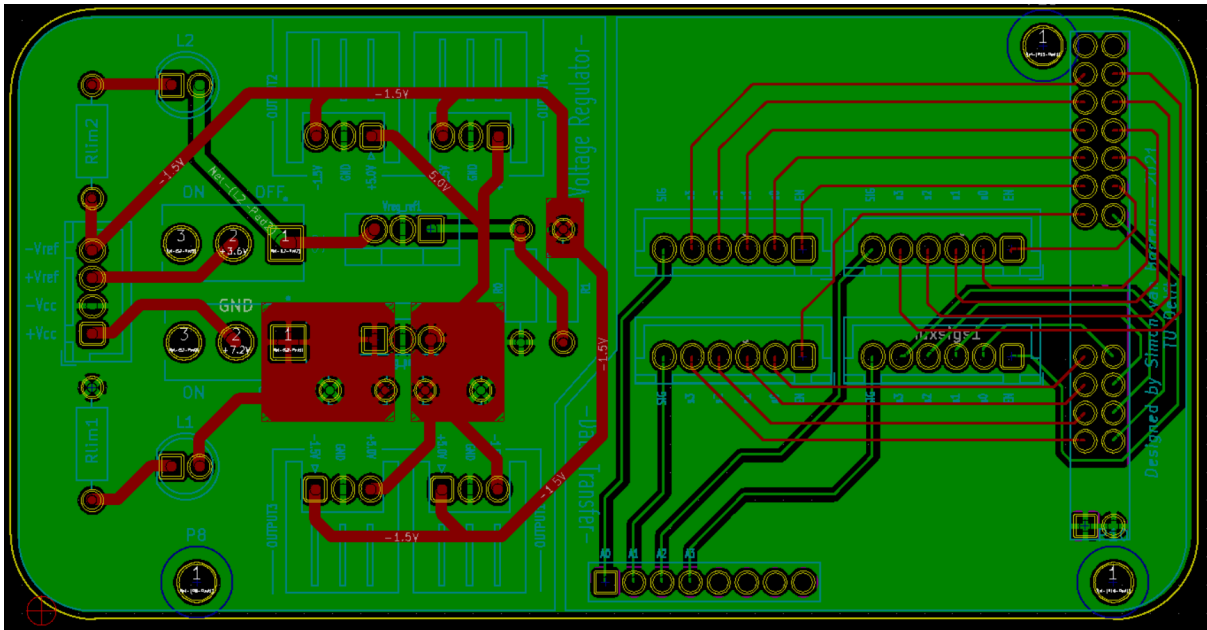


Figure B.2: Routing of the Voltage Regulator and Data-Transfer Circuit Circuit Board.

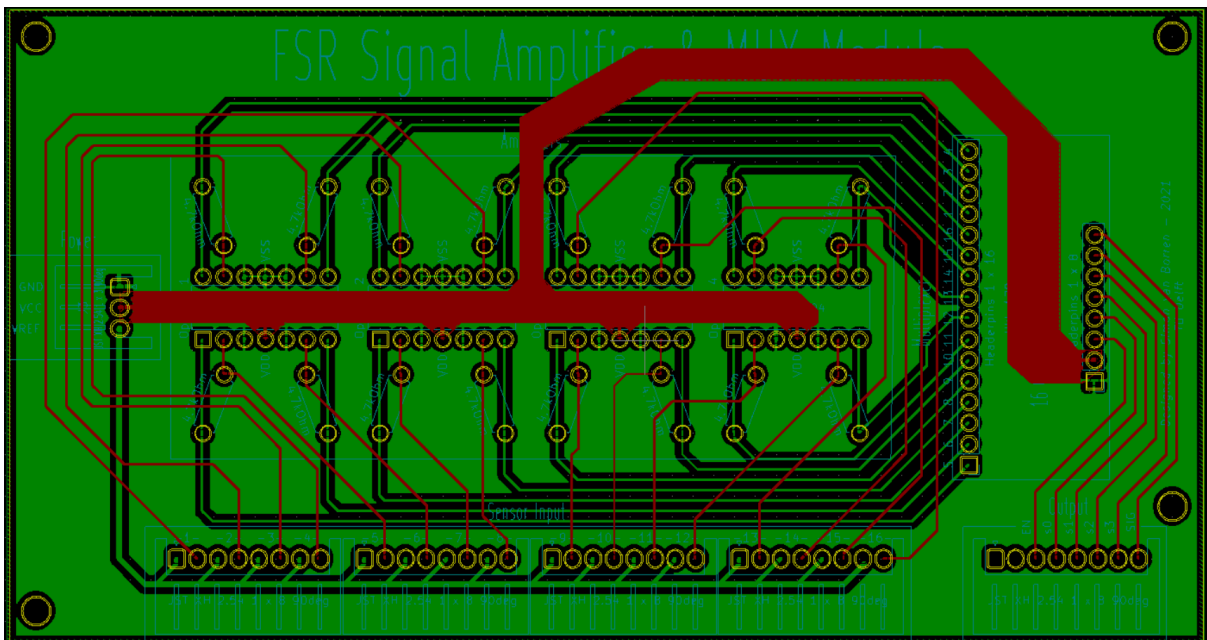


Figure B.3: Routing of the Signal Conditioning Module circuitboard

C | GRASSHOPPER SCRIPT

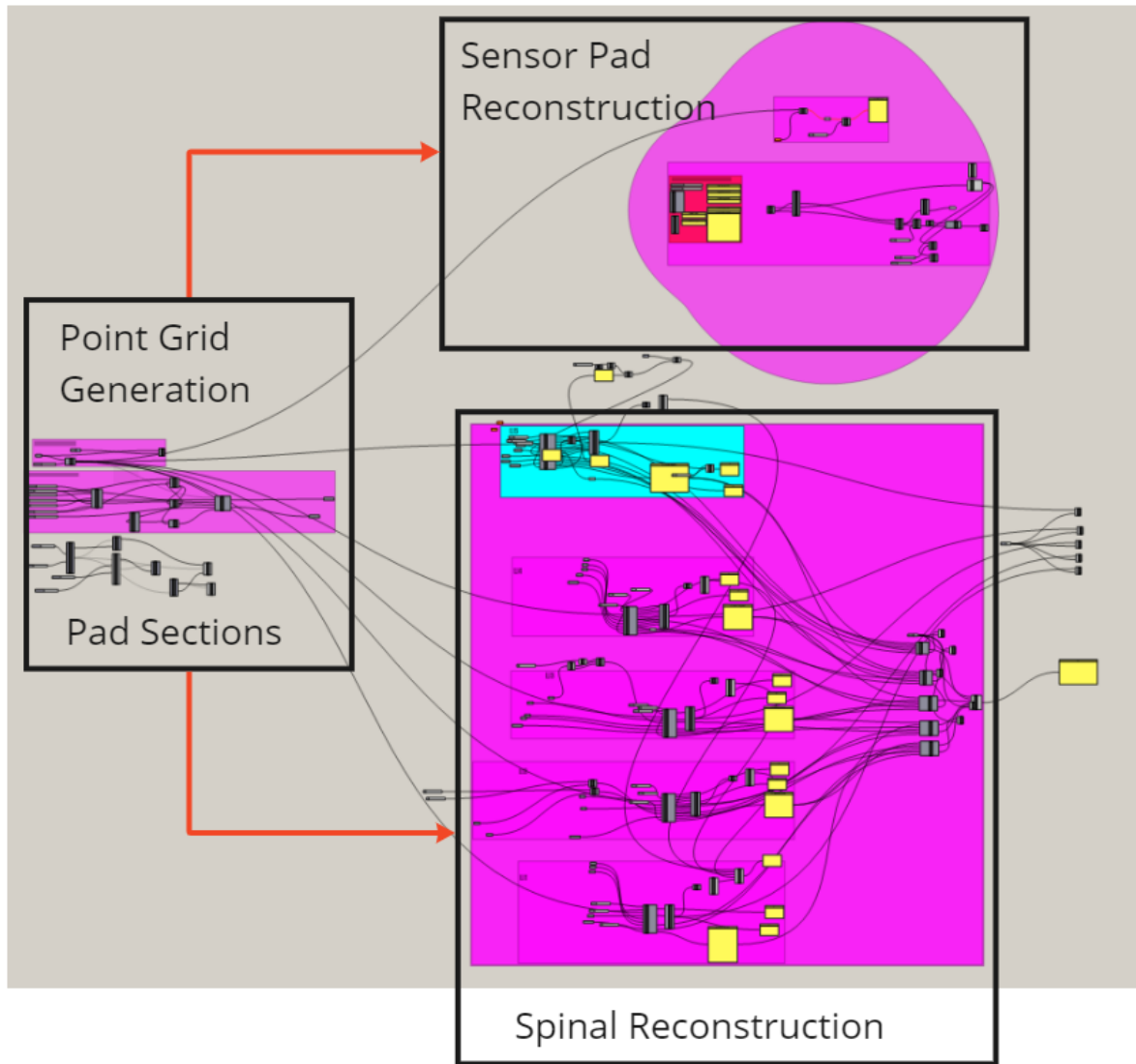


Figure C.1: Quick overview of the entire Grasshopper script used for reconstruction of the sensor pad and the lumbar spine.

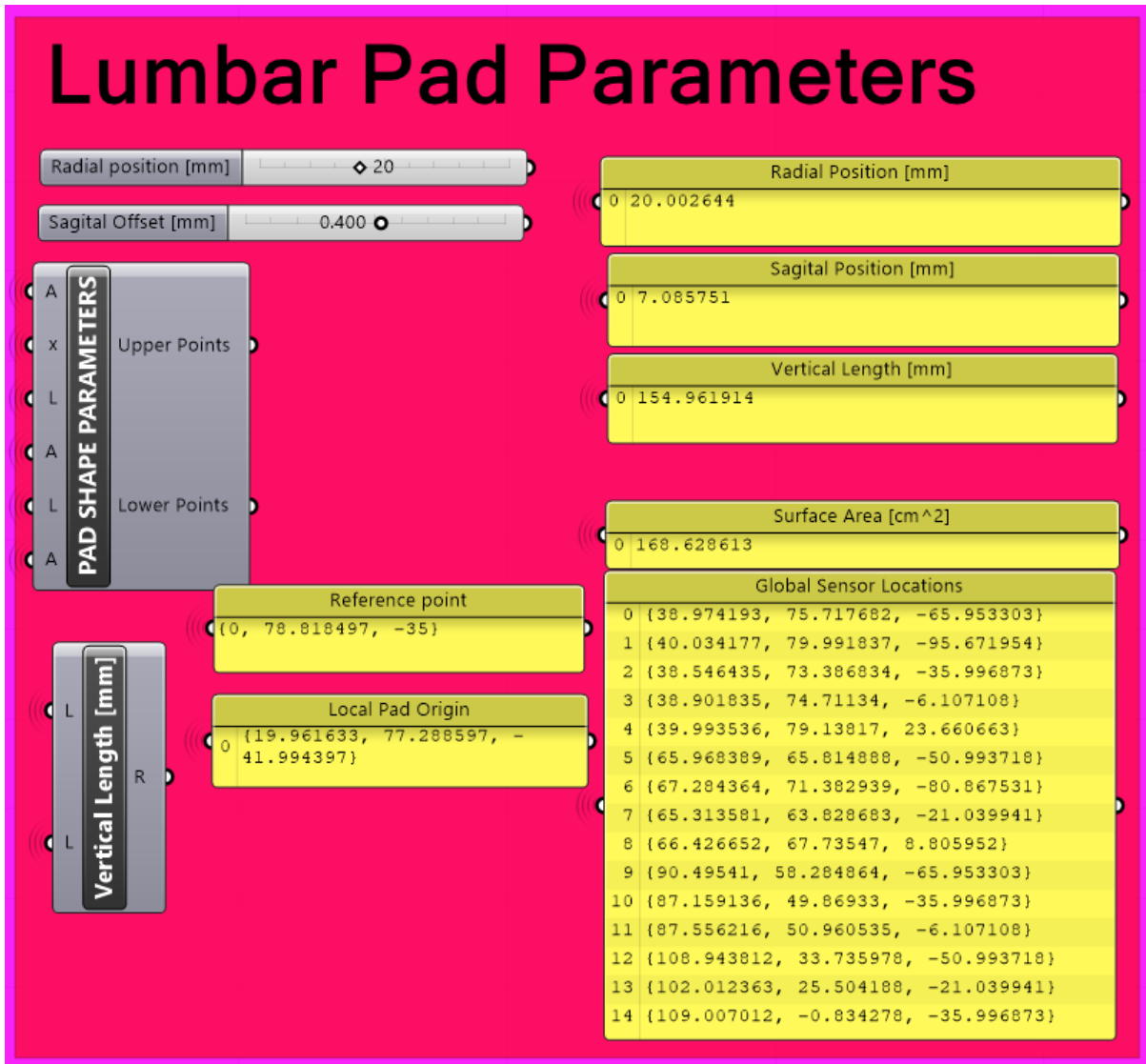


Figure C.2: Example of the interface built in Grasshopper for moving the lumbar pad to its required radial and vertical position with the main output being the global sensor locations.

D | CALIBRATION PROTOCOL

All of the 15 force sensitive resistors (FSR) in the sensor pad had to be calibrated individually prior to testing for obtaining the parameters for defining the major loading and deloading curves. This was done using the following protocol:

1. First the $10k\Omega$ variable resistors are tuned to approximately $5k\Omega$ (see Figure D.1).
2. Then, a total of two load-deload tests were performed for actuation of the FSR as defined in Chapter 6.
3. The maximum load of $1316g$ ($\sim 25.98kPa$, see Chapter 6) is then applied for a total of 15 seconds. If this remains below $4.5V$ (~ 920 bit) the resistance value is increased until the output signal is approximately $4.5V$, else the resistance value is kept constant.
4. This is then followed by a total of 3 load-deload tests as defined in Step 2. The data that follows is then used to compute the relevant parameters for the major load and deload curves

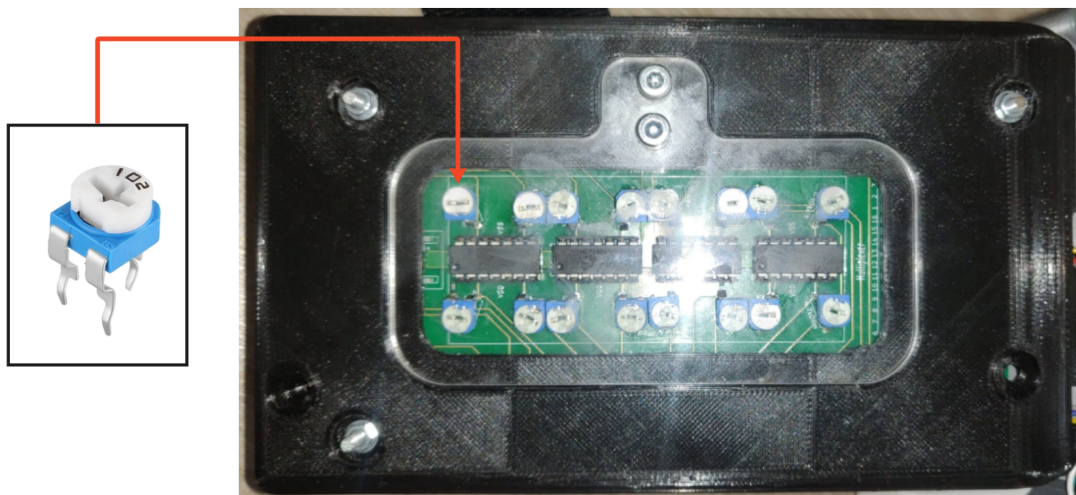


Figure D.1: A Figure showing the $10k\Omega$ variable resistors mounted on the signal conditioning module circuit board. The housing was adjusted to accommodate for the variable resistors and to allow the system to be easily calibrated by removing the plexiglas sheet mounted on the top.

E

ARDUINO & MATLAB CODE FOR DATA ACQUISITION

For initiating the pressure measurement data acquisition the following code is uploaded to the micro-controller:

```
mux_control_file $  
  
//The mux signal is read on analog pin A3:  
int FSR[] = {3,3,3,3,3,3,3,3,3,3,3,3,3,3,3,3};  
//int FSR1 = 30;  
//int FSR2 = 31;  
//int FSR3 = 32;  
//int FSR4 = 33;  
int sensPin = A3;  
  
// Switching code, Port Manipulation.  
// Every second bit is one of the 4 bit required to control the MUX  
byte controlPins[] = {B00000000, //0  
B01000000,  
B00010000,  
B01010000,  
B00000100, //7  
B01000100, //6  
B00010100, //5  
B01010100, //4  
B00000001, //8  
B01000001, //9  
B00010001, //10  
B01010001, //11  
B00000101,  
B01000101,  
B00010101  
};  
  
byte EnablePins[] = {B00000000,  
B00000000,  
B00000000,  
B00000000,  
B00000000,  
B00000000,  
B00000000,  
B00000000,  
B00000000,  
B00000000,  
B00000000,  
B00000000,  
B00000000,  
B00000000,  
B00000000,  
B00000000,  
B00000000,  
B00000000};
```

Figure E.1: Arduino Code pt. 1

```

void setPin(int outputPin)
// function to select pin on 74HC4067
{
  PORTL = controlPins[outputPin];
  PORTC = EnablePins[outputPin];
}

void setup() {
  Serial.begin(9600);
  DDRL = B11111111;
  DDRC = B11111111;
  pinMode(sensPin, INPUT);
}

void displayData()
// dumps captured data from array to serial monitor
{
  for (uint16_t i = 0; i < 15; i++)
  {
    if (i!=0)
    {
      Serial.print(", ");
    }
    Serial.print(FSR[i]);
  }
  Serial.println(" ");
}

void loop() {
  displayData();
  const uint32_t SAMPLE_PD = 3; // ms; period (how often to take a new sample)
  static uint32_t tStart = millis(); // ms; start time
  bool bufferIsFull = false; // set to true each time NUM_READINGS have been taken

  // Only take a reading once per SAMPLE_PD
  uint32_t tNow = millis(); // ms; time now

  for (int i = 0; i<15; i++){

    setPin(i);
    if (tNow - tStart >= SAMPLE_PD)
    {
      tStart += SAMPLE_PD;

      FSR[i] = analogRead(sensPin);
      //Serial.println(FSR[i]);
    }
  }
}

```

Figure E.2: Arduino Code pt. 2

When the Arduino Code is successfully uploaded to the microcontroller board, the following MATLAB function file is called to read the serial port input. The input of the function file includes the serial port number (COM) and the name of the Excel file the data should be saved as (should be of the form 'name.xls').

```

1  function T = callbackSerial(com, filename)
2  global T
3  %Delete residual port
4  delete(instrfindall);
5  %Define serial port.
6  s = serial(com,'baudrate',9600);
7  %Set size of buffer
8  s.InputBufferSize = 1024;
9  if (s.status == 'closed')
10
11      fopen(s);
12      figure('Name','TestData','NumberTitle','off');
13      fig = gcf;
14      grid on;
15
16      %% animatedlines
17      h1 = animatedline;
18      h2 = animatedline;
19      h3 = animatedline;
20      h4 = animatedline;
21      h5 = animatedline;
22      h6 = animatedline;
23      h7 = animatedline;
24      h8 = animatedline;
25      h9 = animatedline;
26      h10 = animatedline;
27      h11 = animatedline;
28      h12 = animatedline;
29      h13 = animatedline;
30      h14 = animatedline;
31      h15 = animatedline;
32      set(h1,'Color','k','MaximumNumPoints',200000000,'DisplayName','s1');
33      set(h2,'Color','k','MaximumNumPoints',200000000,'DisplayName','s2');
34      set(h3,'Color','r','MaximumNumPoints',200000000,'DisplayName','s3');
35      set(h4,'Color','r','MaximumNumPoints',200000000,'DisplayName','s4');
36      set(h5,'Color','k','MaximumNumPoints',200000000,'DisplayName','s5');
37      set(h6,'Color','r','MaximumNumPoints',200000000,'DisplayName','s6');
38      set(h7,'Color','k','MaximumNumPoints',200000000,'DisplayName','s7');
39      set(h8,'Color','b','MaximumNumPoints',200000000,'DisplayName','s8');
40      set(h9,'Color','m','MaximumNumPoints',200000000,'DisplayName','s9');
41      set(h10,'Color','g','MaximumNumPoints',200000000,'DisplayName','s10');
42      set(h11,'Color','m','MaximumNumPoints',200000000,'DisplayName','s11');
43      set(h12,'Color','b','MaximumNumPoints',200000000,'DisplayName','s12');
44      set(h13,'Color','b','MaximumNumPoints',200000000,'DisplayName','s13');
45      set(h14,'Color','r','MaximumNumPoints',200000000,'DisplayName','s14');
46      set(h15,'Color','r','MaximumNumPoints',200000000,'DisplayName','s15');
47
48      %% global variables
49      global A;
50      global i;

```

Figure E.3: MATLAB code pt. 1

```

50 -     global i;
51 -     global k;
52 -     global numitr;
53 -     global y;
54 -     global Y;
55 -     global T;
56 -     global t0;
57
58 -     A = zeros(1,15);
59 -     xlswrite(filename,A);
60 -     A = zeros(200,15);
61 -     Y = zeros(3000,1);
62 -     numitr = 1;
63 -     t0 = 0;
64 -     i=1;
65 -     y = 0;
66
67 -     t0 = now();
68 -     s.BytesAvailableFcn = {@Call, fig, h1, h2, h3, h4, h5, h6, h7, h8,
69 -         h9, h10, h11, h12, h13, h14, h15, filename} ;
70
71 - end
72
73 - %     fclose(s)
74 - %     delete(s)
75 - %     clear s
76 - end
77
78 - function T = Call(obj, ~, fig, h1, h2, h3, h4, h5, h6, h7, h8, h9, h10, h11, h12, h13, h14, h15, filename)
79
80 - global t0
81 - global numitr;
82 - global i;
83 - global A;
84 - global y;
85 - global Y;
86 - global T;
87
88 - if ishghandle(fig)==1
89
90 -     N = fscanf(obj);
91 -     N = convertCharsToStrings(N);
92 -     pat = digitsPattern(1,4) + ", " + digitsPattern(1,4) + ", " + digitsPattern(1,4) + ", "
93 -     + digitsPattern(1,4) + ", " + digitsPattern(1,4) + ", " + digitsPattern(1,4) + ", " + digitsPattern(1,4) + ", "
94 -     + digitsPattern(1,4) + ", " + digitsPattern(1,4) + ", " + digitsPattern(1,4) + ", " + digitsPattern(1,4) + ", "
95 -     + digitsPattern(1,4) + ", " + digitsPattern(1,4) + ", " + digitsPattern(1,4) + ", " + digitsPattern(1,4);
96 -     N = extract(N, pat);
97 -     N = str2num(N);
98
99 -     b = numitr;
100 -     H = [h1, h2, h3, h4, h5, h6, h7, h8, h9, h10, h11, h12, h13, h14, h15];

```

Figure E.4: MATLAB code pt. 2


```

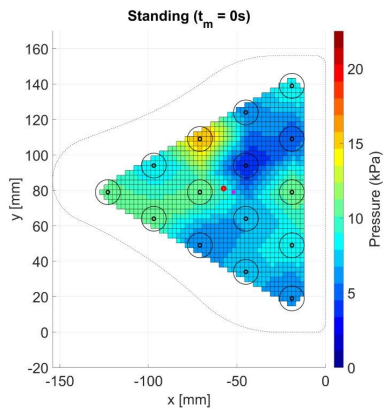
104 %         break % stop trying to add points
105 %     end
106
107 -     addpoints(H(1),b,N(1));
108 -     addpoints(H(2),b,N(2));
109 -     addpoints(H(3),b,N(3));
110 -     addpoints(H(4),b,N(4));
111 -     addpoints(H(5),b,N(5));
112 -     addpoints(H(6),b,N(6));
113 -     addpoints(H(7),b,N(7));
114 -     addpoints(H(8),b,N(8));
115 -     addpoints(H(9),b,N(9));
116 -     addpoints(H(10),b,N(10));
117 -     addpoints(H(11),b,N(11));
118 -     addpoints(H(12),b,N(12));
119 -     addpoints(H(13),b,N(13));
120 -     addpoints(H(14),b,N(14));
121 -     addpoints(H(15),b,N(15));
122 -     else
123 -         return;
124 -     end
125
126 -     n = i;
127 -     A(b,:) = N(1:15);
128 -     p = A;
129 -     %%
130
131 -     %p(b,:) = a0*A(b,:)+b0
132 -     %%
133 -     % sliding window -->
134 -     numitr = numitr + 1;
135 -     axis([numitr-100,numitr,0,1200]);
136 -     drawnow limitrate;
137 -     %n = n+1;
138 -     i = n;
139
140 - else
141 -     fclose(obj);
142 -     y = now();
143 -     T = (y - t0)*24*60*60;
144 -     T2 = T.*ones(1, 15);
145 -     A = [A;T2];
146 -     xlswrite(filename,A)
147
148 -     disp('xls file created');
149 -     %fclose(s);
150
151
152 - end
153
154 - end

```

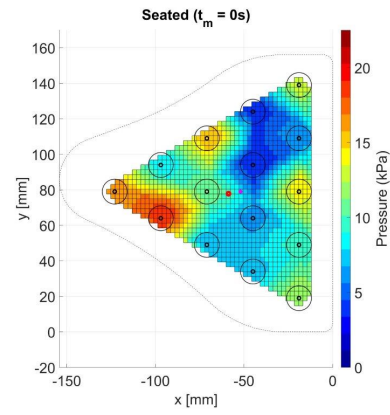
Figure E.5: MATLAB code pt. 3

F

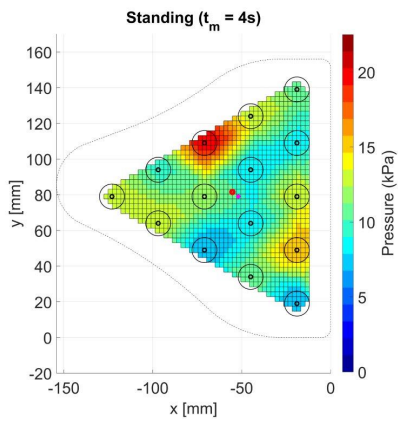
AVERAGE BREATHING CYCLE PRESSURE DISTRIBUTIONS



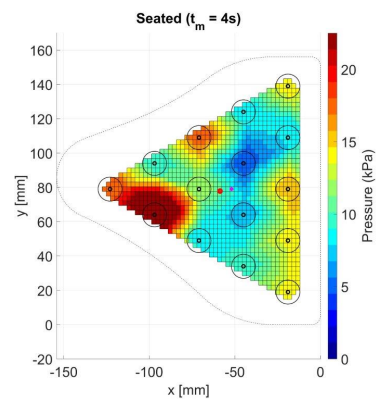
(a)



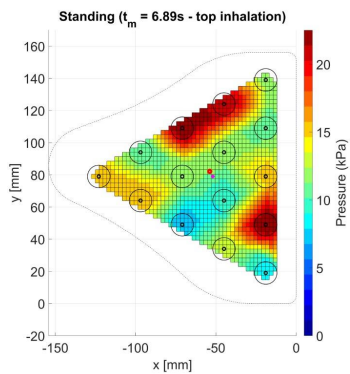
(b)



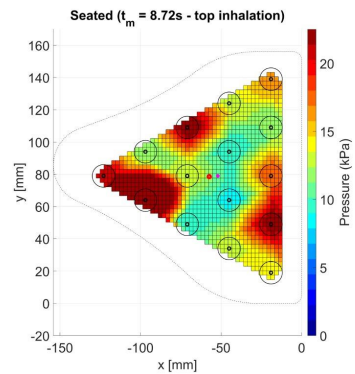
(c)



(d)



(e)



(f)

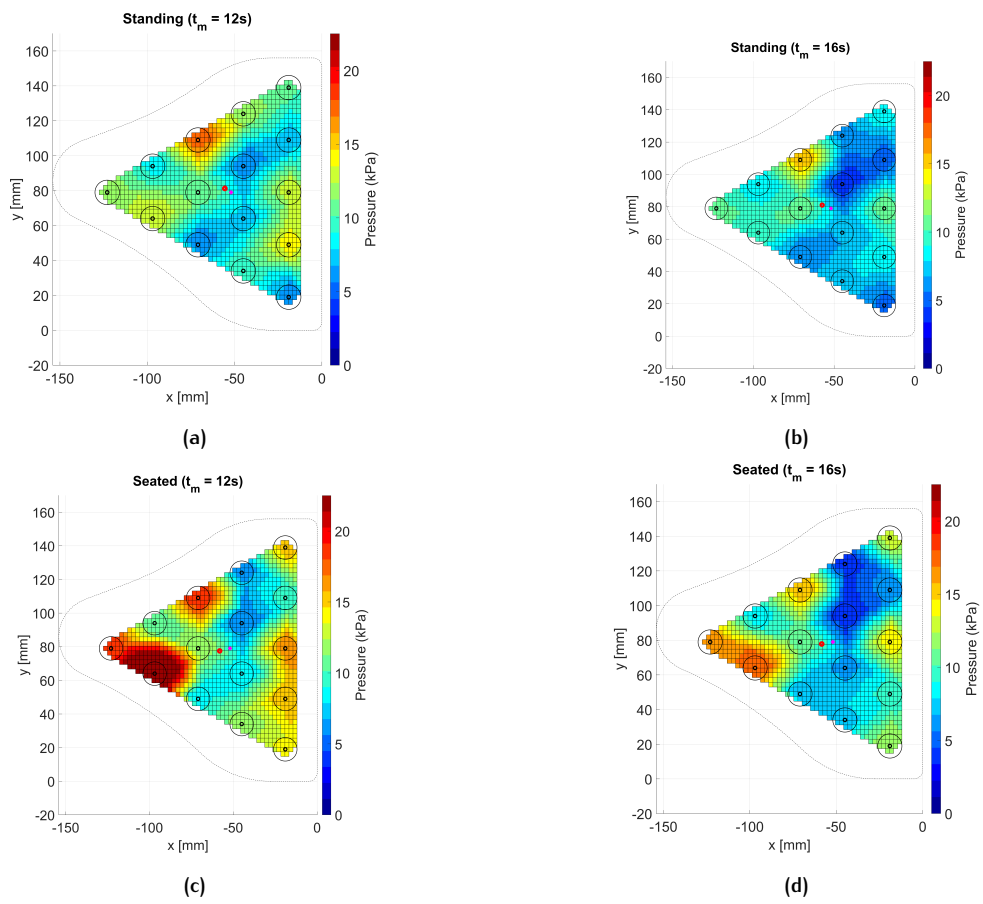


Figure F.2

COLOPHON

This document was typeset using \LaTeX . The document layout was generated using the `arsclassica` package by Lorenzo Pantieri, which is an adaption of the original `classiethesis` package from André Miede.

